

A Quantitative Multiscale Approach to Nanofluidics

Santtu T. T. Ollila

A Quantitative Multiscale Approach to Nanofluidics

Santtu T. T. Ollila

A doctoral dissertation completed for the degree of Doctor of Science in Technology to be defended, with the permission of the Aalto University School of Science, at a public examination held at the lecture hall K of the school on 24 May 2013 at noon.

**Aalto University
School of Science
Department of Applied Physics
Multiscale Statistical Physics Group**

Supervising professors

Tapio Ala-Nissilä

Colin Denniston, University of Western Ontario, Canada

Thesis advisors

Prof. Colin Denniston, University of Western Ontario, Canada

Prof. Tapio Ala-Nissilä

Preliminary examiners

Prof. Enzo Orlandini, University of Padova, Italy

Prof. Ignacio Pagonabarraga Mora, University of Barcelona, Spain

Opponent

Prof. José María Ortiz de Zárate, Universidad Complutense de Madrid, Spain

Aalto University publication series

DOCTORAL DISSERTATIONS 94/2013

© Santtu T. T. Ollila

ISBN 978-952-60-5198-7 (printed)

ISBN 978-952-60-5199-4 (pdf)

ISSN-L 1799-4934

ISSN 1799-4934 (printed)

ISSN 1799-4942 (pdf)

<http://urn.fi/URN:ISBN:978-952-60-5199-4>

Unigrafia Oy

Helsinki 2013

Finland

Publication orders (printed book):

santtu.ollila@aalto.fi



Author

Santtu T. T. Ollila

Name of the doctoral dissertation

A Quantitative Multiscale Approach to Nanofluidics

Publisher School of Science

Unit Department of Applied Physics

Series Aalto University publication series DOCTORAL DISSERTATIONS 94/2013

Field of research Engineering Physics, Theoretical and Computational Physics

Manuscript submitted 16 April 2013

Date of the defence 24 May 2013

Permission to publish granted (date) 7 May 2013

Language English

☐ **Monograph**

☒ **Article dissertation (summary + original articles)**

Abstract

Nanofluidics is a cross-disciplinary field of science that deals with the controlled transport of small amounts of fluid in confined geometries. Due to the confinement, interactions with the channel walls are a dominant factor in the physics of the system and the size of the solute being transported with respect to the channel dimensions is highly relevant for the observed behavior.

Multiscale modeling of soft matter system has become a popular approach of addressing problems that involve disparate time and length scales. However, such models are seldom quantitatively accurate and may contain algorithmic (fitting) parameters whose values are not physically justified. Here, we develop a multiscale model that couples a fluctuating Lattice-Boltzmann solvent and molecular dynamics particles of finite size. We consider in detail how thermal fluctuations should be implemented in the solvent model. Most importantly, we entertain the question of how the coupling should be calibrated in order for the solute particles to have a well-defined hydrodynamic size. We do this by requiring the hybrid model to reproduce both several well-known hydrodynamic steady states, which are sensitive to the particle size but do not depend on fluctuations, and several consistency checks, which do. The dissipation of energy due to the coupling is examined as well.

The model is applied to five different cases. First, porous particles oscillating in a quiescent fluid are examined and new analytical expressions for the hydrodynamic force on porous particles are derived in the case of two different internal mass distributions. We then study colloids bifurcating in a letter T-shaped microfluidic channel. Second, the model is examined in the context of polymers and nanofluidics in the limit where thermal fluctuations are important. We verify the computational model in bulk by reproducing both static and time-dependent results of polymer physics. The necessity of hydrodynamic boundary conditions for agreement with experiments is observed when a lone polymer is confined into a thin film. Last, polymers driven in a corrugated nanochute by a pressure differential are found to exhibit entropic trapping and length and topology-dependent mobilities.

Keywords nanofluidics, microfluidics, Lattice Boltzmann, hydrodynamics, consistency

ISBN (printed) 978-952-60-5198-7

ISBN (pdf) 978-952-60-5199-4

ISSN-L 1799-4934

ISSN (printed) 1799-4934

ISSN (pdf) 1799-4942

Location of publisher Espoo

Location of printing Helsinki

Year 2013

Pages 208

urn <http://urn.fi/URN:ISBN:978-952-60-5199-4>

Tekijä

Santtu T. T. Ollila

Väitöskirjan nimi

Nanofluidistiikan kvantitatiivista moniskaalamallinnusta

Julkaisija Perustieteiden korkeakoulu**Yksikkö** Teknillisen fysiikan laitos**Sarja** Aalto University publication series DOCTORAL DISSERTATIONS 94/2013**Tutkimusala** Teknillinen fysiikka, teoreettinen ja laskennallinen fysiikka**Käsikirjoituksen pvm** 16.04.2013**Väitöspäivä** 24.05.2013**Julkaisuluvan myöntämispäivä** 07.05.2013**Kieli** Englanti☐ **Monografia**☒ **Yhdistelmäväitöskirja (yhteenvedo-osa + erillisartikkelit)****Tiivistelmä**

Nanofluidistiikka on poikkitieteellinen tutkimusala, jossa pyritään pienten nestemäärien hallittuun kuljetukseen kanavissa, joiden halkaisija on tyypillisesti samaa suuruusluokkaa kuin nesteen mukana kulkeutuvien hiukkasten. Kanavien ahtaudesta johtuen neste ja sen kuljettama liue vuorovaikuttaa voimakkaasti kanavan seinien kanssa, millä on suuri vaikutus systeemin fysikaalisiin ominaisuuksiin.

Moniskaalamallinnuksesta on tullut suosittu työkalu pehmeän aineen fysiikan ongelmissa, jotka kattavat useita dekadeja aika- ja pituusasteikolla. Kyseiset mallit eivät tyypillisesti ole kvantitatiivisen tarkkoja ja ne saattavat sisältää malliparametreja, joiden arvot eivät ole fysikaalisin perustein valittuja. Tässä väitöskirjatyössä kehitetään moniskaalamalli, joka kytkee fluktuoivan hila-Boltzmann -nesteen molekyyliidynamiikkamenetelmällä mallinnettavaan hiukkasfaasiin. Työssä kiinnitetään erityishuomiota nestemalliin lisättävän lämpöhuojunnan toteutukseen sekä nesteen ja hiukkasten väliseen kytkentään, mihin mallin kvantitatiivisuus osittain perustuu. Kytkentä kalibroidaan vaatimalla useiden termisistä fluktuatioista riippumattomien, mutta hiukkasen koosta riippuvien jatkuvien olotilojen toteutumista. Kalibroitu systeemi läpäisee lukuisia lämpöhuojunnasta ja hiukkasen koosta riippuvia kokeita, joissa hiukkasen hydrodynaamisen säteen havaitaan olevan sopusoinnussa kalibroidun arvon kanssa. Energian dissipaation ja kytkennän yhteyttä tutkitaan myös.

Mallia sovelletaan viiteen esimerkkitapaukseen. Näistä ensimmäisessä tutkitaan nesteessä värähteleviin huokosiin hiukkasiin kohdistuvia hydrodynaamisia voimia kahden eri massajakauman tapauksessa. Toinen systeemi, jossa termisiä fluktuatioita ei tarvitse ottaa huomioon, liittyy mikrofluidistiikan alaan ja käsittelee kolloidien virtausta T-kirjaimen muotoisessa haarassa. Mallia sovelletaan lisäksi polymeerifysiikkaan ja nanofluidistiikkaan, missä termit fluktuatiot ovat tärkeitä. Mallin toimivuus varmistetaan ensin bulkissa. Hydrodynaamisten reunaehtojen tarpeellisuus huomataan, kun neste ja polymeeri laitetaan kahden samansuuntaisen seinän väliseen rakoon. Viimeinen esimerkkitapaus käsittelee paine-erolla aikaansaattua nestevirtausta kanavassa, jonka poikkileikkaus koostuu vuorottelevista kapeikoista ja leveistä osista. Virtauksen, termisten fluktuatioiden ja kanavan muodon yhteisvaikutuksen huomataan johtavan polymeerin pituudesta ja rakenteesta riippuvaan liikkuvuuteen.

Avainsanat nanofluidistiikka, mikrofluidistiikka, hila-Boltzmann, hydrodynamiikka**ISBN (painettu)** 978-952-60-5198-7**ISBN (pdf)** 978-952-60-5199-4**ISSN-L** 1799-4934**ISSN (painettu)** 1799-4934**ISSN (pdf)** 1799-4942**Julkaisupaikka** Espoo**Painopaikka** Helsinki**Vuosi** 2013**Sivumäärä** 208**urn** <http://urn.fi/URN:ISBN:978-952-60-5199-4>

Preface

The work summarized in this thesis has been carried out in the Multiscale Statistical Physics Group at the Aalto University School of Science and at the Department of Applied Mathematics at the University of Western Ontario under the supervision of professors Tapio Ala-Nissilä and Colin Deniston. The work has been supported by the National Doctoral Program in Nanoscience (NGS-NANO), the Center of Excellence in Computational Nanoscience (COMP), CSC IT Center for Science, Jenny and Antti Wihuri Foundation, Alfred Kordelin Foundation, Magnus Ehrnrooth Foundation and the Finnish Cultural Foundation.

I am grateful to both Tapio and Colin for their encouragement and patience in getting the work accepted. I would like to thank Tapio for his guidance throughout the years to efficient and no-nonsense scientific practice and for introducing me to a number of exemplary scientists each of whom strengthened my inkling of what conducting research in physics entails. I hold Tapio in high regard for his professionalism, commitment to challenging preconceptions in science and willingness to take on ambitious projects whose yields are far from certain.

Colin has infused me with an appreciation for computational science and the inner workings of numerical algorithms. I am impressed by his intuition for physics, his participatory approach to supervising students and his gentlemanly, respectful interaction with other scientists both in the written and spoken word. I am honored to have been his student. I thank him and his family for their kind hospitality.

Professor Mikko Karttunen has been involved in this work from its inception. He has been a central, valuable collaborator and friend. I admire his uncompromising work ethic and dedication to science. I wish to thank him for putting me up at his home many a time and sharing his time on the running trail and an appreciation for good food.

At this stage, I would like to thank professors Enzo Orlandini and Ignacio Pagonabarraga kindly for taking the time to review this manuscript.

I wish to acknowledge Frances MacKay, a fellow graduate student at UWO, for her talent in programming and for wrapping the LB-MD algorithm into a LAMMPS package. I have also had the privilege of looking up to many inspiring colleagues in the MSP group during my years there. I am grateful for your friendship. Much like an adventure, Ph.D. work has unexpected turns. One such turn took place at UWO, where I had the pleasure of meeting Marie and John whose positivity kept my spirits up even at the worst of times. Marie's delectable cooking is only matched by my and John's appreciation for it and by our smiles while opening our lunch boxes.

I am extremely grateful for having dear friends who have kept me occasionally away from work, be it by traveling to France, going rock climbing or golfing. Also, I am fortunate to have such a wonder of a mother and a mother-in-law. Your support in the small and the large has been invaluable.

Contrary to who the author is, I feel that this thesis was brought to completion by the love and compassion of my wife Laura. However articulate I try to be, I fall short in trying to thank you for everything you have done for me. My feelings for you are best embodied in our 9-week-old Sonja sleeping in my lap as I am writing this.

Quand tu veux construire un bateau, ne commence pas par rassembler du bois, couper des planches et distribuer du travail, mais réveille au sein des hommes le désir de la mer grande et large.

-Antoine de Saint-Exupéry

Helsinki, May 7, 2013,

Santtu T. T. Ollila

Contents

Preface	1
Contents	3
List of Publications	5
Author's Contribution	7
1. Introduction	9
2. Brownian Motion and Fluctuating Hydrodynamics	15
2.1 Equations of motion of a viscous fluid	15
2.1.1 Mobility tensors	18
2.2 On Brownian motion	19
2.3 Thermalization of a Brownian particle in the linearized Navier-Stokes theory	23
2.4 Particle-solvent coupling	27
2.4.1 Hydrodynamic shape and size	29
2.4.2 Dissipation and removal of degrees of freedom	30
2.4.3 Implications of the velocity coupling on the diffusion coefficient	31
2.5 Polymer statics and dynamics	32
3. Solvent Model	37
3.1 Overview of solvent models with thermal fluctuations	37
3.2 Lattice Boltzmann–Molecular Dynamics Method	40
3.2.1 From Hamiltonian mechanics to kinetic theory	41
3.2.2 Discretization onto a lattice	45
3.2.3 Thermal fluctuations in the numerical scheme	52
3.2.4 Hydrodynamic radius of a Brownian particle	56

4. Dynamics of Single Particles	63
4.1 Oscillating DBB particles	63
4.2 Colloids in a T-shaped junction	67
5. Transport Properties of Polymers	71
5.1 Polymer dynamics in bulk	71
5.2 Polymer dynamics in slitlike confinement	74
5.3 Polymer transport in nanochannels	78
6. Summary	87
Bibliography	89
Publications	97

List of Publications

This thesis consists of an overview and of the following publications which are referred to in the text by their Roman numerals.

I Santtu T. T. Ollila, Tapio Ala-Nissila and Colin Denniston. Hydrodynamic forces on steady and oscillating porous particles. *Journal of Fluid Mechanics*, **709** pp. 123-148, October 2012.

II Santtu T. T. Ollila, Colin Denniston and Tapio Ala-Nissila. One and two-particle dynamics in microfluidic T-junctions. *Phys. Rev. E(R)*, (5 pages), Submitted 23 April 2013.

III Santtu T. T. Ollila, Colin Denniston, Mikko Karttunen and Tapio Ala-Nissila. Fluctuating lattice-Boltzmann model for complex fluids. *Journal of Chemical Physics*, **134** 064902, February 2011.

IV Santtu T. T. Ollila, Christopher J. Smith, Tapio Ala-Nissila and Colin Denniston. The hydrodynamic radius of particles in the hybrid Lattice Boltzmann – Molecular Dynamics method. *Multiscale Model. Simul.*, **11** pp. 213-243, January 2013.

V Santtu T. T. Ollila, Colin Denniston, Mikko Karttunen and Tapio Ala-Nissila. Hydrodynamic Effects on Confined Polymers. *Soft Matter*, **9** pp. 3478-3487, January 2013.

Author's Contribution

Publication I: “Hydrodynamic forces on steady and oscillating porous particles”

The author contributed significantly to the main ideas of the work, performed all theoretical and numerical calculations, analyzed the results and wrote the first version of the manuscript.

Publication II: “One and two-particle dynamics in microfluidic T-junctions”

The idea to apply the methodology to this work was the author's. The author implemented and performed all the theoretical and numerical calculations, analyzed the results and wrote the first version of the manuscript.

Publication III: “Fluctuating lattice-Boltzmann model for complex fluids”

The author implemented and performed all the numerical work, analyzed the results and wrote the first version of the manuscript.

Publication IV: “The hydrodynamic radius of particles in the hybrid Lattice Boltzmann – Molecular Dynamics method”

The author contributed significantly to the main idea of the manuscript, which was co-written with C. Denniston. The author implemented the numerical model and performed simulations involving thermal fluctuations.

Publication V: “Hydrodynamic Effects on Confined Polymers”

The author contributed significantly to the main ideas of the work. The author implemented and performed all the numerical work, analyzed the results and wrote the first version of the manuscript.

1. Introduction

While they often go unnoticed, various forms of fluid transport are present in the vernacular as references, for instance, to the weather, irrigation in agriculture or to poor peripheral blood circulation in the winter time. Fluid flow is an integral part of life as it perpetually takes place in different forms in the atmosphere (*e.g.*, through advection in the water cycle), the soil (percolation, diffusion), capillaries of plants (capillary action due to surface tension and boundary adhesion) and in the human body (shear-thinning flow in veins, osmosis). The relevant scales over which the flow processes occur in these disparate systems vary from thousands of kilometers and days down to nanometers and nanoseconds. The flows provide transport mechanisms for substances across the wide range of scales that connect the biotic and abiotic parts of an ecosystem.

The movement of fluids has enjoyed continual attention from scientists and engineers since the days of Isaac Newton (1642-1727). His laws of motion and the principle of conservation of energy were applied to continuous matter by Leonhard Euler (1707-1783) and Daniel Bernoulli (1700-1782) who laid a sound theoretical foundation for scientific development of fluid mechanics. Fluid mechanics has been an enormously successful design tool in the aviation [1, 2] and the nautical industries [3]. Drag minimization for fuel efficiency and decreased interior noise [4] and aerodynamic design [5] have become an important part of the automobile industry as well. These breakthroughs in how humans travel and explore the Earth originate in part from the ideas of Claude-Louis Navier (1785-1836) and George Gabriel Stokes (1816-1903) who incorporated the process of dissipation of kinetic energy into heat in the equations of fluid motion. Stokes' contribution to the understanding of viscous resistance of bodies is the basis on which the aforementioned industrial applications are built and his results serve as standard benchmarks even in the present day.

Shortly after Navier in 1823 had defined what viscosity is, Jean-Louis Poiseuille (1799-1869) was already investigating blood flow in narrow capillaries. His pioneering laboratory experiments in the 1830s dealt with finding relationships between volumetric rates of flow driven by a pressure differential in tubes of diameter $15\text{ }\mu\text{m}, \dots, 600\text{ }\mu\text{m}$ and of various lengths. [6] The parabolically shaped steady-state velocity profile that develops in the capillary is known as Poiseuille flow, which was substantiated analytically in the case of a circular pipe by Stokes in 1845. According to Ref. [6], Stokes was uncertain about what the velocity of the fluid should be at the wall and, at first, he refrained from publishing his results.

Similar uncertainties persist over the velocity boundary condition at the solid-liquid interface even today. However, the questions have become more specialized and they typically pertain to the nanometer scale and, *e.g.*, the role of microscopic surface roughness, hydrophobicity vs. hydrophilicity or charge effects. Generally speaking, the material of the wall and its surface properties play an important role in the momentum and energy exchange. Scientists working in the field of nanofluidics deal with small systems in which the validity of the Navier-Stokes (NS) equations is put to question in a setting that is physically complicated in many aspects. First, the fluid motion takes place in confinement, whereby the ratio A/V of the surface area A to the system volume V is large. For this reason, wall-fluid interactions are significant to the physical behavior. The steady-state solutions to the NS equations will eventually fail to describe the velocity field as molecular details become important and the solvent might not be in local equilibrium. The distribution of both solvent and solute particles is affected by the interactions with the walls. Second, the hydrodynamic size of the solute relative to that of the channel becomes relevant as they are of the same order of magnitude. A reduction to a single point in modeling is no longer valid as a point particle can neither rotate nor displace fluid. The equilibrium shape of a more extended solute molecule such as a polymer changes drastically when confined into a narrow channel. Third, thermal fluctuations at the nanoscale are significant. They make the particles undergo spatially constrained Brownian motion, and behavior not seen in bulk is to be expected. Brownian motion next to a charged wall contributes to the formation of an electrical double layer of thickness $\approx 1\text{ nm}$. Fourth, thermal fluctuations and wall-particle interactions compete against external driving forces such as pressure gra-

dients and electromagnetic fields. A change in the relative magnitudes of these factors can be expected to result in new physics provided there are sufficiently accurate experimental and quantitatively predictive computational tools to study them.

Microfluidics is a cross-disciplinary field of science with the purpose of controlled transport and manipulation of volumes of fluid comparable or smaller than a nanoliter. A successfully commercialized microfluidic device is Epson's piezoelectric print head that can express droplets as small as 1.5 picoliters at a rate of 40,000 droplets per second at linear densities up to 360 dots per inch [7]. Microfluidics fuses research efforts made in the fields of microelectronics, molecular biology and molecular analysis. Much of the initial research impetus was provided by the US Department of Defense that funded academic programs in microfluidics in the 1990s in preparation for chemical and biological terrorist threats. [8] The technical prerequisites for micromachining elastomer and glass-based materials into fluid channel circuitry were adapted from microelectronic technologies. The fluid circuitry needing no manual assembly [9] enables precise control over the (biological) sample. Such high-throughput microfluidic devices have been employed in single-molecule genomic analysis [10, 11] and grouping based on gene expression patterns [12] and drug screening [13].

The classification between nano and microfluidics is typically done based on a relevant length scale or a characteristic droplet size. One feature that distinguishes them from one another is the phenomenon of inertial lift acting on solutes discovered by Segré and Silberberg [14, 15, 16]. It stems from nonlinearities in the equations of motion due to non-negligible inertia of the solvent particles [17]. Investigations of inertial microfluidics have experienced a resurgence due to aspirations of employing inertial lift in automated filtration and separation of solvated macromolecules based on their shape [18], hydrodynamic size [19] or porosity [Publication II].

While in many microfluidic systems external forces easily dominate those arising from thermal fluctuations, this is not the case in nanofluidics. As system dimensions are scaled down, thermal fluctuations increase in magnitude and inertial effects grow weak. The regime possesses counterintuitive physics [20], which is partly attributable to the time-reversible equations of motion that can explain how microbes, such as *Escherichia coli* or spermatozoa, swim [21]. Single-molecule studies of DNA in nanoconfinement show promise of applicability to DNA sequencing using solid-state

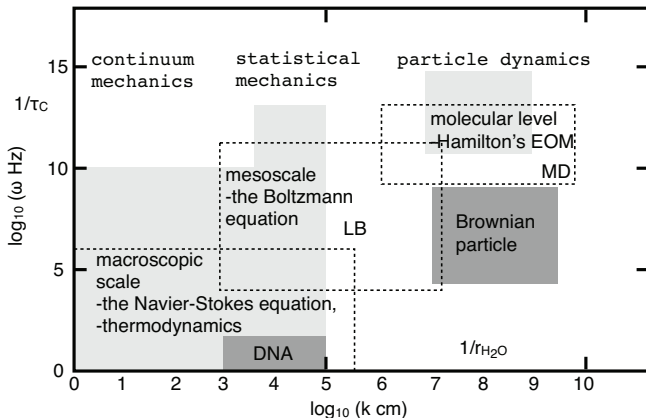


Figure 1.1. An approximate, accessible range of wave vectors and angular frequencies for different computational and experimental approaches. The ranges for the most important experimental methods in hydrodynamics and molecular dynamics are adapted from Ref. [25] and indicated with a light shade of gray. The dark shade of gray corresponds to ranges of measurements in recent experiments of single-particle Brownian motion using an optical trap [26] and DNA dynamics in confinement [23, 24]. The value of the molecular collision time (τ_C) and the mean radius of a water molecule (r_{H_2O}) are indicated as well.

nanopores [22], which are highly parallelizable. Nanoscale confinement in one direction makes DNA stretch in another decreasing the accessible part of the chain configuration space. From a fundamental point of view, the availability of lithography and visualization techniques make for a fascinating opportunity to study entropic trapping of polymers by examining how a single chain moves through nanochannels consisting of segments of different degrees of confinement. The problem is under active experimental study, where polymer separation based on topology and the degree of polymerization have been observed [23, 24].

Computational approaches offer the advantage over experiments that more detailed measurements on a system can be performed without disturbing it. One may isolate the effect of a single quantity by varying its value systematically and performing a series of measurements. The limitations of the approaches are those of the computational model itself and of the computational resources. A typical restriction that researchers have attempted to overcome in the past twenty years or so is the amount of computational time spent simulating the solvent molecules, which serve as the heat bath for the solvent and mediate momentum-conserving hydrodynamic interactions. To illustrate, there is a separation of temporal and spatial scales between the two phases, which refers to

the size of typical colloid or DNA (10^{-4} cm) in contrast to that of a water molecule (10^{-8} cm), and the respective times, ≈ 1 s and 10^{-12} s, they take to diffuse over a distance of their size.

The gap in both the spatial and temporal scales makes the molecular dynamics (MD) method [27] an impractical tool for investigating either Brownian motion or DNA transport as it is limited by a femtosecond (10^{-15} s) time step and roughly atomic resolution [28]. The accessible range of MD is shown as a dashed square in Fig. 1.1 together with the ranges of established spectroscopy techniques (light gray), and recent experiments on the transition to Brownian motion for a single particle and DNA transport in nanochannels (dark gray). In fact, no single methodology can capture the cascade of length and time scales present in a DNA molecule from local, constrained motion of atoms on the chain to the motion of the whole chain in a channel.

To deal with the restriction and to access hydrodynamic time and length scales, the solvent molecules have been grouped into larger, effective solvent particles, whose dynamics is slower and closer to that of the colloids. Alternatively, they have been replaced altogether by a field-theoretic description. These coarse-graining procedures sacrifice atomic detail and temporally fast processes in favor of computational gains such as a large time step and fewer degrees of freedom. However, the coarsening of the description is done such that collective nanoscopic details, *e.g.* thermal fluctuations, are preserved. The overlaps between the macroscopic and the microscopic scales with the mesoscale in Fig. 1.1 for the computational methodologies are important as they allow for validation of well-known limiting behavior such as equipartition and thermal fluctuations in the nanoscale and hydrodynamic forces in the hydrodynamic limit.

Coarse graining is a nontrivial process and its successful application to static quantities, for which the original, more microscopic system and the coarse-grained version yield the same values within a given margin of error, does not translate automatically to dynamic quantities. Therefore, a methodology that would be able to predict both static and dynamic observables quantitatively correctly would be highly desirable. In this thesis, we present a quantitatively predictive multiscale model and validate it against theoretical predictions and experimental observations in bulk [Publications III and IV]. The model is applied to oscillating porous particles [Publication I], colloids in a T-shaped microfluidic junction [Publication II], to a lone polymer in slitlike confinement [Publication V] and

in a nanofluidic channel in Section 5.3.

This overview is structured as follows. Chapter 2 contains a review of the hydrodynamic equations of motion at the Navier-Stokes level of description for an isothermal system, after which we discuss facets of Brownian motion pertinent to this work. Section 2.3 presents the theoretical, Markovian framework of the coupled fluid—Brownian particle system on which the numerical model is based. We discuss the implementation of the coupling in Sec. 2.4, which is a brief review of the material in Publications I, III and IV. In Chapter 3 of this thesis, we present our hybrid computational model of Publications III and IV that combines our fluctuating lattice-Boltzmann (LB) solvent and molecular dynamics particles with a well-defined hydrodynamic radius. Results of Publications I through V are presented in Chapters 4 and 5. Section 5.3 contains unpublished results on polymer mobility in a nanochannel with a varying cross-sectional area. A summary with guidelines for future research in Chapter 6 concludes the overview.

2. Brownian Motion and Fluctuating Hydrodynamics

We begin this chapter by introducing the Navier-Stokes (NS) equations for an isothermal system, which are the macroscopic equations of motion of fluid mechanics. We consider simplifying approximations to the NS equations and their respective restrictions as they will be referred to in later parts of the thesis. Approximative mobility tensors, which model long-range interactions, are summarized and commented on in Section 2.1.1. Next, we discuss the developments in understanding Brownian motion including brief historical remarks. Section 2.3 describes a Markovian theory at the NS level of description of the coupling of a fluctuating solvent and solute particles undergoing Brownian motion. Our considerations of realizing a consistent coupling through the particle velocity and the solvent velocity field are discussed in Section 2.4. The chapter concludes with Section 2.5 that contains an introduction to the properties of the Rouse and the Zimm model of polymer dynamics in the dilute limit.

2.1 Equations of motion of a viscous fluid

In the 1800s, pioneers of fluid mechanics conducted research on the behavior of simple fluids at macroscopic length scales visible to the naked eye. At such scales, *e.g.*, some $1\text{ cm}/0.3\text{ nm} \approx 3.3 \times 10^7$ times the radius of a water molecule [29], it is valid to base the macroscopic theories describing the fluid's behavior on the assumption (the continuum hypothesis) that the structure of the fluid can be considered as continuous. Theoretically, such description is referred to as being “in the continuum limit,” in which the physical system can be assumed to be in local thermodynamic equilibrium, which presumes even a small local volume V_s to contain a large number of solvent particles N_s [30]. What exactly defines the word “local” above is the temporal resolution of the process of interest and the

size of the smallest object whose dynamics one attempts to understand or, alternatively, the size of the probe used to conduct measurements on the system. Provided that the perturbations due to the phenomena under study occur at long wavelengths, $\lambda \gg (V_s/N_s)^{1/3}$, and at low frequencies $\omega \ll 1/\tau_C$, where τ_C is the time scale of molecular collisions, the fluid's response can be described by hydrodynamic equations of motion for conserved quantities. At the Navier-Stokes level for the mass and the momentum, they can be written down in the case of a compressible fluid as [31]

$$\partial_t \rho + \partial_\alpha (\rho u_\alpha) = 0; \quad (2.1a)$$

$$\partial_t (\rho u_\alpha) + \partial_\beta (\rho u_\alpha u_\beta) = -\partial_\beta P_{\alpha\beta} + f_\alpha + \partial_\beta \sigma'_{\alpha\beta}, \quad (2.1b)$$

respectively. The continuity equation (2.1a) depends on the mass density ρ and the components of fluid velocity u_α , $\alpha \in \{x, y, z\}$. The partial derivatives with respect to time and space are abbreviated as $\partial_t \equiv \partial/\partial t$ and $\partial_\alpha \equiv \partial/\partial x_\alpha$. Summation over repeated indices is assumed throughout this thesis. The momentum conservation equation (2.1b) has three terms on the right-hand side. The first of these is due to the pressure tensor $P_{\alpha\beta}$ arising from conservative forces in the fluid and the second is an external force density f_α , which can have contributions from, *e.g.*, gravity or a particle phase. The third term contains the viscous stress tensor $\sigma'_{\alpha\beta}$,

$$\sigma'_{\alpha\beta} = \eta \left(\partial_\alpha u_\beta + \partial_\beta u_\alpha - \frac{2}{3} \partial_\gamma u_\gamma \delta_{\alpha\beta} \right) + \Lambda \partial_\gamma u_\gamma \delta_{\alpha\beta}, \quad (2.2)$$

where η is the shear viscosity related to dissipation due to internal friction and Λ is the bulk viscosity related to compressibility.

The relative magnitudes of the terms in Eq. (2.1) vary significantly depending on the flowing material and boundary conditions [32]. In dealing with liquids, it is often valid to make the assumption of incompressibility, $\rho(\mathbf{r}, t) \equiv \rho_0$, which simplifies Eqs. (2.1) to the incompressible NS equations, which we write here in dimensionless form¹,

$$\frac{\partial \tilde{u}_\alpha}{\partial \tilde{x}_\alpha} = 0; \quad (2.3a)$$

$$\frac{D \tilde{u}_\alpha}{D \tilde{t}} \equiv \left(\frac{\rho_0 L^2}{\eta \tau_0} \frac{\partial}{\partial \tilde{t}} + Re \tilde{u}_\beta \frac{\partial}{\partial \tilde{x}_\beta} \right) \tilde{u}_\alpha = -\frac{\partial \tilde{P}_{\alpha\beta}}{\partial \tilde{x}_\beta} + \frac{\partial^2 \tilde{u}_\alpha}{\partial \tilde{x}_\beta^2} + \tilde{f}_\alpha; \quad (2.3b)$$

$$Re \equiv \frac{LU}{\eta/\rho_0},$$

¹The units of length, velocity and time are scaled using the relations $\tilde{x}_\alpha = x_\alpha/L$, $\tilde{u}_\alpha = u_\alpha/U$ and $\tilde{t} = t/\tau_0$. The time scale τ_0 is defined in Eq. (2.17). The pressure and the force density are scaled as $\tilde{P}_{\alpha\beta} = P_{\alpha\beta}/(\eta U/L)$ and $\tilde{f}_\alpha = f_\alpha/(\eta U/L^2)$.

where the Reynolds number Re , defined in terms of a system-specific, characteristic length scale L and velocity U , is the first dimensionless number used for the dynamical specification of fluid flow in this work. The characteristic time scale τ_0 depends on the particle phase and it is discussed below.

Stokes carried out extensive analytical work using the linear “Stokes approximation” given by the $Re \rightarrow 0$ limit of Eq. (2.3):

$$\frac{\partial u_\alpha}{\partial x_\alpha} = 0; \quad \rho_0 \frac{\partial u_\alpha}{\partial t} = -\frac{\partial p}{\partial x_\alpha} + \eta \frac{\partial^2 u_\alpha}{\partial x_\beta^2} + f_\alpha, \quad (2.4)$$

which neglects the nonlinear term on the left-hand side of Eq. (2.3b) and where we have assumed a diagonal pressure tensor, $P_{\alpha\beta} = p\delta_{\alpha\beta}$, for simplicity. Based on Eq. (2.4), he derived in 1851 the expression

$$\mathbf{F}_d = -6\pi\eta R \mathbf{v}_\infty \quad (2.5)$$

for the *steady-state* drag force \mathbf{F}_d exerted on a *macroscopic* sphere of radius R moving at a small velocity \mathbf{v}_∞ in a *quiescent* fluid assuming a no-slip boundary condition on its surface². [33] The linear Stokes approximation gives an incorrect velocity field far from the particle albeit the same velocity field does lead to Eq. (2.5) [31]. To determine a more accurate far velocity field, Oseen included the asymptotic contribution of the nonlinear term as $\mathbf{v}_\infty \cdot \nabla u_\alpha$ on the left-hand side of the linear momentum equation (2.4). [31] Taking the asymptote into account leads to a first-order correction to \mathbf{F}_d in terms of a length scale $L_O = \eta/(v_\infty \rho_0)$, [34]

$$\mathbf{F}_d = -6\pi\eta R \mathbf{v}_\infty (1 + (3/8)(R/L_O)), \quad (2.6)$$

which tells the nonlinearity affects the interactions at distances greater than L_O , and highlights the first shortcoming of the linear approximation.

The ratio of the inertial terms to the viscous term in Eq. (2.3), $|D\tilde{u}_\alpha/D\tilde{t}|/|\partial^2 \tilde{u}_\alpha/\partial \tilde{x}_\beta^2|$, is customarily used to quantify the relative magnitude of inertial and viscous forces. If the ratio is close to unity, Re determines the ratio of the forces, and for small values of Re , one might be tempted to neglect the nonlinear term or both inertial terms altogether.

Next, we shall introduce solute particles into the solvent in a simplified mobility-tensor description of long-range interactions between them without any account for solvent inertial terms or momentum conservation. The applicability of mobility tensors to nano and microfluidics is commented on in Section 3.1.

²Equation (2.5) is related by Galilean invariance to the case of an immobile particle immersed in a fluid whose far-field velocity is \mathbf{v}_∞ .

2.1.1 Mobility tensors

Most theoretical work on colloidal many-particle systems [36] and some simulation methods of soft matter systems, such as Stokesian dynamics [37], incorporate aspects of hydrodynamic equations of motion in a linearized fashion through approximate mobility tensors, which are, strictly speaking, valid only at intermediate particle separations in the zero-Reynolds-number limit for spherical particles. Here, we introduce two examples of translational mobility tensors that account for the interaction of distant particles due to their relative translational motion in a pairwise fashion. Long-range many-body interactions ensue through a superposition of linearized perturbations in the solvent velocity field in the form of Eq. (2.4):

$$\partial_\alpha u_\alpha = 0; \quad -\partial_\alpha p + \eta \partial_\beta \partial_\beta u_\alpha + f_\alpha^{(n)}(\mathbf{r}) = 0, \quad (2.7)$$

where instantaneous propagation of information is assumed as well as incompressibility and the diagonality of the pressure tensor, $P_{\alpha\beta} = p \delta_{\alpha\beta}$. The notation $f_\alpha^{(n)}(\mathbf{r}) = F_\alpha \delta(\mathbf{r} - \mathbf{r}^{(n)})$ refers to the α component of a force exerted on the fluid by particle No. n at $\mathbf{r}^{(n)}$, which results in a pressure field $p(\mathbf{r})$ and consequently in a velocity field $u_\alpha(\mathbf{r})$. One may determine the effect of $f_\alpha^{(n)}$ in infinite space by Fourier transforming³ Eq. (2.7) and solving for the transformed quantities \hat{p} and \hat{u}_α :

$$\begin{aligned} k_\alpha \hat{u}_\alpha &= 0; \\ i k_\alpha \hat{p} - \eta k^2 \hat{u}_\alpha + \hat{f}_\alpha^{(n)} &= 0 \quad | \cdot k_\alpha; \\ \Rightarrow \hat{p} &= i k_\alpha \hat{f}_\alpha^{(n)} / k^2; \\ \Rightarrow \hat{u}_\alpha &= \hat{H}_{\alpha\beta} \hat{f}_\beta^{(n)} \equiv \frac{1}{\eta k^2} \left(\delta_{\alpha\beta} - \frac{k_\alpha k_\beta}{k^2} \right) \hat{f}_\beta^{(n)}, \end{aligned} \quad (2.8)$$

where $\hat{H}_{\alpha\beta}$ is the Oseen mobility tensor in Fourier space. The inverse Fourier transform of \hat{u}_α reveals the Oseen mobility tensor [38] $H_{\alpha\beta}$ in real space:

$$u_\alpha(\mathbf{r}, t) = \int d\mathbf{r}' (2\pi)^{-d} \int d\mathbf{k} \overbrace{\hat{H}_{\alpha\beta}(\mathbf{k})}^{=H_{\alpha\beta}(\mathbf{r}-\mathbf{r}')} e^{-i\mathbf{k} \cdot (\mathbf{r}-\mathbf{r}')} f_\alpha^{(n)}(\mathbf{r}', t), \quad (2.9)$$

where the time t emphasizes the nonexistent lag of propagation. Performing the integral in three dimensions gives in dyadic notation

$$\mathbf{u}(\mathbf{r}^{(n)}, t) = \mathbf{H}_{mn} \mathbf{f}(\mathbf{r}^{(n)}, t) = \frac{1}{8\pi\eta r_{mn}} \left(\mathbf{I} + \frac{\mathbf{r}_{mn} \mathbf{r}_{mn}}{r_{mn}^2} \right) \mathbf{f}(\mathbf{r}^{(n)}, t), \quad (2.10)$$

³We use the definition $\hat{g} = \mathcal{F}[g] \equiv \int g(\mathbf{x}) \exp(i\mathbf{k} \cdot \mathbf{x}) d\mathbf{x}$ and $g = \mathcal{F}^{-1}[\hat{g}] \equiv (2\pi)^{-d} \int \hat{g} \exp(-i\mathbf{k} \cdot \mathbf{x}) d\mathbf{x}$ for its inverse in d dimensions.

where we denote the vector extending from particle n to particle m as $\mathbf{r}_{mn} = \mathbf{r}^{(m)} - \mathbf{r}^{(n)}$ for brevity. The self-mobility $\mathbf{H}_{mm} = \mathbf{I}/(6\pi\eta R)$ is set by Eq. (2.5).

The Oseen tensor predicts the velocity of particle m to diverge as $r_{mn} \rightarrow 0$, which is unphysical. By minimizing the rate at which the moving fluid dissipates energy, Rotne and Prager were able to derive perturbatively the first-order correction that accounts for the particle size at small separations. [35]. The Rotne-Prager (RP) tensor reads

$$\mathbf{M}_{mn} = \frac{1}{8\pi\eta r_{mn}} \left((\mathbf{I} + \tilde{\mathbf{r}}_{mn}\tilde{\mathbf{r}}_{mn}) + \frac{2R^2}{3r_{mn}^2} (\mathbf{I} - 3\tilde{\mathbf{r}}_{mn}\tilde{\mathbf{r}}_{mn}) \right) \quad (2.11)$$

where $\tilde{\mathbf{r}}_{mn}$ denotes a unit vector parallel to \mathbf{r}_{mn} . More accurate hydrodynamic mobility tensors can be derived systematically from a multipole expansion in which the Oseen tensor is the lowest-order term and the RP tensor is the second [36]. However, their use in stochastic algorithms is nontrivial due to nonzero divergence terms [39].

The mobility tensor used in Stokesian dynamics, which is typically at the Oseen or the RP level, usually incorporates the contribution from the particles' rotational motion as well as the cross-coupling between rotational and translation motion, which is relevant for non-spherical particles. Instead of accounting for close-particle interaction through higher-order terms in the multipole expansion, lubrication forces between the particles have been addressed in a complementary manner [37], which is one facet of accounting for the finite size of the solvated colloidal particles. However, the imposition of boundary conditions causes complications and requires significant modifications to the algorithms [40]. Even in an array of finite cubic boxes of linear size L the expression for \mathbf{H} becomes

$$\mathbf{H}(\mathbf{r} - \mathbf{r}') = \frac{1}{\eta L^3} \sum_{\mathbf{q} \neq 0} \frac{\mathbf{I} - \mathbf{q}\mathbf{q}}{q^2} \exp(i\mathbf{q} \cdot (\mathbf{r} - \mathbf{r}')), \quad (2.12)$$

where $\mathbf{q} = 2\pi\mathbf{n}/L$ and \mathbf{n} is a three-dimensional vector of integers. If the hydrodynamic flow takes place, *e.g.*, in a channel with a varying cross section featuring right angles, the corresponding Stokesian dynamics formulation of the problem becomes impractical. We shall return to the choice of a simulation methodology in greater detail in Chapter 3.

2.2 On Brownian motion

Though Robert Brown in 1827 [41, 42] was not the first to observe the peculiar motion of micrometer-size particles suspended in a fluid, it is

suitable that Brownian motion is named after him as pioneering work on diffusion was established both experimentally and theoretically in his time by his contemporaries Thomas Graham and Adolf Fick. Graham performed experiments on the mixing of gases and liquid diffusion based on which he concluded that diffusion is at least three orders of magnitude slower in liquids than in gases and that diffusive fluxes are proportional to the concentrations of the diffusing species. [43] Adolf Fick formalized Graham's observations in what are now known as Fick's first and second law and recognized that the diffusion coefficient depends on the properties of the substance. [43]

Central to subsequent developments and the reasons why Brownian motion even at the present time remains an active topic of research in both fundamental and applied forms was Albert Einstein, who established the microscopic definition of the diffusion coefficient, D_0 , for a particle as a random walk [44]:

$$D_0 \equiv \lim_{t \rightarrow \infty} \frac{|\mathbf{r}(t) - \mathbf{r}(0)|^2}{2dt}, \quad (2.13)$$

where $\mathbf{r}(t)$ is the position of the particle at time t and d the dimensionality of the system. He proceeded to relate Eq. (2.13) to microscopic fluctuations in the velocity of the particle, $\delta\mathbf{v}(t) = \mathbf{v}(t) - \langle\mathbf{v}\rangle$, through the velocity autocorrelation function (VACF)

$$\phi(t) = \langle\delta\mathbf{v}(t) \cdot \delta\mathbf{v}(0)\rangle \quad (2.14)$$

as

$$D_0 = \frac{1}{d} \int_0^\infty \phi(s) ds, \quad (2.15)$$

where the average $\langle\cdot\rangle$ is taken over different realizations of the random walk. Einstein [44] (1905) and Smoluchowski [45] (1906) derived independently the first successful theory of Brownian motion, which expresses D_0 based on Eq. (2.13) for a spherical particle of radius R , written in modern form as

$$D_0 = \frac{k_B T}{C} = \frac{k_B T}{6\pi\eta R}, \quad (2.16)$$

where k_B is Boltzmann's constant and T is the temperature. The hydrodynamic drag coefficient $C = 6\pi\eta R$ in the denominator of Eq. (2.16) had been derived earlier by Stokes on a hydrodynamic basis [33]. Einstein did state that his stochastic description of the dynamics, Eqs. (2.13)-(2.16), does not hold at short timescales as the particle's motion is dominated by inertia and until it collides with surrounding fluid particles, it moves along a straight trajectory in reaction to an impulse received at $t = 0$. Typically, an order-of-magnitude estimate for the time a solid particle takes

to reach a steady state due to collisions is approximated as

$$\tau_0 = \frac{m}{C} = \frac{(4/3)\pi\rho_p R^3}{6\pi\eta R} = \frac{2}{9} \frac{\rho_p R^2}{\eta}, \quad (2.17)$$

based on the equation of motion $m\ddot{\mathbf{r}} = -C\dot{\mathbf{r}}$ in the case of a spherical particle of mass density ρ_p . However, the actual physics has recently been observed to be more complicated [26].

Einstein's work formed the foundation for relations between microscopic fluctuations and macroscopic transport coefficients such as Eq. (2.16), which are now referred to as Green-Kubo relations [46, 47]. Graham's observation on the different rates of diffusion in liquids and gases is captured by the density dependence embedded in the shear viscosity $\eta = \rho\nu$, where ν is the kinematic viscosity. Einstein's work that initiated the study of random processes was continued in the realm of physics already in 1908 by Langevin who put forth an equation of motion for the Brownian (point) particle [48],

$$m\ddot{\mathbf{r}} = -\xi\dot{\mathbf{r}} + \mathbf{F}, \quad (2.18)$$

where m is the particle's mass and ξ is a friction parameter. The force \mathbf{F} that maintains the thermal agitation of the particle has a vanishing mean, $\langle F_\alpha \rangle = 0$, and a diagonal covariance matrix proportional to temperature $\langle F_\alpha(t)F_\beta(t') \rangle = 2k_B T \xi \delta_{\alpha\beta} \delta(t - t')$, where $\alpha, \beta \in \{x, y, z\}$, that is also the fluctuation-dissipation theorem for the model. The averages $\langle \cdot \rangle$ are taken over different realizations of the noise. Notably, Langevin set the friction parameter to $\xi = C$ in his original paper, which formally leads to Eq. (2.16) in the long-time limit $t \gg m/\xi$. Moreover, the Langevin equation does account for the inertia of the particle, which leads to a ballistic regime, where the mean-squared displacement (MSD) is

$$\text{MSD}(t) \equiv |\mathbf{r}(t) - \mathbf{r}(0)|^2 = d(k_B T/m)t^2 \quad (2.19)$$

for $0 \leq t \ll m/\xi$.

Due to its simplicity and ease of implementation, Eq. (2.18) has been, and is still, used rather freely in many problems to introduce randomness with a white noise spectrum. However, in its original context, the choice of $\xi = 6\pi\eta R$ is inconsistent with the assumptions made by Stokes in deriving Eq. (2.5). The crucial difference is that \mathbf{v}_∞ in Eq. (2.5) denotes a difference between the steady-state velocity of the particle and that of the far-field fluid. According to Ref. [49], Lorentz presented in 1911 an order-of-magnitude estimate for $\xi = 6\pi\eta R$ to be a valid approximation in the unsteady case of Eq. (2.18) only in the limit $\rho_0/\rho_p \ll 1$, *i.e.* when the mass

density of the particle (ρ_p) is much larger than that of the (incompressible) fluid (ρ_0). This limit is, in fact, completely opposite to the one relevant to most biology.

Earlier in 1885, Boussinesq had used the linearized Navier-Stokes equation to derive an analytical expression for the drag force acting on a solid sphere undergoing arbitrary translational motion. Within the linearized framework of Eq. (2.4), the frictional force of Eq. (2.5) should be replaced by the Boussinesq force [50, 31, 51]

$$\mathbf{F}_B(t) = -6\pi\eta R\mathbf{v}(t) - \frac{2}{3}\pi\rho_0 R^3 \dot{\mathbf{v}}(t) - 6\sqrt{\pi\eta\rho_0} R^2 \int_{-\infty}^t \frac{d\mathbf{v}}{ds} \frac{ds}{\sqrt{t-s}}, \quad (2.20)$$

in which the first two terms depend on the instantaneous velocity and acceleration at time t and the last term on the history up to time t . As the Brownian particle moves, it displaces fluid whose resulting motion in turn couples back to the particle's trajectory. Vladimirovsky and Terletzky [52] apparently considered such hydrodynamic memory effects already in 1945, but the paper is in Russian and difficult to access.

Nevertheless, until the mid-1960s microscopic and macroscopic processes in fluid systems were thought to possess clear time scale separation. Quite fittingly to the computational emphasis of the present thesis, persistent long-time tails in the VACF of hard spheres [53, 54] and Lennard-Jones particles [55] were observed in early momentum-conserving molecular dynamics (MD) simulations. Shortly after, the decay of the tails was verified theoretically [56, 57] to be of the form $t^{-d/2}$ in d dimensions. The long-time tail was observed experimentally in 1981 by Paul and Pusey [58]. Such observations are in contradiction with the VACF corresponding to Eq. (2.18), which exhibits no such tail:

$$\phi_L(t) = \frac{d k_B T}{m} \exp(-(\xi/m)t), \quad (2.21)$$

and they indicated the original Langevin treatment to be inadequate as a complete theory of Brownian motion.

With the advantage of hindsight, it is straightforward to see that at least the friction term in Eq. (2.18) must be incorrect. Within the assumptions of the Stokes equation, Boussinesq's expression (2.20) shows, first, that the friction coefficient involves a memory function over the whole trajectory in velocity space and, second, as long as the no-slip sphere is accelerating, its inertia is augmented by a contribution

$$m_a = (2/3)\pi\rho_0 R^3, \quad (2.22)$$

which depends on the mass density of the fluid and the particle's hydrodynamic radius R . The relevant time scale for the particle slowing down is that of the vorticity to diffuse over the size of the particle, $\tau_i = \rho R^2 / \eta$, which is close to τ_0 of Eq. (2.17). In other words, the additional acceleration-dependent inertia must be included in the equation of motion as the particle has not reached a steady state.

Once the Boussinesq force, and thereby the long-time tail, was incorporated in the theoretical description of Brownian motion through linear-response theory [59], a problem with equipartition arose. Equipartition dictates the initial value of the VACF to be equal to $\phi(0) = d k_B T / m$ [30], where d is again the dimensionality. However, the $t \rightarrow 0_+$ limit of the VACF in the linear theory is $\phi(0_+) = d k_B T / (m + m_a)$ [49], which is solely due to the assumption of incompressibility. As soon as a very small compressibility in the theory is accounted for, a rapid decay of the VACF from $d k_B T / m$ to $d k_B T / (m + m_a)$ is found [60].

The mean kinetic energy $k_B T$ per degree of freedom is thus quickly distributed between the particle and the fluid associated with it. This brings up the question of how the fluid and particle degrees of freedom are coupled or removed from the system as they are not independently assigned an energy of $k_B T$. Moreover, the removal of degrees of freedom relates to the coupling of the particle and the fluctuating solvent phase that serves as the only heat bath for the particle. A full specification of the coupling is necessary and highly relevant for computational approaches.

One may therefore question what role the boundary condition on the surface of the particle plays in the assignment of energy as degrees of freedom are removed from the system due to the coupling on the surface of the particle. The topic has been addressed by Hauge and Martin-Löf in great detail in the case of a solid sphere [49], which we shall review next.

2.3 Thermalization of a Brownian particle in the linearized Navier-Stokes theory

Hauge and Martin-Löf have formulated a joint, Gaussian-Markov description for a Brownian particle and the linearized, fluctuating Navier-Stokes equation [49] that builds on the work by Lax [61]. In this section, we present aspects of their work, which are pertinent and applicable to the coupling of composite MD particles to a continuum solvent.

Their formulation is based on Eq. (2.4) for the solvent, where f_α plays

the role of a random force density, and Newton's equations of motion for the translational velocity \mathbf{v} and the angular velocity \mathbf{w} of the particle:

$$m \dot{\mathbf{v}} = \mathbf{F}; \quad (2.23a)$$

$$\mathbf{J} \dot{\mathbf{w}} = \mathbf{M}, \quad (2.23b)$$

where \mathbf{J} is the moment of inertia tensor, and \mathbf{F} and \mathbf{M} are the instantaneous force and torque on the spherical particle. With the origin of the laboratory coordinate system placed at the center of mass of the particle, their components are given by

$$F_\alpha = - \int_{\partial B(t)} \sigma_{\alpha\beta} n_\beta dS; \quad (2.24a)$$

$$M_\alpha = - \int_{\partial B(t)} \epsilon_{\alpha\beta\gamma} r_\beta \sigma_{\beta\gamma} n_\gamma dS; \quad (2.24b)$$

$$\sigma_{\alpha\beta} = -p\delta_{\alpha\beta} + \sigma'_{\alpha\beta} = -p\delta_{\alpha\beta} + \eta(\partial_\alpha u_\beta + \partial_\beta u_\alpha), \quad (2.24c)$$

where $\epsilon_{\alpha\beta\gamma}$ is the Levi-Cevita tensor, the surface normal \mathbf{n} points into the particle and the integration is performed over the surface $\partial B(t)$ of the Brownian particle. The fluid velocity is subject to the no-flow, no-slip constraint,

$$\mathbf{u}(\mathbf{r}, t) = \mathbf{v} + \mathbf{w} \times \mathbf{r}, \quad (2.25)$$

on the surface $\mathbf{r} \in \partial B(t)$. By linearity, Martin-Löf and Hauge proceeded to write the coupled system of Eqs. (2.4), (2.24) and (2.25) as an infinite-dimensional, random Markov vector $\mathbf{a}(t) = \{\mathbf{u}, p, \mathbf{v}, \mathbf{w}\}$ for the average quantities coupled through a matrix \mathbf{G} with a Gaussian noise term \mathbf{g} :

$$\dot{\mathbf{a}} = -\mathbf{G}\mathbf{a} + \mathbf{g}; \quad (2.26a)$$

$$\langle \mathbf{g} \rangle = 0; \quad \langle \mathbf{g}(t) \mathbf{g}^\top(s) \rangle = 2\mathbf{Q}\delta(t-s), \quad (2.26b)$$

where $\langle \mathbf{a} \rangle = 0$ in equilibrium. The stationary states of $\mathbf{a}(t)$ are given by $\mathbf{a}(t) = \int_{-\infty}^t ds \exp(-(t-s)\mathbf{G})\mathbf{g}(s)$, with which one may write the equilibrium correlations as $\mathbf{C} = \langle \mathbf{a}\mathbf{a}^\top \rangle$:

$$\begin{aligned} \mathbf{C} &= \left\langle \int_{-\infty}^t ds \int_{-\infty}^{t'} ds' e^{-(t-s)\mathbf{G}} \mathbf{g}(s) \left(e^{-(t'-s')\mathbf{G}} \mathbf{g}(s') \right)^\top \right\rangle \\ &= 2 \int_0^\infty dt e^{-t\mathbf{G}} \mathbf{Q} e^{-t\mathbf{G}^\top}; \end{aligned} \quad (2.27)$$

using Eq. (2.26b). As $\mathbf{a}(t)$ is Gaussian, its equilibrium distribution is given by

$$P(\mathbf{a}) = \sqrt{\frac{\det |\mathbf{E}|}{(2\pi)^n}} \int_{-\infty}^\infty d\mathbf{a} \exp \left(-\frac{1}{2} \mathbf{a}^\top \mathbf{E} \mathbf{a} \right), \quad (2.28)$$

with $\mathbf{E} = \mathbf{E}^\top$ and correlations between components of \mathbf{a} are expressed as $\langle a_i a_j \rangle = (E^{-1})_{ij}$ [30], which implies $\mathbf{C} = \mathbf{E}^{-1}$ provided that $\det \mathbf{C} \neq 0$.

The dimensionality of \mathbf{a} is n . The mathematics of the Gaussian-Markov process dictates that the noise correlation matrix \mathbf{Q} is constrained by the relation

$$2\mathbf{Q} = \mathbf{G}\mathbf{E}^{-1} + \mathbf{E}^{-1}\mathbf{G}^\top, \quad (2.29)$$

which is obtained by partial integration of Eq. (2.27). We note that \mathbf{Q} is symmetric by construction.

The connection with thermodynamics is established by relating \mathbf{E} to the entropy of the system based on Einstein's fluctuation theory [30], which states that the probability distribution of fluctuations in entropy from the equilibrium, ΔS , is $P_S(\mathbf{a}) \sim \exp(\Delta S(\mathbf{a})/k_B)$, which together with Eq. (2.28) suggests $\Delta S(\mathbf{a})/k_B = -(1/2)\mathbf{a}^\top \mathbf{E} \mathbf{a}$. The rate of entropy production can be related to the correlations in the fluctuations as

$$\dot{\Delta S} = -\frac{k_B}{2} \left(\dot{\mathbf{a}}^\top \mathbf{E} \mathbf{a} + \mathbf{a}^\top \mathbf{E} \dot{\mathbf{a}} \right) = k_B \mathbf{a}^\top \mathbf{E} \mathbf{Q} \mathbf{E} \mathbf{a}, \quad (2.30)$$

where the second equality follows from Eqs. (2.26) and (2.29). Landau and Lifschitz have shown the entropy production in an incompressible fluid to be [31]

$$\dot{\Delta S} = \frac{\eta}{T} \int_V d\mathbf{x} (\partial_\beta u_\alpha \partial_\beta u_\alpha + \partial_\beta u_\alpha \partial_\alpha u_\beta) = \frac{D(\mathbf{u})}{T}, \quad (2.31)$$

where the second equality involves the rate of dissipation of kinetic energy,

$$D(\mathbf{u}) = -\frac{d}{dt} \left(\frac{\rho}{2} \int_V d\mathbf{x} \mathbf{u}^2 + \frac{m}{2} \mathbf{v}^2 + \frac{1}{2} \mathbf{w}^\top \mathbf{J} \mathbf{w} \right), \quad (2.32)$$

which reveals together with the definition of $\mathbf{a}(t)$ that the vector $\mathbf{E} \mathbf{a}$ is equal to

$$\mathbf{E} \mathbf{a} = \frac{1}{k_B T} \{\rho \mathbf{u}, 0, m \mathbf{v}, \mathbf{J} \mathbf{w}\}. \quad (2.33)$$

Multiplying Eqs. (2.30) and (2.31) by $2\delta(t-t')$ and using the Markovian property of Eq. (2.26b) gives

$$\mathbf{a}^\top(t) \mathbf{E} \langle \mathbf{g}(t) \mathbf{g}^\top(t') \rangle \mathbf{E} \mathbf{a}(t') = 2 \frac{D(\mathbf{u})}{k_B T} \delta(t-t'), \quad (2.34)$$

in which $\mathbf{g}(t)$ is the only unknown quantity. The left-hand side of Eq. (2.34) represents the square of the quantity $\mathbf{a}^\top(t) \mathbf{E} \mathbf{g}(t)$. A suitable noise vector corresponding to $\mathbf{a}(t)$ reads

$$\mathbf{g}(t) = \{\mathbf{f}(\mathbf{x}, t)/\rho, 0, \mathbf{K}(t)/m, \mathbf{J}^{-1} \mathbf{L}(t)\} \quad (2.35)$$

which contains the fluctuating force density $\mathbf{f}(\mathbf{x}, t) = (f_x, f_y, f_z)(\mathbf{x}, t)$ that appears on the right-hand side of Eq. (2.4) and the fluctuating force $\mathbf{K}(t)$ and torque $\mathbf{L}(t)$ on the particle. This choice renders $\mathbf{a}^\top \mathbf{E} \mathbf{g}$ as

$$\mathbf{a}^\top \mathbf{E} \mathbf{g} = \frac{1}{k_B T} \left(\int_V \mathbf{u} \cdot \mathbf{f} d\mathbf{x} + \mathbf{v} \cdot \mathbf{K} + \mathbf{w} \cdot \mathbf{L} \right). \quad (2.36)$$

The noise terms in the particle equations of motion can be set identically to zero ($\mathbf{K} = \mathbf{L} = 0$) provided that the random force density \mathbf{f} on the fluid fulfills Eq. (2.34) in the form

$$\left\langle \int_V d\mathbf{x} \mathbf{u}(\mathbf{x}) \cdot \mathbf{f}(\mathbf{x}, t) \int_V d\mathbf{x}' \mathbf{f}(\mathbf{x}', t') \cdot \mathbf{u}(\mathbf{x}') \right\rangle = 2k_B T D(\mathbf{u}) \delta(t - t'), \quad (2.37)$$

which is the fluctuation-dissipation theorem (FDT) for the Markovian framework. Hauge and Martin-Löf's derivation establishes an FDT for the coupled system under the assumptions of the linear Stokes equation and no slip on the particle surface. The imposition of a random force \mathbf{f} on the fluid according to Eq. (2.37) is not a typical way of formulating the FDT. Instead, the fluctuations have been commonly included as components $s_{\alpha\beta}(\mathbf{x}, t)$ in the fluid stress tensor [31]. The connection between the formulations can be made by applying Gauss's theorem to the volume integral in Eq. (2.34):

$$f_\alpha = \frac{\partial s_{\alpha\beta}}{\partial x_\beta}; \quad (2.38)$$

$$\int_V u_\alpha \frac{\partial s_{\alpha\beta}}{\partial x_\beta} d\mathbf{x} = \int_{\partial B \cup \partial V} u_\alpha s_{\alpha\beta} n_\beta dS - \int_V \frac{\partial u_\alpha}{\partial x_\beta} s_{\alpha\beta} d\mathbf{x},$$

where ∂V is the (outer) boundary of the volume V of the system. The equivalent of Eq. (2.37) with $\mathbf{K} = \mathbf{L} = 0$ but in terms of $s_{\alpha\beta}$ reads

$$\langle s_{\alpha\beta}(\mathbf{x}, t) s_{\gamma\lambda}(\mathbf{x}', t') \rangle = 2k_B T \eta_{\alpha\beta\gamma\lambda}^I \delta(t - t') \delta(\mathbf{x} - \mathbf{x}'); \quad (2.39a)$$

$$\eta_{\alpha\beta\gamma\lambda}^I = \eta(\delta_{\alpha\gamma} \delta_{\beta\lambda} + \delta_{\alpha\lambda} \delta_{\beta\gamma}), \quad (2.39b)$$

with $s_{\alpha\beta}(\mathbf{x}, t) \equiv 0$ for $\mathbf{x}, \mathbf{x}' \in \partial B \cup \partial V$. We refer to $\eta_{\alpha\beta\gamma\lambda}^I$ as the incompressible viscosity tensor. This result reaffirms that with no slip on the particle surface, noise need not be added to the particle equations of motion or at the location of the surface of the particle. Moreover, Hauge and Martin-Löf mention an alternative to Eq. (2.39a) in which the contribution on ∂V to the surface integral of the right-hand side of Eq. (2.38) is neglected and it is recast as

$$\int_{\partial B} u_\alpha s_{\alpha\beta} n_\beta dS = v_\alpha \int_{\partial B} s_{\alpha\beta} n_\beta dS + w_\alpha \int_{\partial B} \epsilon_{\alpha\beta\gamma} r_\beta s_{\gamma\lambda} n_\lambda dS \quad (2.40)$$

where u_α is substituted for using Eq. (2.25). The resulting surface integrals can be identified as the random components of force and torque on the particle:

$$K_\alpha = - \int_{\partial B} s_{\alpha\beta} n_\beta dS; \quad (2.41a)$$

$$L_\alpha = - \int_{\partial B} \epsilon_{\alpha\beta\gamma} r_\beta s_{\gamma\lambda} n_\lambda dS, \quad (2.41b)$$

and noise of zero mean and covariance equal to Eq. (2.39a) is applied at $\mathbf{x}, \mathbf{x}' \in V \cup \partial B$. This simply means that if the no-slip condition is realized on the particle surface and fluctuations as per Eq. (2.39) are present everywhere in the solvent, then the fluctuating force and torque contribute to the right-hand side of Eq. (2.23) by the amounts given by Eq. (2.41), which are fully specified by the fluctuating component in the stress and the shape of the particle. Newton's third law is obeyed and present in the form of the difference in signs of the terms in Eqs. (2.40) and (2.41).

In a later note [62], it is shown that Hauge and Martin-Löf's work applies also in the case of full tangential slip on the surface of the Brownian particle. However, the analysis does not apply to partial slip [62].

The two distinct possibilities of meeting the fluctuation-dissipation condition of Eq. (2.34) in terms of $s_{\alpha\beta}(\mathbf{x}, t)$ are similar in the respect that they rely on the no-slip condition on the surface of the particle: both via Eqs. (2.24) and (2.25) and the latter also via Eq. (2.40). A simulation methodology following these guidelines could therefore be realized based on convenience. Next, we shall account for the coupling between the particle and the solvent, and see how it relates to the desired boundary condition on the surface.

2.4 Particle-solvent coupling

In the case of a rigid particle, the fluctuation-dissipation theorem (FDT) of Eq. (2.37) is obeyed if 1) forces and torques according to Eq. (2.41) are exerted on the particle and forces and torques equal to the opposites of the integrands in Eq. (2.41) are exerted on the fluid, and 2) the no-slip condition is met. The first part is a restatement of Newton's third law. As the surface of a rigid, spherical particle is easily tracked and assuming we have access to the random part of the stress tensor, the only missing ingredient in fulfilling the FDT is the realization of no slip.

For practical reasons of solving the complex particle-solvent problem numerically, it can be beneficial to formulate the interfacial forces and torques of Eq. (2.24) in terms of fluid velocity boundary conditions (BCs) on the surface of the particle. The tangential Navier BC [63] reads (the normal vector here points out of the particle)

$$-(v_\alpha - u_\alpha)t_\alpha = \frac{L_s}{\eta}\sigma_{\alpha\beta}n_\beta t_\alpha, \quad (2.42)$$

where \mathbf{t} is a vector normal to \mathbf{n} and L_s is the (microscopic) slip length.

If elastic forces were present, Marengoni-type force densities [63] would have to be included in Eq. (2.42).

While having no slip is nearly always a valid assumption on a macroscopic scale, there can still be microscopic slip. Such situation can therefore involve a relaxation process that results in having no slip at a large scale. The validity of the no-slip BC has been confirmed experimentally at the scale of a few nanometers in many Newtonian liquids [64]. A local frictional force proportional to $-(\mathbf{v} - \mathbf{u})$ on the sharp particle interface corresponds to such a relaxation process for which Eq. (2.42) provides the associated slip length. The direction normal to the particle surface can be characterized on the same basis. A finite slip length in the normal direction would correspond to a porous particle or, at least, to a surface that is permeable to a degree [Publication I].

The first occurrence of such a frictional force between a particle phase and a hydrodynamic theory was in the context of the DBB model by Debye & Bueche [65] and Brinkman [66, 67]. Debye and Bueche attempted to model a polymer coil as a spherical arrangement of point particles whose relative positions were fixed. In the DBB model, the particle phase enters the right-hand side of Eqs. (2.1b), (2.3b) and (2.4) as a linear contribution in the force density as

$$\mathbf{f} = \gamma n(\mathbf{r})(\mathbf{v} - \mathbf{u}); \quad (2.43a)$$

$$n(\mathbf{r}) = \begin{cases} \lambda, & \mathbf{r} \in B(t), \\ 0, & \mathbf{r} \notin B(t), \end{cases} \quad (2.43b)$$

in regions where the constant “node” density $n(\mathbf{r})$ perturbs the fluid flow. The density comprises N nodes that are spread uniformly across the particle volume $B(t)$ and they make up the internal structure of the (permeable) object. In fact, Debye and Bueche viewed a spherically symmetric $n(\mathbf{r})$ and \mathbf{f} as a mean-field model for the interaction between a polymer and solvent [65]. Notably, a comparison of Eq. (2.42) and (2.43a) suggests the relation $\gamma n(\mathbf{r}) = \eta/L_s(\mathbf{r})$, where the slip length should depend on \mathbf{r} unless $n(\mathbf{r})$ is constant. As the particle is present from the perspective of the solvent only via the coupling, its hydrodynamic shape, boundary condition and thermalization are all controlled by Eq. (2.43). From a fundamental point of view, a velocity-dependent force couples the configuration integral to the momentum integral in the partition function of the system. This raises the concern whether equipartition is still obeyed in the system. We address these topics individually in the present work starting from well-established theoretical steady-state considerations.

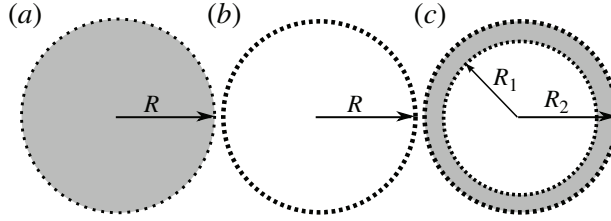


Figure 2.1. Illustration of (a) a uniform-density sphere, (b) a shell and (c) a shell of finite thickness. Figure is from Publication I.

2.4.1 Hydrodynamic shape and size

The linear DBB model (Eqs. (2.4) and (2.43)) can be solved analytically in some steady states for different spherically symmetric distributions $n(\mathbf{r})$. These results are to be viewed as consistency checks for simulation methodologies in the limit of the Stokes approximation. Two experimentally relevant spherical node distributions are a shell, n_{sh} and a uniform-density ball, n_{sp} , which are illustrated in Fig. 2.1(a) and (b) and can be expressed as

$$n_{sp}(\mathbf{r}) = \lambda \Theta(1 - r/R) \equiv N \left(\frac{4}{3} \pi R^3 \right)^{-1} \Theta(1 - r/R); \quad (2.44a)$$

$$n_{sh}(\mathbf{r}) = \lambda_{sh} \delta(r/R - 1) \equiv N (4\pi R^2)^{-1} \delta(r/R - 1), \quad (2.44b)$$

where $\Theta(x)$ is the Heaviside step function. The dimensionless parameter $\beta = R\sqrt{\gamma\lambda/\eta}$ is the ratio of the radius R , where the outermost nodes sit, to the mean pore size $\kappa^{-1} = \sqrt{\eta/(\gamma\lambda)}$. Figure 2.2 displays three typical arrangements that in the laminar flow regime result in a drag force $F(\beta)$ (panels (a) and (b)) and a drag torque $T(\beta)$ (Couette flow, panel (c)) on the particle whose magnitudes are [65, 68, 69]

$$\frac{F(\beta)}{F_d} = \frac{2\beta^2}{2\beta^2 + 9}, \quad \frac{T(\beta)}{T_d} = \frac{\beta^2}{\beta^2 + 9} \text{ for } n_{sh}; \quad (2.45a)$$

$$\frac{F(\beta)}{F_d} = \frac{2\beta^2 G_0(\beta)}{2\beta^2 + 3G_0(\beta)}, \quad \frac{T(\beta)}{T_d} = 1 + \frac{3}{\beta^2} - \frac{3 \coth \beta}{\beta} \text{ for } n_{sp}, \quad (2.45b)$$

where $G_0(\beta) = 1 - (1/\beta) \tanh \beta$, and $F_d = 6\pi\eta Rv$ and $T_d = 4\pi\eta R^3 Q$ are the $\beta \rightarrow \infty$ limits of $F(\beta)$ and $T(\beta)$. The speed of the wall is denoted as v and the constant shear rate of Couette flow as $Q = v/h$. Equation (2.45) informs us that the DBB model corresponds to a combination of the tangential no-slip and the perpendicular no-flow boundary condition through the surface in the $\beta \rightarrow \infty$ limit. Moreover, it tells that, for a given n and a value of β , the effective hydrodynamic radius based on the drag force

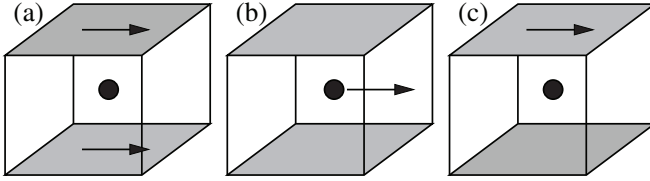


Figure 2.2. Three different ways of measuring the steady-state hydrodynamic radius of a sphere in a parallel-plate arrangement that reduces finite-size effects [70]. (a) Walls move at speed v and particle is kept fixed. (b) Particle is dragged at speed v parallel to and halfway between the walls. (c) Only one wall moves at speed v generating a shear flow, which exerts torque on a particle that is held fixed. Protocols (a) and (b) are related by Galilean invariance. Figure from Publication III.

differs from that based on the drag torque as we have pointed out in Publication I. For example, the effective radii in Eq. (2.45a) are

$$F(\beta)/(6\pi\eta) = 2R\beta^2/(2\beta^2 + 9); \quad (T(\beta)/(4\pi\eta Q))^{1/3} = R\beta^{2/3}/(\beta^2 + 9)^{1/3}, \quad (2.46)$$

which differ significantly from one another unless $\beta \sim \sqrt{\gamma}$ is large. Most importantly, Eqs. (2.45) approach the no-slip limit corresponding to the Stokes drag and torque as $1/\gamma$ as $\beta^2/(2\beta^2 + 9) = 1/2 - 9/(4\beta^2) + \mathcal{O}(\beta^{-4})$ when $\beta \rightarrow \infty$. The consequence of this is that one needs to use a large value of γ in order for Eq. (2.43) to correspond at least approximately to the no-slip limit.

The requirement of large γ in computer simulations seems off-putting at first as it can effectively introduce stiff terms into the equations of motion and lead to numerical instabilities. The use of small γ , on the other hand, leads to inconsistencies of which Eq. (2.46) is the first example. Namely, the idea of being in the no-slip limit, but having an effective hydrodynamic radius, which is determined, *e.g.*, from Eq. (2.5), is a failed concept as the radius is different depending on how it is measured [Publication I and Publication IV].

2.4.2 Dissipation and removal of degrees of freedom

Any slippage in the form of a velocity difference will result in dissipation due the force density of Eq. (2.43). The power output P associated with the dissipation, which we consider in Publication IV, is

$$P \sim \mathbf{f} \cdot \mathbf{v} - \mathbf{f} \cdot \mathbf{u} = \mathbf{f} \cdot (\mathbf{v} - \mathbf{u}) = \gamma(\mathbf{v} - \mathbf{u})^2, \quad (2.47)$$

which is proportional to $1/\gamma$ in the limit of large γ by Eq. (2.45). If the phases are completely decoupled ($\gamma = 0$), there is no associated dissipa-

tion. The $\gamma \rightarrow \infty$ limit has no dissipation associated with it either as $|\mathbf{v} - \mathbf{u}| \sim 1/\gamma$, and \mathbf{v} and \mathbf{u} are the same (fully coupled) and they cannot be considered as statistically independent variables. These arguments carry over to the fluctuating case. With no constraint ($\gamma = 0$) imposed on the velocity space, the variables \mathbf{v} and \mathbf{u} are statistically independent and the latter is Gaussian with $\langle \mathbf{u}^2 \rangle \propto k_B T$. On the other hand, $\gamma \rightarrow \infty$ constrains \mathbf{v} and \mathbf{u} to be identical, which means degrees of freedom are removed from the system. For this reason, \mathbf{v} and \mathbf{u} cannot, and should not, be thermalized independently from one another if one wishes to consider the no-slip limit.

2.4.3 Implications of the velocity coupling on the diffusion coefficient

In Publication IV, we consider a third measure of the hydrodynamic radius of the particle. The velocity coupling will also be responsible for the reproduction of the Stokes-Einstein relation of Eq. (2.16) in the limit where thermal fluctuations are important. The relation depends on the ratio of the temperature T of the heat bath to the hydrodynamic radius $R_H = R$ (via the translational steady-state drag coefficient). The heat bath, which in this case is the fluctuating NS solvent, obeys equipartition far away from particle,

$$\langle u_\alpha u_\beta \rangle = \frac{k_B T}{\rho V_c} \delta_{\alpha\beta}, \quad (2.48)$$

where V_c is the effective volume over which \mathbf{u} is averaged and it is comparable to V_s introduced in Section 2.1. The equation of motion for the CM velocity of the shell-like particle we consider in Publication IV is obtained by summing the contributions of the N nodes and dividing by N :

$$m \dot{\mathbf{v}}_{\text{cm}} = -\gamma(\mathbf{v}_{\text{cm}} - \hat{\mathbf{u}}), \quad (2.49)$$

with $\mathbf{v}_{\text{cm}} = N^{-1} \sum_i \mathbf{v}_i$, $\hat{\mathbf{u}} = N^{-1} \sum_i \mathbf{u}_i$ and m is the combined mass of the nodes of equal mass making up the shell. In its vicinity, the particle will necessarily disturb the fluid velocity field, which can be accounted for in the two-time correlation function as

$$\langle u_\alpha(t_2) u_\beta(t_1) \rangle = \frac{k_B T}{\rho C_v} \delta_{\alpha\beta} \Lambda(t_2 - t_1), \quad (2.50)$$

which contains a fluid response function $\Lambda(t)$ that depends only on the shape of the particle and on fluid properties [49]. We may determine the diffusion coefficient of the particle using the formal solution to Eq. (2.49)

to evaluate the VACF of the particle and Eq. (2.50) as

$$\begin{aligned} D &= \frac{1}{3} \int_0^\infty \langle \mathbf{v}_{\text{cm}}(t) \cdot \mathbf{v}_{\text{cm}}(0) \rangle dt \\ &= \frac{k_B T}{\rho V_c} \frac{\gamma^2}{m^2} \int_0^\infty dt \int_{-\infty}^t dt_1 \int_{-\infty}^0 dt_2 \Lambda(t_2 - t_1) e^{\gamma(t-t_1-t_2)/m}. \end{aligned} \quad (2.51)$$

A closed-form expression for Λ is needed in order to evaluate D explicitly. In any finite system, correlation times are also finite even if hydrodynamic tails are present. For instance, $\Lambda(t) = \exp(-\Gamma|t|)$ leads to

$$D = \frac{k_B T}{\rho V_c \Gamma}, \quad (2.52)$$

which states that D does not explicitly depend on γ of Eq. (2.43) if the correlation time is finite [Publication IV]. Hauge and Martin-Löf [49] have demonstrated that the hydrodynamic tail in the particle's VACF is identical whether a slip or a no-slip BC is imposed on the particle surface. As such, the presence of the hydrodynamic tail does not validate the correctness of the hydrodynamic coupling for a given boundary condition.

2.5 Polymer statics and dynamics

Here we extend the discussion of Brownian motion to polymers. Phenomenological, coarse-grained models of linear polymers are typically constructed by linking N point-like monomers by $N - 1$ (non)linear elastic springs. The time-evolution equation for the monomers in two such models, the Rouse [71] and the Zimm [72] model, can be written formally as the same Langevin equation [73],

$$\frac{\partial \mathbf{r}_m}{\partial t} = \sum_{n=1}^N (-\boldsymbol{\mu}_{mn} \nabla_n U + \nabla_n \mathbf{D}_{mn}) + \mathbf{g}_m, \quad m = 1, \dots, N, \quad (2.53a)$$

$$\langle \mathbf{g}_m \rangle = 0; \quad (2.53b)$$

$$\langle \mathbf{g}_m(t) \mathbf{g}_n(t') \rangle = 2 \mathbf{D}_{mn} \delta(t - t'), \quad (2.53c)$$

where $\boldsymbol{\mu}_{mn}$ is the hydrodynamic mobility tensor (*e.g.*, Eq. (2.11)), $\mathbf{D}_{mn} = k_B T \boldsymbol{\mu}_{mn}$ and $U = U(\mathbf{r}_1, \dots, \mathbf{r}_N)$ is a conservative potential that, depending on the model, accounts for the bonds and excluded-volume interactions between the monomers. We note that Eq. (2.53) neglects the mass of the monomers and inherits all the approximations made in deriving the specific form of $\boldsymbol{\mu}_{mn}$ that is used. Specifically, the Rouse model neglects long-range interactions between the monomers and consecutive beads are connected by a quadratic potential corresponding to Hooke's law,

$$\boldsymbol{\mu}_{mn} = \mathbf{I}_{mn} / \xi; \quad U = \frac{k}{2} \sum_{n=2}^N (\mathbf{r}_n - \mathbf{r}_{n-1})^2, \quad (2.54)$$

where $k = 3k_{\text{B}}T/b^2$ and b is the bond length. The Zimm model, on the other hand, incorporates long-range interactions in the form of the Oseen tensor of Eq. (2.10):

$$\mu_{mn} = \mathbf{H}_{mn}. \quad (2.55)$$

The static and dynamic properties of the Rouse and the Zimm model are well known and they are covered in many textbooks [73, 74]. They serve as important benchmarks for testing computer models of polymers in the appropriate limits where each model applies. In the following, we define static and dynamical quantities central to this thesis.

The size and shape of the polymer can be characterized experimentally and theoretically by measuring the tensor of gyration $Q_{\alpha\beta}$,

$$Q_{\alpha\beta} \equiv \frac{1}{N} \sum_{n=1}^N (r_{n,\alpha} - r_{\text{cm},\alpha})(r_{n,\beta} - r_{\text{cm},\beta}), \quad (2.56)$$

where $\mathbf{r}_{\text{cm}} = N^{-1} \sum \mathbf{r}_n$ is the center-of-mass (CM) coordinate of the polymer. Statistically meaningful quantities are obtained by averaging $Q_{\alpha\beta}$ appropriately for the situation at hand. If no direction takes precedence over any other, the mean size of the polymer can be characterized as (Tr denotes the trace)

$$R_g \equiv \sqrt{\langle \text{Tr} \mathbf{Q} \rangle}, \quad (2.57)$$

which is known as the radius of gyration. The radius of gyration of a solvated polymer in bulk solution depends on many factors. These include, but are not limited to, the dimensionality d of the space in which the polymer is embedded, the excluded-volume effect, solvent conditions and the degree of polymerization N of the chain itself. [73] Asymptotically in good solvent conditions, these effects are included in the scaling relation,

$$R_g \sim N^\nu, \quad (2.58)$$

valid for large N . It contains the exponent ν due to Flory [78] that to good approximation, and agreement with experiments [79], is expressed as $\nu \approx 3/(d+2)$. More involved calculations estimate $\nu = 0.588 \pm 0.001$ for $d = 3$ [80]. Both the Rouse and the Zimm model reproduce Eq. (2.58) in computer simulations with a model-dependent prefactor and ν that involves finite-size corrections to scaling [81].

To determine ν reliably based on Eq. (2.58) for a given polymer model necessitates accurate measurements of R_g for large N . However, scaling theory predicts that the static structure factor of an unconfined lone poly-

mer, defined as

$$S(\mathbf{k}) = \frac{1}{N} \sum_{m,n=1}^N \left\langle \exp[i\mathbf{k} \cdot (\mathbf{r}_m - \mathbf{r}_n)] \right\rangle, \quad (2.59)$$

scales according to $S(k) \sim k^{-1/\nu}$ in the scaling region $kR_g \gg 1$, where $k = |\mathbf{k}|$ is the norm of the wave vector. The asymptotic value of the Flory exponents can therefore be determined by extrapolation of ν versus $1/N$.

Another central quantity is the center-of-mass (CM) diffusion constant of the chain,

$$D_{\text{cm}} \equiv \lim_{t \rightarrow \infty} \frac{\langle |\mathbf{r}_{\text{cm}}(t) - \mathbf{r}_{\text{cm}}(0)|^2 \rangle}{2dt} = \frac{1}{d} \int_0^\infty \langle \delta \mathbf{v}_{\text{cm}}(s) \cdot \delta \mathbf{v}_{\text{cm}}(0) \rangle ds, \quad (2.60)$$

which is distinctly different whether long-range interactions are included or not. The CM diffusion coefficient in the Rouse (R) and the Zimm (Z) model reads [73]

$$D_{\text{cm}}^{(R)} = \frac{k_B T}{N\xi}; \quad D_{\text{cm}}^{(Z)} \propto \frac{k_B T}{\eta R_g} \propto \frac{k_B T}{\eta N^\nu}, \quad (2.61)$$

which show that the drag coefficient of the Rouse chain is simply that of the monomers' added, whereas the Zimm chain experiences a drag proportional to the viscosity of the solvent and the mean size of the chain. The explicit form of the prefactor in $D_{\text{cm}}^{(Z)}$ is model-specific. However, it is addressed in detail in Section 5.1.

Quantities pertaining to decorrelation phenomena in equilibrium are of interest to this work. First of these is the dynamic structure factor, which is related to measurements of Brownian motion of polymers by means of dynamic light scattering experiments. The intensity of the scattered light is related to the dynamic structure factor $S(\mathbf{k}, t)$, which we define it in both the laboratory and the CM coordinate systems,

$$S(\mathbf{k}, t) = \frac{1}{N} \sum_{m,n=1}^N \left\langle \exp[i\mathbf{k} \cdot (\mathbf{r}_m(t+s) - \mathbf{r}_n(s))] \right\rangle_s; \quad (2.62a)$$

$$S_{\text{cm}}(\mathbf{k}, t) = \frac{1}{N} \sum_{m,n=1}^N \left\langle \exp[i\mathbf{k} \cdot (\tilde{\mathbf{r}}_m(t+s) - \tilde{\mathbf{r}}_n(s))] \right\rangle_s, \quad (2.62b)$$

where $\tilde{\mathbf{r}}(t) = \mathbf{r}(t) - \mathbf{r}_{\text{cm}}(t)$. The removal of CM motion makes $S_{\text{cm}}(\mathbf{k}, t)$ more sensitive to intramolecular dynamics. In contrast to this, short-range motion as captured by $S(\mathbf{k}, t)$ for a (rigid) chain will correspond mostly to that along the chain's backbone, which results in scaling corresponding to semi-flexible chains in the laboratory frame of reference. [82, 83] The scaling prediction for Eq. (2.62) quoted in textbooks is [73]

$$S(k, t) = S(k, 0)F(k^z t), \quad (2.63)$$

where $F(k^z t)$ is a scaling function and $z = 2 + \nu_D/\nu$ is the dynamic scaling exponent. Equation (2.63) is expected to hold at infinite dilution in the large- N limit at intermediate lengths [73] $k \in (2\pi/R_g, 2\pi/\sigma)$, where σ is the size of the monomer. The scaling exponent ν_D is associated with how D_{cm} scales as a function of N : $D_{\text{cm}} \sim N^{-\nu_D}$. In 2D, it is known that $\nu_D = 0$ in the presence of hydrodynamic interactions as $D_{\text{cm}} \sim \log N$ for which reason $z = 2$. [75, 76] In 3D, $\nu_D = \nu$ based on Eq. (2.61) in the Zimm model, resulting in $z = 3$. Self-avoiding chains in the absence of hydrodynamic interactions have $\nu_D = 1$ for dilute 3D systems and for all polymer concentrations in 2D leading to $z \approx 3.7$ (3D) and $z = 10/3$ (2D).

A standard way of solving the Rouse model of Eqs. (2.53) and (2.54) is through a coordinate transformation into N equations of motion for N decoupled Rouse modes [77],

$$\mathbf{X}_p = \frac{1}{N} \sum_{n=1}^N \mathbf{r}_n \cos\left(\frac{p\pi}{N} \left(n - \frac{1}{2}\right)\right), \quad (2.64)$$

which decay in time according to

$$\langle \mathbf{X}_p(t+s) \cdot \mathbf{X}_p(s) \rangle_s = \langle \mathbf{X}_p^2 \rangle e^{-t/\tau_p}; \quad (2.65a)$$

$$\tau_p^{-1} \sim \left(\frac{p}{N}\right)^{z\nu}. \quad (2.65b)$$

Albeit it is not exact for an arbitrary potential U , applying the transformation of Eq. (2.64) to more involved models provides valuable information on the deviations from the idealized Rouse and Zimm models. The Rouse modes and the dynamic structure factor present two ways of determining the scaling exponent z .

3. Solvent Model

We begin this chapter by commenting on the available options of modeling transport of solutes in nano and microfluidic channels. The overview is followed by an introduction to the general features of the lattice-Boltzmann (LB) model after which we proceed with the description of the our model that combines our version of the fluctuating LB model with the molecular dynamics (MD) method through a hydrodynamically consistent, velocity-based coupling.

3.1 Overview of solvent models with thermal fluctuations

Modeling of polymer and particle transport in nano and microfluidic channels necessitates that the solvent model is amenable to various types of boundary conditions (BCs), such as periodic ones, solid walls and open boundaries at which thermodynamic boundary conditions (constant pressure, temperature or their gradient) can be fixed. When appropriate, thermal fluctuations should be present and their magnitude should scale according to the smallest length scale in the system. With the solvent playing the role of a momentum-conserving heat bath, the solute, *e.g.* the rigid no-slip test particle, should be at the temperature specified by the heat bath and have correct, macroscopically established transport coefficients such as Eq. (2.16) in the asymptotic limit. To require a model to be quantitatively predictive stipulates that algorithmic parameters should not be explicitly present, but their values should be set based on physical closures or other relations that are functions of physical parameters. The solute-solvent coupling should fulfill the hydrodynamic consistency requirements of Chapter 2 in regard to the size of the solute particle and the boundary condition.

Computational solvent models can be classified into particle-based and

continuum models. Both types of approach have been greatly beneficial to soft matter physics and continue to be due to the still-increasing computational capability of supercomputers. The computational scientist now has a wide selection of tools to choose from, and the choice should be made based on a clear understanding of the intended application and the limitations of each model. Here, we comment on general features of different methods and their applicability to modeling fluid flow in micro and nanoscopic channels.

The molecular dynamics (MD) method [27] is a flexible description in terms of particles that serves as a foundation for more coarse-grained approaches. It offers distinct benefits in that the solvent molecules can possess a complex internal structure and one may vary the degree of quantitative accuracy of the model by choosing phenomenological force fields or *ab initio* force fields based on quantum mechanics. A prime example of the choice is the coarse-grained Mercedes Benz model of water [84, 85], which permits 10^5 molecules to be simulated quite easily and gives qualitatively correct thermodynamics but it does not have the same quantitative accuracy as, *e.g.*, the TIP4P/2005 [28, 86] water model that is, however, limited to $\mathcal{O}(10^3)$ particles. While MD models can be tuned to specialized purposes, the number of required solvent molecules becomes computationally impractical once disparate length scales are introduced in the system. Typically, they appear as large solute particles. For instance, a sphere of radius $R = 10$ nm displaces $\approx 10^4$ water molecules at STP conditions and covering its surface with a single molecular layer of water requires $\sim 10^3$ water molecules. A nanosecond long simulation of a thousand solvated colloids with a femtosecond time step is currently feasible for computing clusters. However, the hydrodynamic phenomena we are often interested in can take place on time scales of the order of milliseconds.

Established coarse-grained, particle-based methods with which longer time scales can be reached are Dissipative particle dynamics (DPD) [27] and Stochastic rotation dynamics/Multiparticle collision dynamics (MPCD) [89]. Both methods have solvent particles that are much larger than individual molecules. Of these two, DPD is computationally more demanding as pairwise forces need to be evaluated at every time step [87]. Solid wall BCs varying from full to no slip have recently been incorporated into DPD [88]. The DPD fluid is gas-like because momentum diffusivity (kinematic viscosity, ν) and mass diffusivity (diffusion coefficient, D) are of the same order as expressed by the Schmidt number $Sc = \nu/D \sim 1$. In con-

trast, higher Sc are attainable in the MPCD method by decreasing the time step of the simulation. The simulation volume in MPCD is divided into collision cells within which a many-particle collision takes place between all particles in the form of a random rotation of the particles' velocities. The collision process is computationally efficient and it establishes a state of local equilibrium defined by the Maxwell-Boltzmann distribution of velocities, which is an aspect of kinetic theory. Implementation of arbitrary boundary conditions is cumbersome in MPCD [89]. A third particle-based method is the Stochastic hard-sphere dynamics (SHSD) algorithm [90], which is similar to DPD but it works in discontinuous time and can incorporate non-ideal equations of state. SHSD is particularly attractive as it parallelizes well and transport coefficients are conveniently adjustable.

Continuum solvents models are implemented on discrete lattices whose resolution Δx determines the smallest volume Δx^3 over which hydrodynamic fields can be defined. It also sets the level of spatial coarse graining: a choice of $\Delta x = 10 \text{ nm}$ corresponds to a volume that contains $\mathcal{O}(10^4)$ water molecules. The moving boundary of an immersed, off-lattice colloid is to be resolved from the perspective of the solvent on the same mesh. The technique of how the boundary is defined and resolved is one of the factors that differentiates continuum methods.

An obvious, but impractical, continuum method that can access long length and time scales is a direct discretization of the fluctuating Navier-Stokes equation with time-dependent boundary conditions for the no-slip colloids of finite radii. The complications of this approach has recently been dealt with by describing a particle with a single spatial coordinate but as a volume source [91]. The scheme captures local flow field effects and, most importantly, the fluid-particle force is based on the no-slip constraint, but does not assume a specific form *a priori*. The incompressible Navier-Stokes equation has also an additional complication due to a non-local pressure field. A recently published finite-volume scheme [92] features a fluctuating continuum far from the solute, but in its vicinity, the solvent is represented with a coarse-grained particle description. However, it is still to be demonstrated how various boundary conditions can be included.

The omission of the inertial terms in the solvent equations of motion *a priori* may lead to unphysical results in microfluidics under certain conditions. This is because the inertia of the fluid is responsible for the mi-

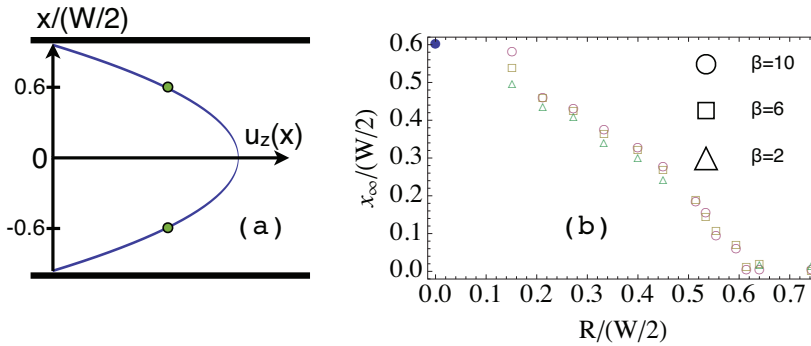


Figure 3.1. (a) Small no-slip particles position themselves at the steady-state coordinate $x_\infty/(W/2) = |\pm 0.6|$ in Poiseuille flow between parallel plates of separation W due to inertial terms in the solvent equations of motion. [17] (b) The position $x_\infty/(W/2)$ changes as a function of the particles radius $R/(W/2)$ and as a function of the DBB permeability parameter β defined in Sec. 2.4.1. The data are acquired using our hybrid LB-MD model in a slit of width $W = 56 \mu\text{m}$ using a mesh constant of $\Delta x = 4.0 \mu\text{m}$ and a time step $\Delta t = 2.13 \mu\text{s}$. The fluid inertia is necessary for these results. The theoretical small-radius limit of a no-slip particle is shown as a solid circle. [17]

gration of rigid spheres to nontrivial steady-state positions in both shear and Poiseuille flows [14, 15, 16, 17]. The phenomenon serves as the basis of modern particle separation and focusing devices [93, 94]. This example speaks in favor of making use of the full nonlinear set of equations (2.1) and letting the NS equations approach the Stokes limit if needed. Figure 3.1 demonstrates how the steady-state position of particles of DBB porosity changes as a function of their radius in our LB-MD method we present next.

3.2 Lattice Boltzmann–Molecular Dynamics Method

The Lattice Boltzmann method (LBM) has become a well-established tool for simulating fluid flow [95, 96]. As it is based on kinetic theory, it can be made to resolve relaxation processes toward local equilibrium and therefore it can account for more microscopic physics than the NS equation and it has been found to reproduce MD results of dense fluid flow quantitatively in nanoscopic systems [97].

One may take a pragmatic point of view and treat the LBM merely as a convenient NS solver provided that one can establish the connection between the LBM and the NS equations. However, such approach provides little understanding of the range of applicability of the method or how to improve it. Instead, we shall proceed with an introduction that relies

on statistical mechanics. Along the way, we comment on the relevance of the description to modeling nano and microfluidics. We also mention which aspects of physics are neglected as the level of description becomes increasingly macroscopic.

3.2.1 From Hamiltonian mechanics to kinetic theory

Molecular level

The system consisting of a single Brownian particle and N solvent particles can be formulated microscopically in terms of classical mechanics by writing down the Hamiltonian for the system in terms of their positions q and momenta p as

$$H(q, p) = H_s(q_s, p_s) + H_p(q_p, p_p) + H_{sp}(q) + H_{\text{ext}}(q), \quad (3.1)$$

where the terms H_s , H_p , H_{sp} and $H_{\text{ext}}(q)$ correspond to the solvent particles (s), The Brownian particle (p), their coupling (sp) interaction and a contribution due to an external field (ext), respectively.

The output of a simple molecular dynamics (MD) model in two dimensions at this level of description with $N = 10^4$ and one Brownian particle has been recently mapped to the generalized Langevin equation by Shin *et al.* [98] While their results provide qualitative insight to the effect of the relative radii and masses of the particles on the non-Markovian nature of the random force, the model is limited to a time scale of some nanoseconds and it cannot match macroscopic transport coefficients quantitatively.

However, more detailed MD models of water, such as TIP4P/2005 [28] in particular, are able to reproduce the shear and bulk viscosities of water and its self-diffusion coefficient within statistical accuracy at atmospheric pressure at temperatures $T = 273 - 373$ K. In isotropic systems, the viscosities are determined from the Green-Kubo relations for the microscopic stress tensor [28]. With great relevance to nanofluidics, Markesteyn *et al.* [86] determined the shear viscosity of TIP4P/2005 water confined between parallel silica walls of separation ≈ 4.3 nm based on the Poiseuille flow profile obtained as a steady-state solution to Eq. (2.1):

$$\partial_z(\eta \partial_z u_x) = -f_x, \quad (3.2)$$

where $u_x = u_x(z)$ is the average velocity of the fluid between the channel walls and f_x is the magnitude of the external body force on the fluid. The viscosity was assumed constant and determined for different water models as $\eta = -f_x / \partial_{zz}^2 u_x$, where $u_x(z)$ was obtained from a fit to the measured

average profile. Regions of thickness $d = 1.2 \text{ nm}$ next to the walls, at which both charge and density variations were seen, were neglected in the fit. The TIP4P/2005 model gave the best agreement with experiments with a maximum relative difference of $\approx 11\%$ in the shear viscosity within the range of temperatures considered [86]. In an earlier work, it was reported that classical Navier-Stokes behavior is approached as the channel width exceeds that of 10 molecular diameters [99].

Quantitatively accurate MD simulations of pure water are limited to time scales of a few nanoseconds, but they do provide insight of solvent-wall interactions and even facilitate engineering of their properties. Nevertheless, an investigation of the collective dynamics *e.g.*, 100 immersed colloidal particles is unfeasible both due to computational demands and practical benefits. For such problems, one would be better off by having the convenience of assigning a desired mass density, shear and bulk viscosities, (open) boundary conditions and a diffusion coefficient of a lone tracer particle without having to employ a time step of one femtosecond.

Kinetic level

Based on the work using TIP4P/2005 water, the average velocity even in 10 nm-wide channels is described by a Poiseuille velocity profile. This suggests that a continuum description of a fluid can be quantitatively accurate even for modeling recent nanofluidic experiments of polymer flow [24]. At this stage, we outline the transition in the description of the system from the molecular to the kinetic level that accounts for the dynamics at longer time scales. The starting point in the coarse-graining process is the Liouville equation. We consider only the Hamiltonian H_s of the N solvent particles. The coupling between the solvent and the particle phase will be reintroduced later through Eq. (2.43).

The state of the solvent with $6N$ degrees of freedom can be characterized by a state vector $\Gamma_N = \{\mathbf{q}_1, \dots, \mathbf{q}_N, \mathbf{p}_1, \dots, \mathbf{p}_N\}$, which is a single point in the $6N$ -dimensional phase space denoted as Ω . A statistical description of the dynamics of the system, which is fully equivalent to the $6N$ coupled Hamiltonian equations of motion for the positions and the momenta, is obtained in terms of the phase-space probability density $\rho_N(\Gamma_N, t)$. The probability for the system to be in the state Γ_N at time t is given by $\rho_N(\Gamma_N, t)d\Gamma_N$, where $d\Gamma_N = d\mathbf{q}_1 \times \dots \times d\mathbf{q}_N \times d\mathbf{p}_1 \times \dots \times d\mathbf{p}_N$. The distribution is normalized as $\int_{\Omega} \rho_N d\Gamma_N = 1$ and the expectation value corresponding to an observable $A(\mathbf{x})$ with $\mathbf{x} \subseteq \Gamma_N$ is given by $\langle A(t) \rangle =$

$\int_{\Omega} \rho_N(\Gamma_N, t) A(\mathbf{x}) d\Gamma_N$. The temporal evolution of ρ_N is determined by the Liouville equation, which reads [30]

$$\frac{\partial \rho_N}{\partial t} = -i\mathcal{L}^N \rho_N \equiv \sum_{j=1}^N \left[\frac{\partial H_s}{\partial \mathbf{q}_j} \cdot \frac{\partial}{\partial \mathbf{p}_j} - \frac{\partial H_s}{\partial \mathbf{p}_j} \cdot \frac{\partial}{\partial \mathbf{q}_j} \right] \rho_N, \quad (3.3)$$

where we have defined the N -particle Liouville operator \mathcal{L}^N . So far, no approximations have been made and Eq. (3.3) remains as difficult to solve as the coupled Hamiltonian equations of motion. However, ρ_N is too detailed a distribution since most experimentally measured quantities can be expressed as one or two-body phase functions. These include the kinetic energy, $\sum_i \mathbf{p}_i^2/(2m)$, and the pair potential energy function, $\sum_{i<j}^{N(N-1)/2} V(|\mathbf{q}_i - \mathbf{q}_j|)$. The reduction in the level of detail of the model is carried out using the BBGKY hierarchy after Bogoliubov, Born, Green, Kirkwood and Yvon. The reduction is presented for many pair potentials in texts [100]. The BBGKY hierarchy is an exact reformulation of the Liouville equation as a recursion of equations of motion for reduced, or coarse-grained, phase-space densities f_n with $n \leq N$ defined as [100, 101]

$$f_n(\Gamma_n, t) \equiv \frac{N!}{(N-n)!} \int \rho_N(\Gamma_N, t) d\mathbf{p}_{n+1} d\mathbf{q}_{n+1} \dots d\mathbf{p}_N d\mathbf{q}_N \quad (3.4)$$

for identical particles, where $\Gamma_n = \{\mathbf{q}_1, \dots, \mathbf{q}_n, \mathbf{p}_1, \dots, \mathbf{p}_n\}$. Last in the hierarchy is the single-particle distribution $f_1(\mathbf{q}_1, \mathbf{p}_1, t)$ with $n = 1$, abbreviated as $f(\mathbf{q}, \mathbf{p}, t)$, whose equation of motion reads [100, 101]

$$\left(\frac{\partial}{\partial t} + \frac{\mathbf{p}}{m} \cdot \frac{\partial}{\partial \mathbf{q}} + \mathbf{F} \cdot \frac{\partial}{\partial \mathbf{p}} \right) f(\mathbf{q}, \mathbf{p}, t) = -C_2[f_2(\Gamma_2, t); \Gamma_2]. \quad (3.5)$$

The quantity $f(\mathbf{q}, \mathbf{p}, t) d\mathbf{q} d\mathbf{p}$ expresses the number of particles at \mathbf{q} with momentum \mathbf{p} at time t within the volume element $d\mathbf{q} d\mathbf{p}$. The right-hand side of Eq. (3.5) contains a collision term C_2 that depends on Γ_2 and the two-particle distribution f_2 that, through its own equation of motion, depends parametrically on Γ_3 and the three-particle distribution f_3 and so on. This is to say that the interaction defined by an N -particle potential in the Hamiltonian is distributed inside the recursion. A truncation of the recursion to Eq. (3.5) means that only binary collisions ($\Gamma_2 = \{\mathbf{q}_1, \mathbf{p}_1, \mathbf{q}_2, \mathbf{p}_2\}$) are included in the description. When C_2 is substituted for by an (approximate) expression in closed form in terms of f , Eq. (3.5) is referred to as a kinetic equation. This means that pair correlations in the model are eliminated by solving for the pair correlation function in terms of f [100]. Approximate Markovian kinetic equations have been derived perturbatively for (dilute) gases, hard-sphere and

other liquids and plasma through an expansion in a suitable, small perturbation parameter [100]. The Markovian evolution of the system, where the kinetic equation involves properties of f only at a single time, is an approximation that relies on the assumption of sufficient time scale separation between the collision time scale τ_C and the time scales of interest $t \gg \tau_C$. The separation in time scales brings about the viewpoint that the collision, where a redistribution of conserved momentum and energy takes place, occurs in a negligible small volume $V_c \leq V_s$ in time τ_C . Hence, the process cannot be described by a Hamiltonian in continuous time, but it must be viewed as a probabilistic transition between an initial and a final state.

Consistency with equilibrium statistical mechanics and the second law of thermodynamics requires that the entropy must increase due to the collision term in Eq. (3.5), which is responsible for driving the system toward a state of local equilibrium. Admissible collision terms are therefore those that fulfill Boltzmann's H theorem. [102]

Continuum level

The connection from Eq. (3.5) to Navier-Stokes equations (2.1) is made by requiring mass and momentum conservation of the collision term. A simple collision term for which the H theorem holds is the BGK approximation,

$$C_2 = -\frac{1}{\tau}(f - f^{\text{eq}}), \quad (3.6)$$

which relaxes $f = f(\mathbf{q}, \mathbf{p}, t)$ toward its local equilibrium value $f^{\text{eq}}(\mathbf{q}, \mathbf{p}, t)$ with a time scale τ . As we consider solvent particles of equal mass, we change the notation from $f(\mathbf{q}, \mathbf{p}, t)$ to $f(\mathbf{r}, \mathbf{v}, t)$. Local mass and momentum densities and the momentum flux tensor are defined as

$$\{\rho(\mathbf{r}, t), \rho(\mathbf{r}, t)u_\alpha(\mathbf{r}, t), \Pi_{\alpha\beta}(\mathbf{r}, t)\} \equiv \int \{1, v_\alpha, v_\alpha v_\beta\} f(\mathbf{r}, t) d\mathbf{v} \quad (3.7)$$

There is some freedom in the choice of the local equilibrium distribution. For a dilute gas, the Maxwell-Boltzmann distribution

$$f_{\text{MB}}^{\text{eq}}(\mathbf{r}, t) = \frac{\rho(\mathbf{r}, t)}{(2\pi k_B T/m)^{3/2}} \exp\left(-\frac{(\mathbf{v} - \mathbf{u})^2}{2k_B T/m}\right), \quad (3.8)$$

is a valid choice, but for a non-ideal barotropic equation of state $P_{\alpha\beta}(\rho)$, which may have non-zero off-diagonal elements, the first three moments of the equilibrium distribution are *constrained* to be

$$\int \{1, v_\alpha, v_\alpha v_\beta\} f^{\text{eq}} d\mathbf{v} = \{\rho, \rho u_\alpha, P_{\alpha\beta} + \rho u_\alpha u_\beta\}. \quad (3.9)$$

The pressure tensor for the Maxwell-Boltzmann distribution *i.e.*, $f^{\text{eq}} = f_{\text{MB}}^{\text{eq}}$, is the equation of state for an ideal gas, $P_{\alpha\beta}^{\text{MB}} = \rho(\mathbf{r}, t)(k_{\text{B}}T/m)\delta_{\alpha\beta}$. However, Eqs. (3.5)-(3.7) and (3.9) are necessary and sufficient conditions for the reproduction of the isothermal Navier-Stokes equations (Eq. (2.1)). [100]

One should recognize that the reduced phase-space density $f(\mathbf{q}, \mathbf{p}, t)$ of Eq. (3.5) has two distinct interpretations. The first of these is that f is a scaled (by a factor N , see Eq. (3.4)) marginal probability distribution of ρ_N of Eq. (3.3). In the second interpretation, f is an ensemble-averaged density,

$$\begin{aligned} f_{\delta}(\mathbf{q}, \mathbf{p}, t) &= \sum_{i=1}^N \delta(\mathbf{r}_i(t) - \mathbf{r})\delta(\mathbf{p}_i(t) - \mathbf{p}) \\ f(\mathbf{q}, \mathbf{p}, t) &= \langle f_{\delta}(\mathbf{q}, \mathbf{p}, t) \rangle, \end{aligned} \quad (3.10)$$

which reveals the stochastic nature of the kinetic description. Namely, for any N -particle initial state $\Gamma_N(0)$, fluctuations,

$$\delta f(\mathbf{q}, \mathbf{p}, t) = f_{\delta}(\mathbf{q}, \mathbf{p}, t|\Gamma_N(0)) - f(\mathbf{q}, \mathbf{p}, t),$$

about f will take place. As the kinetic Boltzmann equation is written in terms of the average f , it does not contain fluctuations. It is possible to formulate an equation of motion for f_{δ} with a noise term, which leads to Eq. (2.39a) in the hydrodynamic limit [103].

3.2.2 Discretization onto a lattice

Solvent

The early developments of the Lattice Boltzmann (LB) method from Lattice Gas Automata [104, 105, 106] to a powerful method for simulating fluid flow are discussed in many reviews [95] and books [96]. The LB fluid based on Eq. (3.5) is typically simulated in three dimensions on a structured lattice with cubic unit cells centered at coordinates $\mathbf{x} = (i, j, k)\Delta x$, where $i = 0, \dots, N_x - 1$ and similarly for j and k . The origin of each cell is connected to those of its neighbors by a discrete set $\mathbb{V} = \{\mathbf{e}_i\}_{i=0}^{n-1}$ of n velocity vectors $\mathbf{e}_i = (e_{ix}, e_{iy}, e_{iz})$, whose magnitude is expressed in units of the lattice speed $v_c = \Delta x/\Delta t$. We denote the discrete time step by Δt . The lattices are distinguished by their dimensionality d and the number of velocity vectors n abbreviated as $DdQn$. The work presented here utilizes the D3Q15 lattice whose unit cell is shown in Fig. 3.2(a). With the division of the velocity space into n lattice directions, the distribution $f(\mathbf{r}, \mathbf{v}, t)$ is

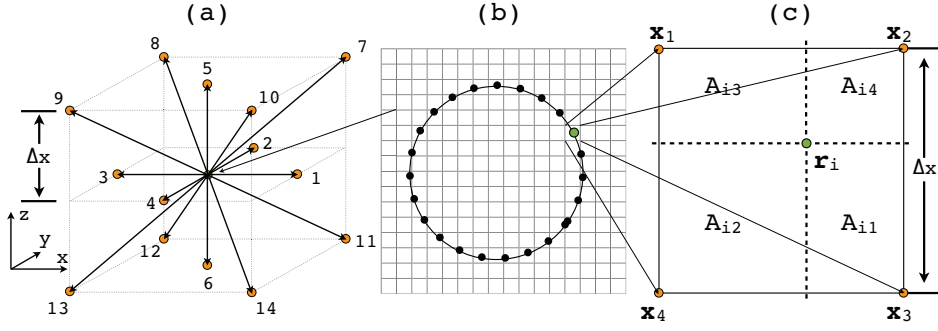


Figure 3.2. (a) The structure of the cubic D3Q15 unit cell with its 15 velocity vectors \mathbf{e}_i with $i = 0, \dots, 14$ of which $\mathbf{e}_0 = \mathbf{0}$ is the null vector. (b) Two-dimensional illustration of a discretized nodal particle that is (c) mapped onto the fluid lattice using the trilinear stencil. The fixed coordinates \mathbf{x}_1 through \mathbf{x}_4 are fluid lattice sites and \mathbf{r}_i is the instantaneous position of the i th node that divides the area Δx^2 into four subareas that form the elements of the trilinear stencil of Eq. (3.24).

split accordingly *e.g.*, $f_i(\mathbf{x}, t) \equiv f(\mathbf{r} = \mathbf{x}, \mathbf{e}_i, t)$, into n components. Analogous to Eqs. (3.7) and (3.9), the definitions of local velocity moments and constraints on their *local* equilibria are

$$\{\rho, \rho u_\alpha, \Pi_{\alpha\beta}\} \equiv \sum_{i=0}^{n-1} \{1, e_{i\alpha}, e_{i\alpha} e_{i\beta}\} f_i(\mathbf{x}, t); \quad (3.11a)$$

$$\sum_{i=0}^{n-1} \{1, e_{i\alpha}, e_{i\alpha} e_{i\beta}\} f_i^{\text{eq}}(\mathbf{x}, t) = \{\rho, \rho u_\alpha, P_{\alpha\beta} + \rho u_\alpha u_\beta\}. \quad (3.11b)$$

The lattice-BGK (LBGK) equations of motion in the n lattice directions are

$$D_i f_i \equiv (\partial_t + e_{i\alpha} \partial_\alpha) f_i = -\frac{1}{\tau} (f_i - f_i^{\text{eq}}) + W_i, \quad (3.12)$$

where we define the material derivatives, D_i , and the forcing terms, W_i , used to implement the external forces \mathbf{F} of Eq. (3.5). The structure of the unit cell determines how many continuum velocity moments are reproduced correctly by their discrete counterparts. For isothermal flows in three dimensions, ten hydrodynamic moments/densities given in Eq. (3.11) are needed: the mass density, the three components of the momentum density and the six independent components of the symmetric momentum flux tensor. The D3Q15 lattice suffices for isothermal flows, but corrections need to be derived to reduce errors in non-Galilean invariant terms [107].

As is made explicit by Eqs. (3.7) and (3.8), the ten listed hydrodynamic fields (in 3D) depend on the distributions f and vice versa. The linear transform between the two can be written as a lattice-dependent matrix \mathbf{m} , ten row vectors of which are already listed on the left-hand side

of Eq. (3.11a). The ordering of the rows is arbitrary. For instance, we could number them as $\mathbf{m}^0 = (1, 1, \dots, 1)$, $\mathbf{m}^1 = (e_{0x}, e_{1x}, e_{2x}, \dots, e_{n-1,x})$, $\mathbf{m}^2 = (e_{0y}, e_{1y}, e_{2y}, \dots, e_{n-1,y})$ and so on. The explicit form of the ten row vectors \mathbf{m}^a corresponding to the moments in Eq. (3.11) for the D3Q15 lattice can be found by substituting the values of $e_{i\alpha}$ based on Fig. 3.2(a). In Publication III, we have appended 5 higher-order velocity moments to the matrix $\mathbf{m} \in \mathbb{Q}^{15 \times 15}$ to make it square and invertible. The procedure is similar for any lattice. Thus, a local mapping from any function $\mathbf{b} \in \mathbb{R}^n$ in the \mathbb{V} basis to the moment basis and its inverse can be written as

$$\mathbf{M} = \mathbf{m} \mathbf{b}; \quad (3.13a)$$

$$\mathbf{b} = (\mathbf{w} \mathbf{m}^\top \mathbf{N}) \mathbf{M}, \quad (3.13b)$$

where \mathbf{w} and \mathbf{N} are lattice-dependent diagonal normalization matrices. To illustrate, we choose $\mathbf{b} = (f_0, f_1, f_2, \dots, f_{14})$ corresponding to the D3Q15 lattice. The mapping yields the vector $\mathbf{M} = (\rho, \rho u_x, \rho u_y, \rho u_z, \Pi_{xx}, \dots)$ by definition. On the other hand, the inverse relation (3.13b) tells that any function in the \mathbb{V} basis (such as f_i or f_i^{eq}) can be expanded in terms of the corresponding moments. An examination of the lattice structure of Fig. 3.2(a) reveals that the 15 vectors \mathbf{e}_i do not constitute an orthonormal basis under the three-dimensional Cartesian dot product. However, a substitution of Eq. (3.13b) in (3.13a) shows that

$$\mathbf{N} \mathbf{m} \mathbf{w} \mathbf{m}^\top = \mathbf{I} \Leftrightarrow N^a \sum_{i=0}^{n-1} w_i m_i^a m_i^b = \delta_{ab}, \quad (3.14)$$

which is to say that the row vectors \mathbf{m}^a of the moment transformation matrix form an orthogonal basis under the w -weighted inner product.

The $n - 10$ nonhydrodynamic lattice-level moments, $M^{10} - M^{n-1}$, appear irrelevant at first glance to isothermal flows, which are hydrodynamically fully specified by $M^0 - M^9$ (i.e., ρ through Π_{zz}) in three dimensions. However, they have turned out to be important for the form of viscous terms in the NS equation (i.e., 3rd and 4th velocity moments of f_i and f_i^{eq}), the stability [108] of isothermal simulations without thermal fluctuations and, as we shall see below, they are crucial for correct thermal fluctuations at the lattice level.

The *local* equations of motion for the moments M^a are obtained by applying the mapping \mathbf{m} to Eq. (3.12):

$$\partial_t M^a + \partial_\alpha \left(\sum_i m_i^a e_{i\alpha} f_i \right) = -\frac{1}{\tau} (M^a - M_{\text{eq}}^a) + \sum_i m_i^a W_i, \quad (3.15)$$

where $M_{\text{eq}}^a = \sum_i m_i^a f_i^{\text{eq}}$. The forcing term has two parts, $W_i = j_i + (1/\tau)\bar{\xi}$, where the j_i account for external forces and $\bar{\xi}$ for thermal fluctuations in the LB fluid. Local mass ($M^0 = \rho$) and momentum conservation ($(M^1, M^2, M^3) = (\rho u_x, \rho u_y, \rho u_z)$) follow directly due to Eq. (3.11b) if $\sum_i m_i^{0,1,2,3} W_i = 0$ holds independently for both the terms included in W_i .

The external force \mathbf{F} in Eq. (3.5) couples to the full distribution f that is unknown in closed form. To implement \mathbf{F} in explicit finite-difference schemes, we approximate the $\mathbf{F} \cdot \partial f / \partial \mathbf{p}$ term of Eq. (3.5) as $F_\gamma \partial_{p_\gamma} f^{\text{eq}}$. Our lattice equilibria are second-order expansions in Hermite polynomials [Publication IV] that fulfill Eq. (3.11b),

$$f_i^{\text{eq}} = w_i \left(\rho + \frac{3}{v_c^2} p_\lambda e_{i\lambda} + \frac{9H_{i\lambda\nu}}{2v_c^4} \left(P_{\lambda\nu} + \frac{p_\lambda p_\nu}{\rho} - \frac{\rho v_c^2}{3} \delta_{\lambda\nu} \right) \right), \quad (3.16)$$

which are easily differentiated with respect to p_γ . The quantity $H_{i\lambda\nu}$ is the tensor $e_{i\lambda} e_{i\nu} - (v_c^2/3) \delta_{\lambda\nu}$. The first four velocity moments of the forcing term evaluated for the D3Q15 lattice are

$$\sum_i F_\gamma \partial_{p_\gamma} f_i^{\text{eq}} = 0; \quad (3.17a)$$

$$\sum_i F_\gamma (\partial_{p_\gamma} f_i^{\text{eq}}) e_{i\alpha} = F_\alpha; \quad (3.17b)$$

$$\sum_i F_\gamma (\partial_{p_\gamma} f_i^{\text{eq}}) e_{i\alpha} e_{i\beta} = u_\alpha F_\beta + F_\alpha u_\beta; \quad (3.17c)$$

$$\sum_i F_\delta (\partial_{p_\delta} f_i^{\text{eq}}) e_{i\alpha} e_{i\beta} e_{i\gamma} = \frac{1}{3} (F_\alpha \delta_{\beta\gamma} + F_\beta \delta_{\alpha\gamma} + F_\gamma \delta_{\alpha\beta}) v_c^2. \quad (3.17d)$$

The third-order velocity moments of Eq. (3.17d) are needed in determining the shear and bulk viscosities for different finite-difference schemes. Finally, the forcing term j_i can be expanded in the moment basis according to Eq. (3.13b):

$$j_i = w_i \sum_{a=0}^{10} m_i^a j^a N^a, \quad (3.18)$$

where $j^0 = 0$ due to Eq. (3.17a), $j^{1,2,3} = F_x, F_y, F_z$ due to Eq. (3.17b) and $j^{4,\dots,9}$ are set by Eq. (3.17c). The nonhydrodynamic moments $j^{10,\dots,n-1}$ are set to zero for which reason they need not be present in the summation.

The local time evolution equations (3.12) need to be expanded in time and space in order to determine the hydrodynamic equations of motion corresponding to the particular choice of the collision term. The Chapman-

Enskog expansion [95] for (3.12) gives

$$\partial_t \rho + \partial_\beta (\rho u_\beta) = 0; \quad (3.19a)$$

$$\begin{aligned} \partial_t (\rho u_\alpha) + \partial_\beta (\rho u_\alpha u_\beta) &= \partial_\beta (-P_{\alpha\beta} + s_{\alpha\beta}) + F_\alpha \\ &\quad + \partial_\beta \left(\eta \left(\partial_\alpha u_\beta + \partial_\beta u_\alpha - \frac{2}{3} \partial_\gamma u_\gamma \delta_{\alpha\beta} \right) \right. \\ &\quad \left. + \Lambda \partial_\gamma u_\gamma \delta_{\alpha\beta} \right) + \mathcal{O}(\partial^3), \end{aligned} \quad (3.19b)$$

where the viscosities depend on the finite-difference scheme. The pressure tensor in this work is diagonal, $P_{\alpha\beta} = P_o \delta_{\alpha\beta} = \rho v_s^2 \delta_{\alpha\beta}$, where v_s is the speed of sound. We have used two finite-difference schemes, the first of which is the standard one [109],

$$f_i(\mathbf{x} + \mathbf{e}_i \Delta t, t + \Delta t) = f_i(\mathbf{x}, t) - \frac{\Delta t}{\tau} (f_i(\mathbf{x}, t) - h_i^{\text{eq}}), \quad (3.20)$$

for which $\eta = (v_c^2/3)\rho(\tau - \Delta t/2)$ and $\Lambda = \eta(5/3 - (3/v_c^2)\partial P_o/\partial \rho)$. The speed of sound v_s is typically chosen to be $v_s = v_c/\sqrt{3}$. The inequality $v_s < v_c$ is a stability requirement in LB algorithms. The generalized equilibrium distribution $h_i^{\text{eq}} = f_i^{\text{eq}} + \tau j_i + \xi_i$ has additional contributions from the external forces, j_i , and thermal fluctuations of the discrete process, ξ_i , which is specified in Section 3.2.3. We have derived an alternative scheme [Publication IV],

$$\begin{aligned} f_i(\mathbf{x} + \mathbf{e}_i \Delta t, t + \Delta t) &= e^{-\Delta t/\tau} f_i(\mathbf{x}, t) + (1 - e^{-\Delta t/\tau}) h_i^{\text{eq}}(\mathbf{x}, t) \\ &\quad + \Delta t \left(1 - \frac{\tau}{\Delta t} (1 - e^{-\Delta t/\tau}) \right) D_t h_i^{\text{eq}}(\mathbf{x}, t) \\ &\quad + \Delta t^2 \left(\frac{\tau^2}{\Delta t^2} (1 - e^{-\Delta t/\tau}) - \frac{\tau}{\Delta t} + \frac{1}{2} \right) D_t^2 h_i^{\text{eq}}(\mathbf{x}, t) + \mathcal{O}(\Delta t^4), \end{aligned} \quad (3.21)$$

which is more accommodating to large values of γ and has $\eta = (v_c^2/3)\rho\tau$ and $\Lambda = \eta(5/3 - (3/v_c^2)\partial P_o/\partial \rho)$. We refer to Eq. (3.21) as the second-order scheme and when only the first two lines are included, we call it the first-order scheme.

Particles

As the fluid velocity \mathbf{u} is only defined on the lattice site located at \mathbf{x} , we must map the surface of our particles, such as those in Fig. 3.3, onto the fluid mesh. Essentially, the mapping boils down to representing the DBB force density of Eq. (2.43a) with $n(\mathbf{r}) = \delta(\mathbf{r} - \mathbf{r}_i)$ as a set of local forces \mathbf{F}_{ij} between the fluid at lattice site \mathbf{x}_j and an individual node i of the particle at \mathbf{r}_i as

$$\mathbf{F}_{ij} = \gamma(\mathbf{v}_i - \hat{\mathbf{u}}_i)\xi_{ij}. \quad (3.22)$$

In Eq. (3.22), $\hat{\mathbf{u}}_i = \mathbf{u}(\mathbf{r}_i)$ is the still undefined fluid velocity at the location of the node and the set of numbers $\{\xi_{ij}\}$ is referred to as a stencil. A

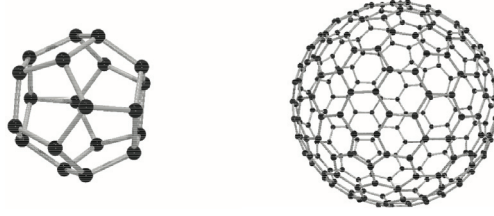


Figure 3.3. Two examples of shell-like particles for which our model provides a hydrodynamically consistent radius. The shell on the left consists of 20 nodes and the one on the right 240. The figure is from Publication IV.

stencil has a compact support on the fluid lattice over which it spreads the effect of a single node such that

$$\sum_{j=1}^{n_s} \xi_{ij} = 1, \quad (3.23)$$

where the sum is taken over the lattice sites within the stencil's compact support. Equation (3.23) guarantees that the surface area of the sphere can be determined exactly independent of the resolution Δx . In this thesis, we have used two different stencils, the first of which is the trilinear stencil $\xi_{ij}^{(T)}$ that is illustrated in Fig. 3.2(c) in two ($d = 2$) dimensions. It couples the node i to the lattice sites \mathbf{x}_j ($j = 1, \dots, n_s$ and $n_s = 2^d$) within the unit cell in which the node resides. Its explicit form for $d = 2$ in the notation of Fig. 3.2(c) is

$$\xi_{ij}^{(T)} = \frac{A_{ij}}{\Delta x^2} = \frac{|x_{ij}| |z_{ij}|}{\Delta x^2}, \quad (3.24)$$

where $x_{ij} = r_{i,x} - x_{j,x}$ and $z_{ij} = r_{i,z} - x_{j,z}$. In three dimensions, the ratios are written in terms of volumes. The Peskin stencil,

$$\xi_{ij}^{(P)} = \psi\left(\frac{x_{ij}}{\Delta x}\right) \psi\left(\frac{y_{ij}}{\Delta x}\right) \psi\left(\frac{z_{ij}}{\Delta x}\right), \quad (3.25)$$

is adapted from the immersed boundary method [110] and it relies on a representation of the Dirac delta function regularized on the grid as

$$\psi(\zeta) = \begin{cases} (3 - 2|\zeta| + \sqrt{1 + 4|\zeta| - 4|\zeta|^2})/8, & |\zeta| \leq 1; \\ (5 - 2|\zeta| + \sqrt{-7 + 12|\zeta| - 4|\zeta|^2})/8, & 1 \leq |\zeta| \leq 2; \\ 0, & |\zeta| > 2. \end{cases} \quad (3.26)$$

The Peskin stencil has a larger support than the trilinear stencil as it extends $2\Delta x$ away from the node thus sampling a total number of $n_s = 4^d$ lattice sites. We use the chosen stencil for the calculation of both \mathbf{F}_{ij} in Eq. (3.22) and the fluid velocity at the node's location through interpolation as

$$\hat{\mathbf{u}}_i = \sum_j^{n_s} \xi_{ij} \mathbf{u}(\mathbf{x}_j). \quad (3.27)$$

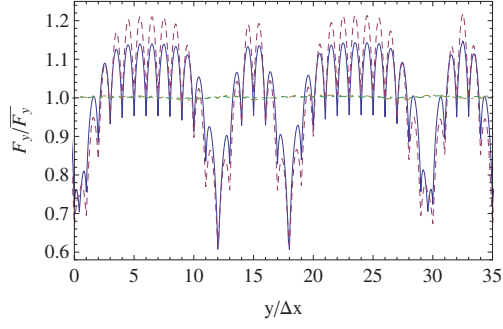


Figure 3.4. Drag force normalized by its mean as a function of particle position. The solid line is the trilinear stencil without interpolation ($\hat{\mathbf{u}}_i = \mathbf{u}(\mathbf{x}_j)$), the dashed line is the trilinear stencil with interpolation, and the dot-dashed line uses the Peskin stencil. The figure is from Publication IV.

The total force \mathbf{F} and torque \mathbf{T} on a composite particle are given by

$$\mathbf{F} = \sum_{i=1}^N \mathbf{F}_i = \sum_{i=1}^N \sum_{j=1}^{n_s} \mathbf{F}_{ij}, \quad \mathbf{T} = \sum_{i=1}^N (\mathbf{r}_i - \mathbf{r}_{\text{cm}}) \times \mathbf{F}_i, \quad (3.28)$$

where N is again the number of nodes on the particle. Newton's third law is fulfilled by applying the d -dimensional mesh of local forces $\mathbf{F}_j = \mathbf{F}(\mathbf{x}_j)$ on the LB fluid,

$$\mathbf{F}_j = \sum_{i=1}^N \mathbf{F}_{ij}, \quad (3.29)$$

which enter Eq. (3.19b) through Eqs. (3.15) and (3.17).

There are cases where these two stencils can be used interchangeably, but the choice warrants a brief discussion. The Peskin stencil can be troublesome close to solid walls (as it may extend inside them) and it requires more computation as each node is spread over 4^d sites as opposed to 2^d in the case of the trilinear stencil. On the other hand, the Peskin stencil is numerically stable for large values of γ in cases in which the trilinear stencil is unstable even for values short of the no-slip limit. The Peskin stencil is much better at eliminating lattice corrugation effects which is desirable as any evidence of the structure of the lattice is not physical. We have quantified this in Fig. 3.4 by measuring the magnitude $F_y = |\sum_j^{n_s} \mathbf{F}_{ij}|$ of the drag force on a point particle (a lone node) using both stencils as it moves over the lattice. The trilinear stencil exhibits 30% deviations from the mean whereas they are negligible for the Peskin stencil. For this reason, using the trilinear stencil for point particles is suspect. However, using it for composite particles like those in Fig. 3.3 poses few problems as the corrugation is averaged out by the nodes that are in different relative positions with respect to the unit cell. [Publication IV]

3.2.3 Thermal fluctuations in the numerical scheme

Before we go into some detail of how thermal fluctuations are implemented in our LB fluid, we must describe how the temperature of the fluid is measured. We assess the temperature reproduction of our method in two ways in a system of size L^3 with periodic boundary conditions (PBCs) in all directions. The first is a measurement of equipartition in k -space through a discrete Fourier transform of local momentum density. We will find equipartition to be obeyed at the target temperature of $T = 300$ K for all $k > 0$ tested. The exception is $T(k = 0) = 0$ due to the global conservation law of total momentum and the fact that the system as a whole is stationary. The second assessment is based on a block-averaged velocity. The total mass of the system is $M_T = \rho L^3$ and the components of the CM velocity of the system are $V_\alpha = M_T^{-1} \sum_{\mathbf{x}} \rho(\mathbf{x}) \Delta x^3 u_\alpha(\mathbf{x})$. We define the subsystem temperature $T(L_s)$ through

$$\frac{1}{2} \sum_{\alpha} \left\langle \frac{[\sum_{\mathbf{x} \in L_s^3} \rho(\mathbf{x}) \Delta x^3 u_\alpha(\mathbf{x})]^2}{\sum_{\mathbf{x} \in L_s^3} \rho(\mathbf{x}) \Delta x^3} \right\rangle = \frac{3}{2} k_B T(L_s). \quad (3.30)$$

After we have discussed the theory of the fluctuating LBE, we return to the issue of the temperature in subsystems of linear size $\Delta x \leq L_s \leq L$.

In its standard formulation, the LB fluid is compressible. This results in the following form of the viscosity tensor in the dissipative stress

$$\eta_{\alpha\beta\gamma\lambda} = \eta \left[\delta_{\alpha\gamma} \delta_{\beta\lambda} + \delta_{\alpha\lambda} \delta_{\beta\gamma} - \frac{2}{3} \delta_{\alpha\beta} \delta_{\gamma\lambda} \right] + \Lambda \delta_{\alpha\beta} \delta_{\gamma\lambda}. \quad (3.31)$$

In the hydrodynamic limit, the implementation of thermal fluctuations amounts to adding Gaussian noise with amplitudes and correlations specified by Eq. (2.39a) with Eq. (3.31) substituted for $\eta_{\alpha\beta\gamma\lambda}^I$. However, the lattice-level fluctuations in the LB fluid are not in the hydrodynamic limit, which must be taken into consideration together with the specific structure of the lattice model. To describe what proper thermalization at the mesh scale Δx entails, we begin by expanding the noise terms $\bar{\xi}_i$ of the continuous-time Eq. (3.15) in terms of continuous-time fluctuations $\bar{\zeta}^a$ in the moments M^a using Eq. (3.13b)

$$\bar{\xi}_i(\mathbf{x}, t) = w_i \sum_a m_i^a \bar{\zeta}^a(\mathbf{x}, t) N^a. \quad (3.32)$$

In Publication IV, we have identified three aspects of correct reproduction of Eq. (2.39a) in LB simulations. They are 1) a proper thermalization of nonhydrodynamic modes, 2) a correction of the variance of the discrete stochastic process ξ_i to match with that of the continuum process $\bar{\xi}_i$, and

3) a cancellation of a scaling factor of the noise variance due to the finite-difference scheme. We address them here one by one.

All modes M^a exist on an even footing at the lattice level, where they are decoupled from one another in terms of the inner product of Eq. (3.14). This means the nonhydrodynamic modes, $M^a, a > 9$, should obey equipartition just as the hydrodynamic modes, $a \leq 9$, do. The lattice-level noise amplitudes must reflect this fact [111].

We have identified Eq. (3.12) as an Ornstein-Uhlenbeck process and found the variance of the discrete processes ξ_i , Eqs. (3.20) and (3.21), after a time step Δt to be

$$\langle \xi_i^2 \rangle = \langle \bar{\xi}_i^2 \rangle q_{\text{OU}}^2 \equiv \langle \bar{\xi}_i^2 \rangle \frac{1 - \exp(-2\Delta t/\tau)}{2\tau}, \quad (3.33)$$

assuming the continuum process $\bar{\xi}_i$ to have zero mean and its standard deviation to remain constant over the duration of Δt . By linearity, the correction affects each of the noise terms of the discrete process in Eq. (3.32): $\langle (\zeta^a)^2 \rangle = \langle (\bar{\zeta}^a)^2 \rangle q_{\text{OU}}^2$. The correction factor q_{OU} depends on the collision term in Eq. (3.5) and it can be derived for collision matrices C_{ij} that decompose in a convenient way.

The last correction is found through perusal of the finite-difference schemes of Eqs. (3.20) and (3.21). Let us assume the generalized equilibria $h_i^{\text{eq}} \propto \xi_i$ contain fluctuations of the desired amplitude. The obvious factor q_{FD} multiplying ξ_i that must be divided out is

$$q_{\text{FD}} = \begin{cases} \Delta t/\tau, & \text{for Eq. (3.20);} \\ 1 - \exp(-\Delta t/\tau), & \text{for Eq. (3.21),} \end{cases} \quad (3.34)$$

which is exact for the standard scheme, Eq. (3.20) and approximate for Eq. (3.21) as it only cancels the local term without derivatives. At this stage, the necessary corrections relating the continuous and the discrete processes are known and we may expand the discrete processes using Eq. (3.13b) as

$$\xi_i(\mathbf{x}, t) = w_i \sum_a m_i^a \zeta^a(\mathbf{x}, t) N^a. \quad (3.35)$$

The indices $a = 4, \dots, 9$ correspond to fluctuations added to the stresses. Their explicit expressions are

$$\begin{aligned} \langle (\zeta^a)^2 \rangle &= \langle (\bar{\zeta}^a)^2 \rangle \frac{q_{\text{OU}}^2}{q_{\text{FD}}^2} = \langle s_{\alpha\beta}^2 \rangle \frac{q_{\text{OU}}^2}{q_{\text{FD}}^2} = 2\eta k_B T \frac{1}{\Delta x^3 \Delta t} \frac{q_{\text{OU}}^2}{q_{\text{FD}}^2}, \quad a = 7, 8, 9; \\ \langle (\zeta^a)^2 \rangle &= \langle s_{\alpha\alpha}^2 \rangle \frac{q_{\text{OU}}^2}{q_{\text{FD}}^2} = 4\eta k_B T \frac{1}{\Delta x^3 \Delta t} \frac{q_{\text{OU}}^2}{q_{\text{FD}}^2}, \quad a = 4, 5, 6, \end{aligned} \quad (3.36)$$

where the $1/(\Delta x^3 \Delta t)$ terms are the discrete spatial and temporal delta functions from Eq. (2.39a). The second moment of both hydrodynamic and

nonhydrodynamic fluctuations ($a = 10, \dots, 14$) can be written as a single relation

$$\langle (\zeta^a)^2 \rangle = \frac{18}{N^a} A_\eta \equiv \frac{18}{N^a} \eta k_B T \frac{1}{\Delta x^3} \frac{1}{\Delta t} \frac{q_{\text{OU}}^2}{q_{\text{FD}}^2}, \quad (3.37)$$

where the insertion of the corresponding normalization factor N^a reduces Eq. (3.37) to Eq. (3.36).

At the beginning of this Section, we stated that the dissipative stresses are correlated according to Eq. (3.31). The diagonal and off-diagonal terms of the compressible viscosity tensor are

$$\begin{aligned} \eta_{\alpha\alpha\beta\beta} &= (1 - 3 v_s^2) \eta \equiv Y \eta; \\ \eta_{\alpha\alpha\alpha\alpha} &= 2 \eta + (1 - 3 v_s^2) \eta = (2 + Y) \eta, \end{aligned} \quad (3.38)$$

which are evaluated using the definition of the bulk viscosity found below Eq. (3.20). The form of the correlation matrix $C^{ab} = \langle \zeta^a(\mathbf{x}, t) \zeta^b(\mathbf{x}', t') \rangle$ with $a, b \in \{4, 5, 6\}$ for the discrete processes in our simple fluid follows directly as

$$C = \frac{q_{\text{OU}}^2}{q_{\text{FD}}^2} \begin{bmatrix} \langle s_{xx}^2 \rangle & \langle s_{xx} s_{yy} \rangle & \langle s_{xx} s_{zz} \rangle \\ \langle s_{xx} s_{yy} \rangle & \langle s_{yy}^2 \rangle & \langle s_{yy} s_{zz} \rangle \\ \langle s_{xx} s_{zz} \rangle & \langle s_{yy} s_{zz} \rangle & \langle s_{zz}^2 \rangle \end{bmatrix} = 2 A_\eta \begin{bmatrix} 2 + Y & Y & Y \\ Y & 2 + Y & Y \\ Y & Y & 2 + Y \end{bmatrix}. \quad (3.39)$$

The matrix C is then Cholesky-decomposed in order to generate three C -correlated random stresses from three independent Gaussian random number with a mean of zero and unit variance [Publication IV].

We are now in a position to comment on the block-averaged temperature in the system. The idea behind Eq. (3.30) is that the velocity coupling of Eq. (2.43) constrains a block of fluid of the linear size of the particle to move collectively. The momentum conservation law would affect the temperature of the particle in the extreme particle size limit $\sim L$. As we shall see, the local fluctuations in the stress tensor are responsible for generating $T(\Delta x)$ equal to the target temperature of 300 K. On the other hand, if the total momentum of the system is initialized to zero, the momentum conservation equation will keep it zero and $T(L) = 0$. First, we assume there to be no local fluctuations in the stress, but the CM velocity V_α to fluctuate such that $(1/2) M_T \langle V_\alpha^2 \rangle = (1/2) k_B T$. A cubic subsystem of mass $M_s = \sum_{\mathbf{x} \in L_s^3} \Delta x^3 \rho(\mathbf{x})$, whose average is $\langle M_s \rangle = \rho L_s^3$, will be at a temperature $T(L_s)$ given by

$$\frac{1}{2} k_B T(L_s) = \frac{1}{2} \langle M_s \rangle \langle V_\alpha^2 \rangle = \frac{1}{2} k_B T \left(\frac{L_s}{L} \right)^3 \quad (3.40)$$

assuming the subvolume undergoes the same Brownian walk in velocity space as the CM velocity. We have found the prediction of Eq. (3.40) to be

correct by measuring it in volumes up to $L = 50$ nm. The results are shown in Fig. 3.5(a). Now, we thermalize the system to $T(\Delta x) = 300$ K such that $(1/2)(\rho_0 \Delta x^3) \langle u_\alpha^2 \rangle = (1/2)k_B T(\Delta x)$ holds at the single-site level and set the global momentum constraint to $M_T V_\alpha = 0 \forall \alpha$. The second moment of the block-averaged velocity difference $V_\alpha^s - V_\alpha$,

$$V_\alpha^s - V_\alpha = \frac{\sum_{\mathbf{x} \in L_s^3} \rho(\mathbf{x}) \Delta x^3 u_\alpha(\mathbf{x})}{M_s} - \frac{\sum_{\mathbf{x} \in L^3} \rho(\mathbf{x}) \Delta x^3 u_\alpha(\mathbf{x})}{M_T}, \quad (3.41)$$

evaluates to

$$\langle (V_\alpha^s - V_\alpha)^2 \rangle = \left(\frac{\Delta x}{L} \right)^3 \left[\left(\frac{L}{L_s} \right)^3 - 1 \right] \langle u_\alpha^2 \rangle \quad (3.42)$$

assuming incompressibility and delta-correlated velocities $\langle u_\alpha(\mathbf{x}) u_\beta(\mathbf{x}') \rangle = \langle u_\alpha^2 \rangle \delta_{\alpha\beta} \delta(\mathbf{x} - \mathbf{x}')$. The subsystem temperature in this case is given by

$$\frac{1}{2} k_B T(L_s) = \frac{1}{2} \langle M_s \rangle \langle (V_\alpha^s - V_\alpha)^2 \rangle = \frac{1}{2} k_B T \left(1 - \left(\frac{L_s}{L} \right)^3 \right). \quad (3.43)$$

A measurement of the block-averaged temperature due to local stress fluctuations shown in Fig. 3.5(a) agrees with Eq. (3.43). By having both local, Eq. (3.43), and global, Eq. (3.40), fluctuations, the temperature profile flattens at the target temperature.

The last adjustment that can be made is the optimization of the non-hydrodynamic modes with respect to temperature reproduction at the single-site level. We report here our findings pertaining to the D3Q15 lattice from Publication IV. While they are decoupled in terms of Eq. (3.14), the *local* stress modes $\Pi_{\alpha\beta}$ and the nonhydrodynamic modes $M^{10,11,12}$ get coupled through the local evolution equations (3.15). The coupling can be written explicitly to lowest order in the case of the D3Q15 lattice as

$$\begin{aligned} \frac{2}{3} \nabla \cdot & \begin{bmatrix} \rho(u_y^2 + u_z^2)/2 & P_{xy} + \rho u_x u_y & P_{xz} + \rho u_x u_z \\ P_{xy} + \rho u_x u_y & \rho(u_x^2 + u_z^2)/2 & P_{xy} + \rho u_y u_z \\ P_{xz} + \rho u_x u_z & P_{yz} + \rho u_y u_z & \rho(u_x^2 + u_y^2)/2 \end{bmatrix} \\ & + \frac{2}{9} \nabla \left(\text{Tr } P - \rho + \frac{K^{\text{eq}}}{\sqrt{2}} \right) = -\frac{1}{\tau} \mathbf{J}^{(1)}, \end{aligned} \quad (3.44)$$

which is written in lattice units ($v_c = 1$). The vector $\mathbf{J}^{(1)} = (M^{12}, M^{10}, M^{11}) - (M_{\text{eq}}^{12}, M_{\text{eq}}^{10}, M_{\text{eq}}^{11})$ is zero in equilibrium. This relation demonstrates that the fluctuating stresses $s_{\alpha\beta}$ accompanying the corresponding $P_{\alpha\beta}$ in Eq. (3.19b) couple to $M_{\text{eq}}^{14} = K^{\text{eq}}$. We have optimized the amplitude K_0 of the 14th moment $K^{\text{eq}} = K_0(\rho - \text{Tr}(P - s))$. The optimization leads to a clear improvement in the single-site temperature as demonstrated by Fig. 3.5(b).

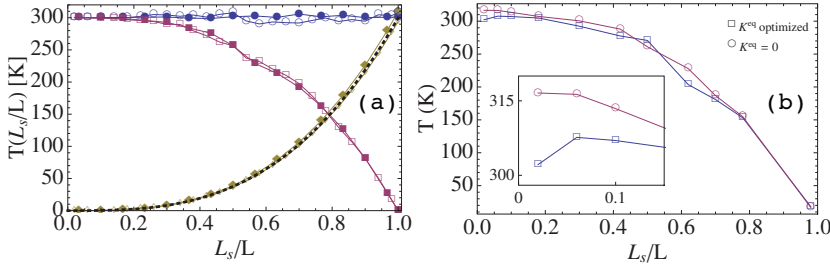


Figure 3.5. (a) Temperature measured from block-averaged momentum fluctuations using Eq. (3.30) as a function of the ratio of subsystem size L_s to the linear size L of the system (solid symbols: $L = 30$ nm, hollow symbols: $L = 50$ nm) with only local noise present in the stress tensor (squares), with noise only in the CM coordinate of the total system (diamonds), and with both local noise in the stress and Langevin thermostat on the CM coordinate present (circles). The dashed line is the function $300 \text{ K}(L_s/L)^3$. (b) Optimization of the $M_{eq}^{14} = K^{eq}$ mode gets the local temperature closer to the target of 300 K. The target temperature was 300 K and the speed of sound is $v_s = (1/\sqrt{3})(\Delta x/\Delta t)$ in both (a) and (b). The figures are from Publication III.

3.2.4 Hydrodynamic radius of a Brownian particle

The physical consistency and accuracy of a method for simulating impermeable solute particles requires one to consider the fundamental concept of a hydrodynamic radius R_H . It can be determined from any measurement that is sensitive to the size of the particle. The requirement of consistency means that all such measurements should provide results that differ from one another by no more than the lattice discretization, *i.e.*, $|R_{H,1} - R_{H,2}| < \Delta x$, where $R_{H,1}$ and $R_{H,2}$ are measured values using different protocols. A sufficient degree of consistency is a prerequisite for the method to be quantitatively predictive.

Here, we review our work in Publication I and Publication IV on the hydrodynamic radius of spherical shells such as those in Fig. 3.3 and point particles. Both the trilinear of Eq. (3.24) and the Peskin stencil of Eq. (3.25) were used, but here we concentrate on the physics and refer to the stencils only when they are relevant. We determined the hydrodynamic radius in different steady states at small Re shown in Fig. 2.2 for which there are analytical, well-established results. Panel (a) and (b) are related by Galilean invariance and the radius is determined from Eq. (2.5) as

$$R_{H,1} = F/(6\pi\eta v) \quad (3.45)$$

by measuring the force F on the particle through Eq. (3.28). In panel (c), the fluid exerts a drag torque of magnitude $T = 4\pi\eta R^2 Q$ on an imperme-

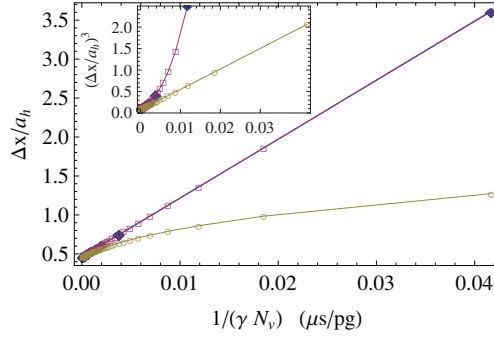


Figure 3.6. The inverse of the hydrodynamic radius (denoted here by a_h) as given by Eqs. (3.45) and (3.46) for a composite sphere of radius $R = 2.0 \Delta x$ as a function of the inverse of the product γN_v , where N_v is the node count. Solid diamonds correspond to a measurement of the drag force on a moving sphere (Fig. 2.2(b)), open squares to the drag force on a fixed particle in a shear flow (Fig. 2.2(c)), and open circles are hydrodynamic radius as computed by drag torque on a fixed particle in a shear flow (Fig. 2.2(c)). All results use the trilinear stencil and interpolated velocities at the nodes. This demonstrates that $1/R_H$ measured from drag forces is a linear function of $1/\gamma$, whereas the same quantity from drag torque is not. Inset: Inverse of hydrodynamic radius cubed versus $1/(\gamma N)$ showing that $1/R_H^3$ from the torque shows a linear relationship.

able, no-slip particle giving another definition for R_H :

$$R_{H,2} = (T/(4\pi\eta Q))^{1/3}. \quad (3.46)$$

The magnitude T of the torque is given by Eq. (3.28). Figure 3.6 shows $\Delta x/R_H$ based on Eqs. (3.45) and (3.46) as a function of $1/(\gamma N)$, *i.e.*, the inverse of the product of the coupling constant of Eq. (2.43a) and the number of nodes making up the sphere. We found that once γ is increased until $R_{H,1}$ is within 1% of R (the radius where the particles sit in Fig. 3.3), then $R_{H,2}$ is also within 1% from R such that $R_{H,2}/R_{H,1} \approx 1.02$. We also observed that the approach to $\Delta x/R$ depends on the functional form of $R_{H,1}$ and $R_{H,2}$ on γ through Eq. (2.45).

We have also studied extensively the effect of the stencil on the hydrodynamic radius of both point and composite particles. The larger support of the Peskin stencil as compared to the trilinear stencil results in larger measured values of R_H , but otherwise the results are similar as long as the interpolated velocity is used in Eq. (3.22). Using it is necessary as the noninterpolated velocity adds to the torque by distributing the force farther from the particle, which is why an inequality $R_{H,2} > R_{H,1}$ will persist. We also found that the finite-difference scheme of Eq. (3.21) provided increased stability over Eq. (3.20) at large values of γ if the trilinear stencil was used [Publication IV].

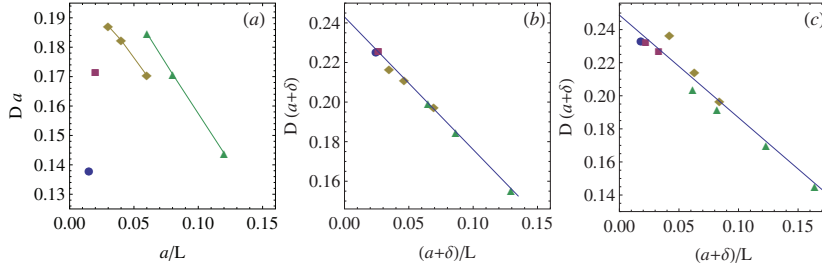


Figure 3.7. Diffusion coefficient $D(L)$ as a function of the ratio of the hydrodynamic radius $R_{H,3} = R + \delta$ to the linear system size L with the notation $a = R$. A change from (a) $\delta = 0$ to (b) $\delta = 0.38 \Delta x$ in the case of the Peskin stencil produces a good collapse with $B \approx 3.04$. (c) The corresponding values for the trilinear stencil are $\delta = 0.12 \Delta x$ and $B \approx 2.82$. [Publication IV]

Having fixed the only free parameter in the model, γ , based on the observed agreement between steady-state definitions of R_H that are not dependent on temperature, we proceeded to measure R_H based on the diffusion coefficient D_0 and the added mass m_a . Thermal fluctuations were present as detailed in Publication III. There are significant finite-size effects in the measurement of the diffusion coefficient, which is why one expects it to have the value

$$D(L) = D_0 - \frac{k_B T}{6\pi\eta} \frac{B}{L} = \frac{k_B T}{6\pi\eta} \left(\frac{1}{R_{H,3}} - \frac{B}{L} \right), \quad (3.47)$$

where the value of the constant $B = 2.837$ is due to finite-size effects [112]. The temperature of the bath at the scale of the particle is found from a figure similar to Fig. 3.5(b). Our results for $D(L)$ are plotted in Fig. 3.7 both for the Peskin (panels (a) and (b)) and the trilinear stencil (panel (c)). We find that the hydrodynamic radius $R_{H,3}$ based on diffusion has a form $R_{H,3} = R + \delta$, where R is the distance where the nodes sit (Fig. 3.3) and δ is a stencil-dependent constant whose value is found by fitting. Assuming $\delta = 0$ for the Peskin stencil gives clear disagreement with Eq. (3.47) as evidenced by Fig. 3.7(a), which simply means that $R_{H,3}$ and R differ. However, a good collapse results for $\delta = 0.38 \Delta x$ and we measure $B \approx 3.04$ (Peskin, panel (b)). The data points corresponding to the trilinear stencil collapse best for $\delta = 0.12 \Delta x$ and we find $B \approx 2.82$. The radius $R_{H,3}$ is within 1% of the steady-state values of $R_{H,1}$ and $R_{H,2}$. Again, the larger spread of the Peskin stencil produces a larger hydrodynamic radius as we have learned to expect.

Another nontrivial measure of the hydrodynamic radius for a no-slip particle is the added-mass term m_a of Eq. (2.22) that is present in the Boussinesq equation. We can determine the value of m_a for our nodal par-

ticle by measuring its velocity autocorrelation function (VACF, Eq. (2.14)) in two cases within the linear response regime. First, we measure the VACF of a particle diffusing in equilibrium in a periodic box for which $\phi(0)/d = k_B T/M$ where M is the combined mass of the nodes used to construct the particle and of the fluid within its hydrodynamic radius R_H that always tracks it. At short times, M will be augmented by m_a and the VACF decays to $\phi(t_s)/d = k_B T/(M + m_a)$ as sound waves transport momentum from the particle at times $t < t_s \equiv R_H/v_s$. In the second case, we turn off thermal fluctuations by setting $T = 0$ in Eq. (3.37) and work in the geometry of Fig. 2.2 in a large box where the walls impose a zero far-field velocity. We drag the particle halfway between and parallel to the walls with a constant force F_0 at times $t < 0$ until we let it go by setting $F_0 = 0$ for $t \geq 0$. The normalized deceleration $(-1/F_0)dv/dt$ should overlap with $\phi(t)/(dk_B T)$ for $t > t_s$ in the linear response regime. This deterministically moving particle has $(-1/F_0)dv(0)/dt = 1/(M + m_a)$ as there are no sound waves in the steady state. We examine a particle whose hydrodynamic radius is $R_H = 2.7 \Delta x$ and the corresponding sound time is $t_s = 2.7 \Delta x/(\Delta x/\sqrt{3}\Delta t) \approx 4.7 \Delta t$. Figure 3.8(a) from Publication IV displays the data for the deterministic and stochastic VACF response functions from the intercepts of which with the y axis we determined $m_a \approx 40$ ag, which yields $R_H \approx 2.7 \Delta x$. The value matched with the deterministically measured radius. The combined mass of the nodes (66.9 ag) and the fluid within the shell $((4/3)\pi\rho R_H^3 = 82.3$ ag) predict $M = 149$ ag, which is very close to the measured 150 ag based on the intercept $1/M$. Moreover, the response functions overlap for $t > t_s$ and for $t/\Delta t > 40$ they merge and match the hydrodynamic long-time tail. We emphasize that agreement with the asymptotic tail only does not tell about the correctness of the coupling or the boundary condition as the tail is identical for a full-slip particle [49].

As a rule of thumb for attaining the no-slip limit in simulations, the value of γ needs to be increased until it forces a mass of $\rho\Delta x^3/N$ to relax in a time scale close to a single time step Δt , where N is again the number of nodes. One may still question whether that is large enough a value to eliminate possible dissipation of kinetic energy in the numerical solvent due to the presence of the particle. We entertain the issue in Publication IV by considering the average aggregate rate of change of kinetic energy

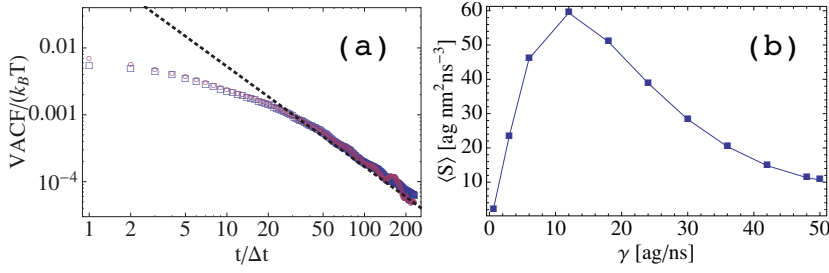


Figure 3.8. (a) Velocity autocorrelation functions of a particle diffusing freely at $T = 330$ K (\circ) and a deterministic particle decelerating from a steady state at $T = 0$ (\square). The dotted line is the asymptotic long-time tail $k_B T (12\rho\sqrt{\pi^3\nu^3})^{-1}t^{-3/2}$ divided by $k_B T$. (b) Rate of dissipation $\langle S \rangle$ due to a 240-node shell is a bounded function of γ . The value of $\langle S \rangle$ corresponding to numerical no-slip ($\gamma > 48$ ag/ns) is less than 0.01% of the rate of dissipation present at the scale of the particle in the absence of the particle. [Publication IV]

of the particle as a function of γ ,

$$\langle S \rangle = \left\langle \sum_i^N S_i \right\rangle = \left\langle \sum_i^N \frac{d}{dt} \left(\frac{1}{2} m \mathbf{v}_i^2 \right) \right\rangle = \left\langle \sum_i^N -\gamma \mathbf{v}_i \cdot (\mathbf{v}_i - \hat{\mathbf{u}}_i) \right\rangle, \quad (3.48)$$

where the last equality follows from a substitution of the negative of Eq. (2.43) for $m d\mathbf{v}_i/dt$. We have measured $\langle S \rangle$ and compared it to the rate of dissipation of kinetic energy in the solvent at the scale of the particle in the particle's absence. That is, we have computed what $D(\mathbf{u})$ of Eq. (2.31) is when $\gamma = 0$ and scaled it by the ratio of volumes (V_{Sphere}/V). A typical measurement is shown in Fig. 3.8(b), which shows, first and foremost, the rate of dissipation $\langle S \rangle$ to be a bounded function of γ . There is zero dissipation when there is no coupling and when there is no slip numerically ($\gamma > 48$ ag/ns), $\langle S \rangle$ is roughly 0.01% of $(V_{\text{Sphere}}/V)D(\mathbf{u})$. Moreover, it has recently been shown that the discrete time implementation has a finite γ which results in conservative forces that ensure zero numerical dissipation. [113]

In addition to the single-particle tests summarized here, we have examined [Publication IV] the consistency of our model in a four-particle setting by comparing it to the predictions of the Rotne-Prager mobility tensor for particle-particle interactions in the regime where the RP tensor is valid. The agreement is quantitative for slowly moving particles, but deviations are observed for fast-moving ones, which could be significant in shear flows. [Publication IV]. The results presented here have been verified recently using a parallel MPI-version of our model [114].

In conclusion, the calibration scheme of our model provides a hydrodynamic radius for the particle whose value is independent of the way it is measured. Deviations due to numerical approximations such as the ex-

tent of the stencil's support are well understood. If torques are not needed and the system is in the dilute limit, point particles may suffice. In this case the compact support determines the native/intrinsic hydrodynamic size of the particle.

4. Dynamics of Single Particles

Here, we apply our coupled LB-MD model to the study of single-particle dynamics in the limit where thermal fluctuations are negligible. We begin by determining analytical expressions for the hydrodynamic drag on oscillating porous spheres in the case of different node distributions. Next, colloidal particles are investigated in a letter-T-shaped microfluidic junction, which is of high experimental relevance.

4.1 Oscillating DBB particles

As the LB method is able to account for local deviations from equilibrium, it is interesting to compare LB simulation results to theoretical predictions of hydrodynamic forces on particles in oscillatory motion. Such comparisons are useful in that they can aid in establishing quantitative limits for the validity of hydrodynamic theories derived based on the Stokes approximation.

In Publication I, we have derived closed-form expressions for the time-dependent hydrodynamic force exerted on a sinusoidally oscillating sphere (Fig. 2.1(a) and Eq. (2.45a)) and shell (Fig. 2.1(b) and Eq. (2.45b)) in the limit of small Re . Our derivation is based on matching the local force on the sphere in terms of the stress tensor (the integrand of Eq. (2.24a)) with the DBB force density of Eq. (2.43). Here we outline the procedure.

The Boussinesq drag force of Eq. (2.20) is derived via an inverse Fourier transform of force components $\hat{\mathbf{F}}(\omega) = \hat{F}_0(\omega)\mathbf{e}_z$,

$$\hat{F}_0(\omega) = -2\pi\rho\omega v R^3 \left[\frac{i}{3} + \frac{3}{2} \frac{1 + kR}{Y^2} \right], \quad (4.1)$$

each of which corresponds to the oscillatory motion $v = v_0 \exp(i\omega t)$ of a sphere of radius R at an angular frequency ω in a quiescent fluid [31]. The parameters k and Y in Eq. (4.1) are defined as $k = (1 + i)\alpha$ and $Y = R\alpha$ where $\alpha = \sqrt{\rho\omega/2\eta}$. Typically (see *e.g.* Ref. [31]), the no-slip, no-flow

boundary condition (BC) on the surface of the sphere is imposed directly on the velocity field obtained from a stream function. The imposition of the BC at that level prevents from investigating the approach to the no-slip limit in terms of the velocity-based coupling of Eq. (2.43).

In our approach, we do not explicitly impose the BC on the velocity field. Instead, we derive an expression analogous to Eq. (4.1) from the well-known stream function ψ_O , which is valid in the exterior of the oscillating particle,

$$\psi_O = h_O(r) v \sin^2 \theta, \quad r \geq R; \quad (4.2a)$$

$$h_O(r) = A/r + (D/k)(1 + 1/(kr))e^{-kr}, \quad (4.2b)$$

where the complex numbers $A = A_{\text{Re}} + iA_{\text{Im}}$ and $D = D_{\text{Re}} + iD_{\text{Im}}$ are unspecified coefficients. We may calculate the components $\sigma_{r\theta}$ and σ_{rr} of stress conveniently in spherical coordinates from

$$u_r = (r^2 \sin \theta)^{-1} \partial_\theta \psi; \quad u_\theta = -(r \sin \theta)^{-1} \partial_r \psi; \quad (4.3a)$$

$$\sigma_{r\theta} = \eta \left(\frac{1}{r} \frac{\partial u_r}{\partial \theta} + \frac{\partial u_\theta}{\partial r} - \frac{u_\theta}{r} \right); \quad (4.3b)$$

$$\sigma_{rr} = -p + 2\eta \frac{\partial u_r}{\partial r}. \quad (4.3c)$$

The pressure, p , is associated with the irrotational part of the flow, *i.e.*, $\psi_{\text{doublet}} = (A/r)v \sin^2 \theta$ in (4.2a), and is solved from $\nabla p = -\rho \partial \mathbf{u}_{\text{doublet}} / \partial t$. The total hydrodynamic force \hat{F} on the particle for arbitrary A and D is given by substituting $\psi = \psi_O$ in Eq. (4.3) using Eq. (2.24a):

$$\hat{F} = \hat{F}_0 \Omega; \quad (4.4a)$$

$$\Omega = \Omega_{\text{Re}} + i\Omega_{\text{Im}} = R^{-3} \frac{4AiY^2 - 4DR^2 e^{-kR}(1 + (1+i)Y)}{9(1 + (1+i)Y) + 2iY^2}, \quad (4.4b)$$

The coefficients A and D for a DBB shell are obtained by equating the expressions for the radial and the tangential forces based on the fluid stress and the DBB force. This gives the following pair of complex equations for A and D which must hold for $0 \leq \theta \leq \pi$ at $r = R$,

$$\begin{cases} -\gamma \lambda_{\text{Sh}}(v_r - u_r) = \sigma_{rr}; \\ -\gamma \lambda_{\text{Sh}}(v_\theta - u_\theta) = \sigma_{r\theta}. \end{cases} \quad (4.5)$$

In the interior of a uniform-density sphere, the nodes exert drag on the solvent. A suitable stream function inside the sphere is

$$\psi_I = h_I(r) v \sin^2 \theta, \quad r \leq R; \quad (4.6a)$$

$$h_I(r) = Br^2 + C \left(\frac{\sinh(k_I r)}{k_I r} - \cosh(k_I r) \right), \quad (4.6b)$$

where $k_I R = \sqrt{\beta^2 + 2iY^2}$ and $B = B_{\text{Re}} + iB_{\text{Im}}$ and $C = C_{\text{Re}} + iC_{\text{Im}}$ are two additional unspecified coefficients. The pressure distribution inside the DBB sphere is more involved as the contribution due to the irrotational part of the force \mathbf{f} must be included. We solve for the complex coefficients A , B , C and D from

$$\tilde{u}_r = u_r, \quad \tilde{u}_\theta = u_\theta; \quad \tilde{\sigma}_{rr} = \sigma_{rr}, \quad \tilde{\sigma}_{r\theta} = \sigma_{r\theta}, \forall \mathbf{r} \in \partial B(t), \quad (4.7)$$

where quantities in the exterior (interior) are denoted with (without) a tilde. The lengthy expressions for Ω both for the shell and the sphere are found in Publication I.

We have compared the normalized amplitude ($\max |F|/F_d$ where $F_d = 6\pi\eta R v_0$) and the phase shift ($\phi \equiv \arg(F(t) - \arg v(t))$) of the hydrodynamic force between our analytical solutions, our LB simulations and those by other workers. These two quantities are conveniently written for the different theories as

$$F(t)/F_d = \sqrt{a^2 + b^2} \cos(\omega t + \phi); \quad (4.8a)$$

$$\phi = -\arccos\left(a/\sqrt{a^2 + b^2}\right); \quad (4.8b)$$

$$a = -\left(\left(1 + Y\right)\Omega_{\text{Re}} - \left(Y + \frac{2}{9}Y^2\right)\Omega_{\text{Im}}\right); \quad (4.8c)$$

$$b = (4/9)Y^2 \left(\left(\frac{1}{2} + \frac{9}{4Y}\right)\Omega_{\text{Re}} + \left(\frac{9}{4Y} + \frac{9}{4Y^2}\right)\Omega_{\text{Im}}\right), \quad (4.8d)$$

for $v(t) = v_0 \cos(\omega t)$. The information about the assumptions on the boundary condition and the particle's internal structure are contained in the quantity Ω specific to each theory. Our time-dependent theory based on force matching reverts back to Eq. (2.45) in the $Y \rightarrow 0$ limit of Eq. (4.8) both for the DBB shell and the sphere. Figures 4.1(a) and (b) compare the phase shift and force amplitude as a function of β between different theories and our LB simulations. For $Y \approx 0.2$, our DBB theory and simulations are in quantitative agreement throughout the range of permeabilities $0 \leq \beta \leq 15$. Looker and Carnie's [115] theory (dot-dashed line) for $F(t)$ is based on a perturbative expansion in the parameter $1/\beta$ for the tangential slip whilst maintaining the no-flow condition ($\mathbf{u} \cdot \hat{\mathbf{e}}_r = 0$ on the surface, $\mathbf{r} \in \partial B(t)$), of the sphere. Their theory agrees quantitatively with ours for the DBB sphere at low permeabilities when the slip coefficient $\xi = 0.9$ in their fluid slip length $\Theta = R/(\beta\xi)$ is set by fitting their expression of the normalized force $F(\beta, \xi)/F_d$ in the $Y \rightarrow 0$ limit to that in Eq. (2.45b). Due to its nature, the perturbative expansion fails for $\beta \leq 2$, which is not surprising. The Darcy model (dashed line in Fig. 4.1) for the

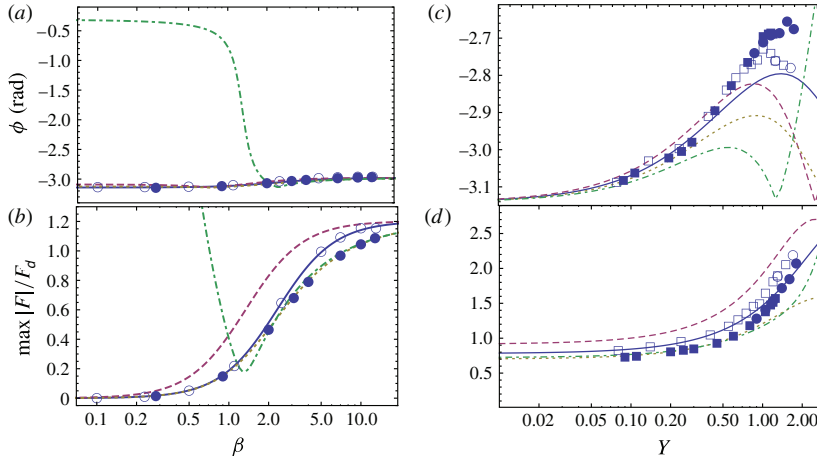


Figure 4.1. (a) Phase shift and (b) normalized amplitude of the oscillating hydrodynamic force as a function of β at $Y = 0.187$ (or, an angular frequency of $\omega = 2\pi/(5000\Delta t) = 1.25$ MHz). The hollow circles correspond to simulations of a shell $(R, N) = (3.3\Delta x, 540)$ with $\Delta x = 100$ nm. The data for a uniform-density sphere $(R, N) = (3.3\Delta x, 2247)$ are plotted as solid circles. (c) Phase shift and (d) normalized amplitude of the oscillating hydrodynamic force as a function of Y (ω was varied to change Y) at fixed $\beta = 4.0$. Simulations in (c) and (d) were performed with a finer mesh resolution, $\Delta x = 77$ nm and time step $\Delta t = 0.59$ ns. The hollow squares and circles correspond to simulations of shells $(R, N) = (4.3\Delta x, 540)$ and $(9.1\Delta x, 2252)$. The data for uniform-density spheres $(R, N) = (4.3\Delta x, 5665)$ and $(9.1\Delta x, 61805)$ are plotted as solid squares and circles, respectively. In all plots, lines correspond to our shell theory (solid line), corrected Darcy theory (dashed), our theory for the uniform-density sphere (dotted) and Looker and Carnie's perturbation theory (dot-dashed) with $\xi = 0.9$. Figure and caption are from Publication I.

uniform-density sphere neglects the second term in Eq. (4.6b) *i.e.*, $C = 0$, which results in an overestimation of the the force.

Figures 4.1(c) and (d) compare the same theories at $\beta = 4$, for which they are clearly distinguished in panels (a) and (b), as a function of $Y = R\alpha \propto \sqrt{\omega}$. The length scale $1/\alpha$ sets the the wavelength and decay length of the disturbance due to the moving particle. We find the agreement between our theory and LB simulations to remain good for $Y \leq 0.5$. However, above $Y = 0.5$ our theories predict smaller amplitudes than those measured in simulation. We were able to rule out finite-size effects (ratio of R to the linear size of the system) as the cause of the discrepancy. Thus, we tentatively suggest the near field description in the linear Stokes theory to break down when $1/\alpha \leq R$, which restricts the validity of the present theories to $Y < 1$.

4.2 Colloids in a T-shaped junction

Microfluidic flow networks typically contain junctions that split a channel into two branches. The solvent in the junction is subject the conservation law $Q_0 = Q_1 + Q_2$ between the flow rates in the inlet and outlets 1 and 2. When solvated particles are driven in the bifurcation asymmetrically *i.e.*, $Q_1 < Q_2$, interesting phenomena such as the Zweifach-Fung effect [116, 117] (ZFE) result. In the effect, the proportion N_1/N_0 of particles, in this case red cells, entering branch 1 is smaller than that of the fluid Q_1/Q_0 . Recently, Doyeux *et al.* [118] performed experiments in order to explain the physics behind the ZFE in a T-shaped bifurcation. In Publication II, we have reproduced their experimental results in the bifurcation of Fig. 4.2(a), which shows several fluid streamlines plotted specifically for $Q_1/Q_0 = 0.35$ in the absence particles and four particle trajectories that leave the streamlines.

As it turns out, the computational model can be used to predict with quantitative accuracy how particles of various shapes, sizes or different degrees of porosity are distributed between the outlets. One may therefore acquire detailed knowledge of the operation of such junctions with the computational scheme as hydrodynamic BCs and surface potentials are freely adjustable. Such considerations are of value to filtration purposes based on different (mechanical) properties and controlled transport at the level of individual colloids. A passive sorting device that does not rely on real-time monitoring would be highly desirable. An important consideration in realizing one is direct and indirect fluid-mediated colloid-colloid interactions, which we have examined in Publication II.

How particles split between the branches is mainly dictated by the inlet coordinate x at which they approach the bifurcation [118]. In fact, the proportion Q_1/Q_0 of fluid going left in Fig. 4.2(a) is related to the fluid-separating streamline located at x_0 in the inlet sufficiently far from the junction. It is determined from the velocity profile of an incompressible fluid as

$$Q_1/Q_0 = \int_0^{x_0} u_z(x)dx / \int_0^W u_z(x)dx, \quad (4.9)$$

where W is the width of the inlet. The coordinate x_0 is plotted versus Q_1/Q_0 in Fig. 4.2(b) as a solid thick line. The coordinate x_0 does not, however, determine which direction colloidal particles flow. The location x_0^* of the particle-separating streamline can be distinctly different from x_0 . In Fig. 4.2(a), particle trajectories close to x_0^* have a right angle as the

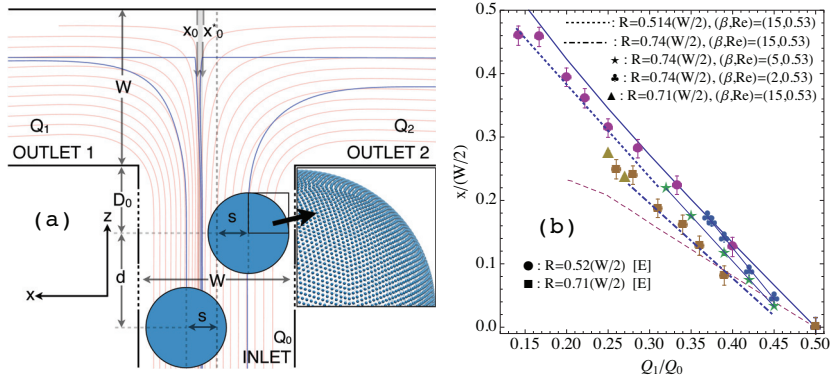


Figure 4.2. (a) Schematic of the T-bifurcation, where the fluid-separating (x_0) and the particle-separating coordinates (x_0^*) are functions of Q_1/Q_0 . (b) Location of x_0 (thick solid line) and x_0^* (dotted and dot-dashed lines, symbols) versus Q_1/Q_0 for different particle radii (R) and levels of porosity (β). Data below x_0 indicate that x_0^* is located right of x_0 in panel (a). Our theoretical model (dotted and dot-dashed lines) agrees with experimental “[E]” results [118] (● and ■). The more porous the particle is (dot-dashed line, ★, ♣) the farther left it needs to reside in the inlet for it exit through outlet 1. Comparing Doyeux and coworkers’ 2D model (dashed line) to their experiments indicates that a full 3D description (our model, dot-dashed line) is needed to account for the experiments. Figures are from Publication II.

particle collides with the top wall. For other offsets the particles follow streamlines more faithfully. In its absence, the solvent flows left (right) when located at $x > x_0$ ($x < x_0$). A particle flows left (right) when started at $x > x_0^*$ ($x < x_0^*$). Within the narrow grey region ($x_0 > x > x_0^*$), solvent flows right and a particle left. We have found our LB-MD method to reproduce Doyeux and coworkers’ measurements for two different particle radii. Thermal fluctuations can be neglected in this study as the results will show. We used the trilinear stencil to couple DBB shells with $(2R, N) = (0.514W, 10692)$ and $(0.74W, 22092)$ using $\beta = 15$ in order to approximate the no-slip limit. These data are shown as a dotted and a dot-dashed line in Fig. 4.2(b). The overall finding is that the particle can be right of the fluid-separating coordinate ($x_0 > x_0^*$) for it to enter the low-flow-rate branch, and the larger the particle is the bigger the difference $x_0 - x_0^*$ is. The agreement with experiments is very good unlike in the theoretical 2D model used in Ref. [118].

The DBB model can be used to determine at least qualitatively the effect of permeability ($\propto \beta$) on x_0^* . As β is decreased, the coordinate $x_0^*(\beta)$ approaches x_0 . This observation allows separation of particles based on porosity by focusing them at x , for which impermeable particles go left and porous ones right. Similarly, splitting a focused stream of imperme-

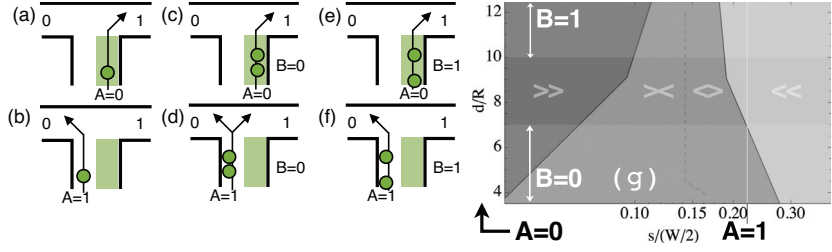


Figure 4.3. (a-b) Single-particle NOT gate. (c-f) Two-particle NAND gate. (g) Example regions corresponding to different values of the binary variables: $s < 0$ ($A = 0$), $s/(W/2) = 0.22$ ($A = 1$), $d/R < 7$ ($B = 0$) and $d/R \geq 10$ ($B = 1$). Figures are from Publication II.

able particles appears to be feasible based on the radius R alone. For instance, if we pick the coordinate $x = 0.22(W/2)$ and drive the junction at $Q_1/Q_0 = 0.3$, a particle of $2R = 0.74W$ goes left and $2R = 0.514W$ goes right.

The aforementioned examples of filtration assume the focused stream to have large enough gaps such that particle-particle correlations can be neglected. To understand the correlations, we have examined how a pair of particles with a common offset s separated initially by d flows through the junction. The four outcomes, both go left ($<<$), both go right ($>>$), the leading particle goes left and the trailing particle right ($<>$) or vice versa ($><$), can be gathered into a two-particle phase diagram in terms of s and d . The diagram is plotted in Fig. 4.3(g) for $Q_1/Q_0 = 3/8$ and it suggests that for sufficiently large d/R , the $<>$ and $><$ phases disappear. The phase diagram stays qualitatively similar as the channel Reynolds number is varied between 0.5 and 5.

We have also proposed that operations of binary logic can be realized by using the initial conditions $s/(W/2)$ and d/R as the control variables. The definitions of two binary variables, A and B , as functions of s and d are given in Fig. 4.3(g). A logic NOT gate illustrated in Fig. 4.3(a)-(b) follows if the left/right branch is associated with the outcome 0/1 since they correspond to $A = 1$ and $A = 0$, respectively. Two-particle flow characterized by A and B can be turned into a NAND gate, for which $(A, B) = (1, 1) \mapsto 0$, but other combinations of A and B are understood as a binary 1. Serial gate configurations may require sheath flow and/or additional focusing, but in principle any binary operation can be implemented as the NAND gate is universal.

In conclusion, we have validated the coupled LB-MD model against experimental results on colloid flow in a bifurcation and found it to yield

good agreement on how particles are distributed between the outlets. We have observed the particle porosity to affect the outlet distribution such that highly porous particles are increasingly prone to entering the high-flow-rate outlet. Bifurcations are key components in complex microfluidic networks. If they are to function analogous to electronic circuits, a detailed understanding of the operation of each component is necessary. Here, we have found two-particle correlations to alter the outlet distribution of focused particles both as a function of the distance at which they approach the junction and their common offset from the centerline. Natural extensions of this work would be to examine three-particle correlations and serial/parallel gate configurations.

5. Transport Properties of Polymers

5.1 Polymer dynamics in bulk

We have further validated our coupled LB-MD algorithm in Publication III by performing standard tests on linear polymers in a dilute bulk solution in the presence of thermal fluctuations. The monomers are constructed from 30-node shells similar to those in Fig. 3.3 and coupled to the LB fluid using the trilinear stencil. The CM coordinates of consecutive monomers are linked with a nonlinear FENE potential [119]

$$U_{\text{FENE}}(r_{mn}) = -\frac{1}{2}kR_0^2 \log(1 - r_{mn}^2/R_0^2) \delta_{|m-n|,1}, \quad (5.1)$$

where $r_{mn} = |\mathbf{r}_m - \mathbf{r}_n|$, $k = 30\epsilon\sigma^{-2}$ is the stiffness of the bond, $R_0 = 1.5\sigma$ is the bond's maximal extension and δ_{ab} is the Kronecker delta function. The excluded-volume effect is modeled using the pairwise, truncated and shifted 12-6 Lennard-Jones (LJ) potential

$$U_{\text{LJ}}(r_{mn}) = 4\epsilon \left[(\sigma/r_{mn})^{12} - (\sigma/r_{mn})^6 + 1/4 \right] \Theta(2^{1/6} - r_{mn}/\sigma), \quad (5.2)$$

between all pairs of beads. The energy and length scales are set by $\epsilon = k_{\text{B}}(300\text{ K})$ and $\sigma = 1.0\text{ nm}$, respectively, and the Heaviside step function $\Theta(x)$ zeroes the potential beyond its repulsive part. The monomers obey Newton's equation of motion,

$$m\ddot{\mathbf{r}}_m = - \sum_{n \neq m} \nabla_m U(\mathbf{r}_m, \mathbf{r}_n) + \mathbf{F}_m, \quad (5.3)$$

where $U = U_{\text{FENE}} + U_{\text{LJ}}$ and \mathbf{F}_m is the coupling between the m th monomer and the LB fluid as given by Eqs. (3.28) and (3.22). Our measurements of the Flory exponent ν based on the static structure factor are shown in Fig. 5.1(a). We find $\nu \rightarrow \nu_\infty = 0.586 \pm 0.005$ in the limit $N \rightarrow \infty$, which agrees well with the value of 0.588 ± 0.001 by Sokal *et al.* [80]. The value

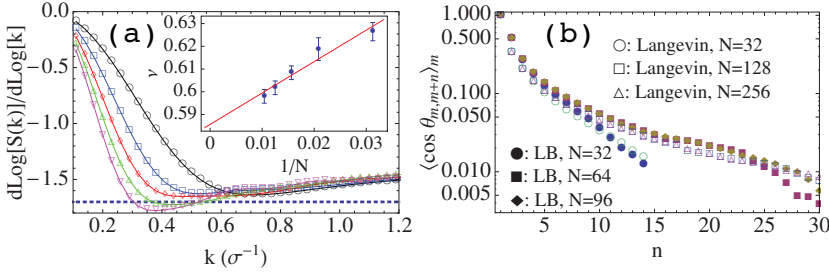


Figure 5.1. (a) Extraction of the Flory exponent ν and finite-size scaling gives an asymptotic estimate of $\nu = 0.586 \pm 0.005$. (b) Corresponding LB and Langevin chains have very similar bond-bond correlations apart from the first few bonds for which the LB chain appears stiffer. Figures are from Publication III.

of ν is larger than ν_∞ for short chains, which can be interpreted as a sign of local stiffness. The static bond-bond correlation function,

$$\langle \cos \theta_{m,m+n} \rangle_m \equiv \left\langle \frac{\mathbf{r}_{m+1} - \mathbf{r}_m}{|\mathbf{r}_{m+1} - \mathbf{r}_m|} \cdot \frac{\mathbf{r}_{m+n+1} - \mathbf{r}_{m+n}}{|\mathbf{r}_{m+n+1} - \mathbf{r}_{m+n}|} \right\rangle_m, \quad (5.4)$$

is a temperature-dependent quantity that should reveal whether our LB solvent serves as an isothermal heat bath for the polymer model introduced above. We compare the LB results to ones from using a Langevin thermostat to thermalize a chain with the same MD parameters. Figure 5.1(b) indicates that locally, $n < 5$, the LB polymer is expectedly stiffer due to finite monomer size, but for $n > 5$ the decay is very similar between the two models. This is an indication of the fact that the chain in our model is at the desired temperature.

The relaxation times τ_p are plotted in Fig. 5.2(a) as a function of the ratio of the mode number, p , to the degree of polymerization, N , for chains of different length. The Rouse modes suggest that long-range interactions are present and, in the long-chain limit, the Rouse modes predict a value of $z = 2.97 \pm 0.04$ in agreement with the Zimm model.

The macroscopically observed fluctuation-dissipation theorem with a first-order finite-size correction due to PBCs reads

$$D_{\text{cm}} = \frac{k_B T}{6\pi\eta} \left(\frac{A}{R_g} - \frac{B}{L} \right) \quad (5.5)$$

in the dilute limit. The CM diffusion coefficient of the polymer is measured using Eq. (2.61) and the temperature and the shear viscosity are set by the LB bath. Figure 5.2(b) shows measurements of D_{cm} for different N as a function of the inverse of the linear system size. Fits to data yield an average value of $B = 2.8 \pm 0.05$, which is consistent with that in Section 3.2.4 for the Brownian particle. Equation (5.5) differs formally from Eq. (3.47) only in that the hydrodynamic radius is replaced by

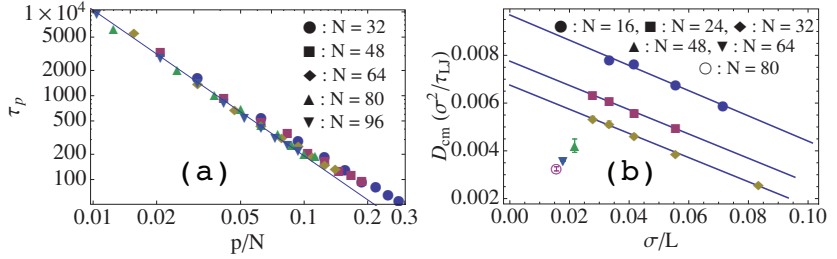


Figure 5.2. (a) The slope of the fit equals $z\nu = 1.74 \pm 0.01$, which gives $z = 2.97 \pm 0.04$, when the asymptotic value $\nu = 0.586$ from Fig. 5.1 is used. The relaxation times are reported in Lennard-Jones units. (b) Extraction of the coefficient in the finite-size correction yields $B = 2.8 \pm 0.05$. Figures are from Publication III.

the expression R_g/A . This is because the polymer is not a solid sphere of radius R_g , but its hydrodynamic radius in terms of equilibrium dynamics is $R_H = R_g/A$, where A is a model-dependent proportionality constant. A bead-spring model in continuum space is expected to have $A = 1.63 \pm 0.01$ [81]. The data of Fig 5.2(b) give $A = 1.67 \pm 0.05$, which is obtained by using $B = 2.8$ for the chain lengths without measurements as a function of $1/L$, and by measuring R_g according to Eq. (2.57). Based on these findings, we conclude that our polymer obeys the fluctuation-dissipation theorem without any added adjustable parameters.

Interestingly, SRD simulations [83] predict the existence of an additional term, $D_1 = k_B T / (\xi N)$, on the right-hand side of Eq. (5.5). Theoretically, the term arises from Kirkwood theory [120], which assumes clear time scale separation, which makes D_1 observable at short times, but not in the long-time limit. We observe no such term to be present in our simulations, which can be argued by not having any slip on the monomer surface.

We have also validated our polymer model against the theoretical scaling prediction of Eq. (2.63) in great detail. Winkler and coworkers [82] have argued that z should equal $8/3$ in the laboratory frame for $kR_g \gg 1$ in the presence of hydrodynamic interactions. The argument has been confirmed earlier by simulation [83] and our results concur with theirs. Figure 5.3 shows our findings. In the laboratory frame of reference (panel (a)) data for a 32-bead chain show a clear collapse onto the scaling function $F(x)$ with $z = 2.43$ for $k \in [\sigma^{-1}, 2.4\sigma^{-1}] = [2\pi/(1.6R_g), 2\pi/(2.62\sigma)]$. The corresponding value for a 64-bead chain was found to be 2.54 ± 0.02 . When $S_{\text{cm}}(\mathbf{k}, t)$ of Eq. (2.62b) is evaluated from the same sets data, the data collapse best for $z = 3.0$ (panels (b) and (c)). Interestingly, the function

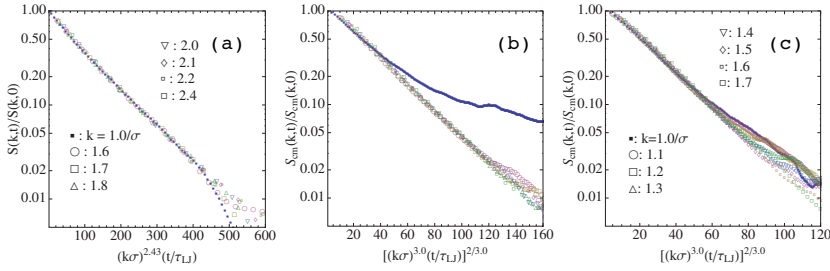


Figure 5.3. (a) Dynamic structure factor for $N = 32$ collapses best for $z = 2.43$ in the laboratory frame of reference whereas (b) in the CM frame the collapse takes place for $z = 3$. (c) The CM collapse for $N = 64$ is reasonable, but it suffers from insufficient statistics. Figures are from Publication III.

$S_{\text{cm}}(1/\sigma, t)$ does not collapse with the other data. This can be understood on the basis that beads are roughly within a distance of R_g away from the center of mass but, in the laboratory frame, the characteristic length scale doubles to $2R_g$, which is a common separation between pairs of beads. The collapse in the CM frame for $N = 64$ was found to take place over a narrower range of k values. By computing off-diagonal elements of the Rouse matrix, $C_{p,q}(t) \equiv \langle \mathbf{X}_p(t+s) \cdot \mathbf{X}_q(s) \rangle_s$ with $p \neq q$, we noticed correlation levels of $C_{1,q}(t)/C_{1,1}(0) \approx 0.1$ for $N = 64$ and $q = 1, \dots, 5$ even at $t = 2000 \tau_{LJ}$. The corresponding ratios for $N = 32$ had dropped to $\mathcal{O}(10^{-2})$ to $\mathcal{O}(10^{-3})$ at $t = 100 \tau_{LJ}$. We were limited by the unavailability of a parallel implementation of our model in running the bulk simulations for which reason the statistics in Fig. 5.3(c) are limited at longer time scales.

5.2 Polymer dynamics in slitlike confinement

Many of the unique physical properties of nano and microfluidic systems stem from reduced dimensionality at least in one direction. We have recently examined the effect of confinement on polymer statics and dynamics in Publication V both in the absence and the presence of hydrodynamic interactions. The confinement is imposed in the z direction in the form of parallel plates, which are illustrated schematically in Fig. 5.4(a). The degree of confinement is defined as

$$C = R_g/L_z, \quad (5.6)$$

where R_g is the chain's radius of gyration measured in bulk using Eq. (2.57). The plate separation L_z is defined based on the locations z_1 and z_0 of planar LJ walls, whose functional form is given by Eq. (5.2) with a monomer-wall length scale set to $\sigma_{\text{mw}} = 1.87\sigma = 2.8 \text{ nm}$ and $\epsilon = k_B(300 \text{ K})$,

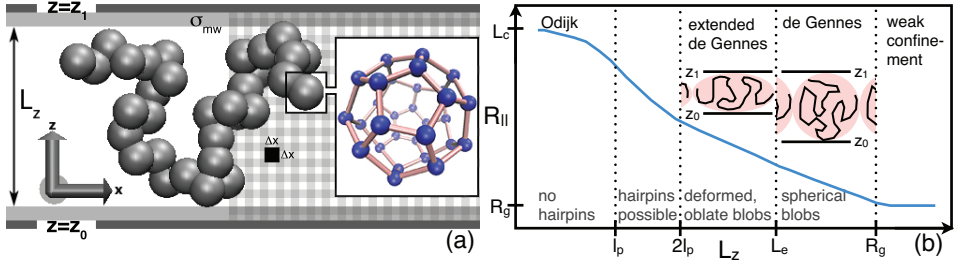


Figure 5.4. (a) A schematic of the parallel-plate geometry. Planar confinement restricts the polymer into a thin film. Panel (a) is from Publication V. (b) A characterization of confinement regimes in terms of planar size $R_{||}$ of the chain as a function of plate separation L_z .

but the distance dependence in the interaction is only in the direction normal to the wall. The confinement needs to be imposed independently on the MD and the LB part of the model. This is convenient as it allows to characterize the effect of different hydrodynamic BCs on measurable quantities. We have studied two types of confinement in Publication V. In the first, which we abbreviate as q2D-LB, the confinement is imposed both on the fluid and the polymer, which corresponds to a slit between two solid walls. The fluid boundaries are implemented using the mid-grid bounceback rule [96]. In the second, abbreviated as 3D-LB, only the polymer is confined using the LJ potential and the LB solvent is in a cubic box with periodic boundary conditions. This type of confinement is feasible in experiment *e.g.*, by optical trapping.

The walls break the isotropy of the bulk system, which is why the size of the polymer cannot be characterized by R_g alone. Following Ref. [121], we define the size of the polymer parallel, $R_{||}$, and perpendicular, R_{\perp} , to the walls through

$$R_{||}^2 \equiv \left\langle \sum_{i=1}^3 \lambda_i (1 - |\hat{\lambda}_i \cdot \hat{z}|^2) \right\rangle; \quad R_{\perp}^2 \equiv \left\langle \sum_{i=1}^3 \lambda_i |\hat{\lambda}_i \cdot \hat{z}|^2 \right\rangle, \quad (5.7)$$

where λ_i are the eigenvalues of the tensor of gyration Q and $\hat{\lambda}_i$ are the corresponding unit-normalized eigenvectors. The static and dynamic structure factors are probed similarly parallel, $S(k_{||}, t)$, and normal, $S(k_{\perp}, t)$, to the walls using $\mathbf{k}_{||} = k(\hat{x} + \hat{y})/\sqrt{2}$ and $\mathbf{k}_{\perp} = k\hat{z}$.

The obvious limits of confinement are its complete absence ($C \rightarrow 0$) and confinement onto a two-dimensional plane $C \rightarrow \infty$. Experimental and theoretical investigations [122] have established intermediate regimes, for which the planar extension $R_{||}$ depends on the contour length ($L_c \sim N$) and the persistence (l_p) length of the polymer as well as the plate separation and even the width of the contour. The de Gennes regime [74] is

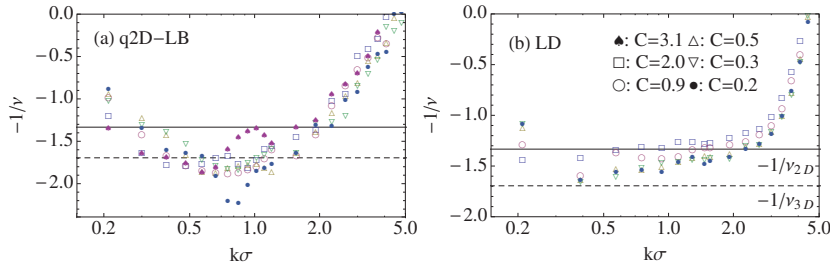


Figure 5.5. The exponent $-1/\nu$ versus $k\sigma$ based on $S_{\parallel}(k) \sim k^{-1/\nu}$ for a chain at different levels of confinement. The data are for a 96-bead chain from (a) q2D-LB and (b) LD simulations. The solid/dashed horizontal line indicates the value corresponding to the 2D/3D scaling exponent. Panels are from Publication V.

typically defined as the interval $1 < C \ll R_g/l_p$, where the contour gets distributed into blobs of linear size L_z dictated by the plate separation. Once L_z is decreased further, the excluded-volume interaction within a blob drops below $k_B T$ [123] and the blob becomes oblate. Plate separation $l_p < L_z < 2l_p$ make single hairpins possible, whereas in the Odijk regime [124], $L_z < l_p$, the chain can only deflect from the confining walls.

A direct comparison with experiments spanning from the de Gennes to the Odijk regime would require one to simulate the same chain over two decades of C . The Odijk regime presumes a model that resolves structure at scales smaller than l_p . Such a requirement would either make the number of beads computationally impractical or the size Δx of the LB unit cell unphysically small. Our polymer model has a microscopic cutoff set by the LJ length scale σ and the hydrodynamic radius R_H of the monomer. Also, 10 lattice LB sites are required for sufficiently accurate reproduction of, *e.g.*, the Poiseuille velocity profile between the walls. The chain's R_g and contour length are well-defined quantities. These considerations limit the range of confinement to $C \leq 3.1$ in Publication V.

Blob theory [74] predicts $R_{\parallel}/R_g \sim C^{\beta}$ to hold in the de Gennes regime, where the scaling exponent $\beta = \nu_{2D}/\nu - 1 \approx 0.276$. We performed measurements of R_{\parallel} versus $1/C$ in the case of two thermostats: our LB solvent and Langevin dynamics (LD). We found R_{\parallel} to scale with values $\beta = 0.24 \pm 0.03$ for LB and 0.21 ± 0.03 for LD, which are similar to those found in both computational and experimental studies listed in Publication V. However, the range of values of C is limited to less than a decade which is why the existence of the de Gennes scaling regime cannot be established conclusively. The dynamics differ in how they approach the 2D limit as C increases. We quantify the approach by plotting $-1/\nu = \partial[\log S(k)]/\partial[\log k]$ as a function

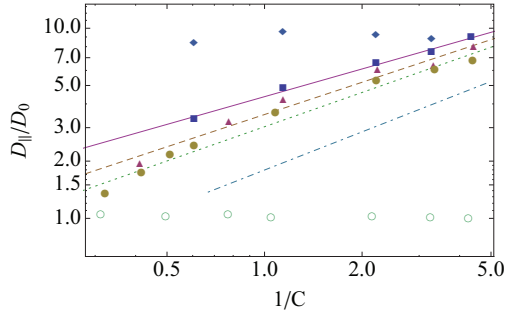


Figure 5.6. The normalized planar diffusion coefficient versus $1/C$ in q2D-LB for $N = 32$ (squares), 64 (triangles) and 96 (solid circles). We also show data points in 3D-LB for $N = 32$ (diamonds) and LD for $N = 96$ (hollow circles). The lines are fits to q2D-LB data that scale as $D_{\parallel} \sim C^{-0.48 \pm 0.04}$ ($N = 32$, solid line), $C^{-0.56 \pm 0.04}$ ($N = 64$, dashed line) and $C^{-0.60 \pm 0.04}$ ($N = 96$, dotted line). The dot-dashed line is the blob theory prediction $D_{\parallel} \sim C^{-2/3}$. The data are scaled by $D_{\text{cm}}^{(R)}$ of Eq. (2.61) corresponding to $N = 96$ and $\xi = 6\pi\eta R$, where R is the hydrodynamic radius of the monomer.

of k in Fig. 5.5. The data suggest the transition to the 2D limit takes place closer to the Odijk regime (large C) for the LB model than it does for the LD model. There are, however, subtle differences in the level of confinement for the two models related to wall-monomer interactions and point (LD) versus finite (LB) monomer size.

The transition between two and three dimensions should also be reflected in the value of the dynamical scaling exponent $z = 2 + \nu_D/\nu$ from $z = 2$ in 2D to $z = 3$ in 3D with hydrodynamic interactions as detailed in Section 2.5. The 2D limit has been studied earlier in detail and convincing agreement with the value of $z = 2$ was established. [76] We have examined the transition by measuring $S_{\parallel}(k, t)$ for a 32-bead chain. The measurements yield values from $z = 2.2 \pm 0.1$ to $z = 2.7 \pm 0.1$ as confinement decreases from 1.6 to 0.3, which are physically reasonable. The perpendicular quantity $S_{\perp}(k, t)$ fails to collapse for $C = 1.6$, but at $C = 0.3$ it reverts to the expected 3D scaling law with $z = 3$ [Publication III and Publication V].

Another dynamic quantity of interest is the planar diffusion coefficient D_{\parallel} defined using Eq. (2.60) for $\mathbf{r}_{\parallel, \text{cm}} = (x_{\text{cm}}, y_{\text{cm}})$. The blob theory predicts a scaling relation of the form $D_{\parallel} \sim C^{-\alpha}$ with $\alpha = 2/3$ in the long-chain limit. Experiments by different workers [125, 126] covering ranges of confinement up to $0.4 < C < 25$ have resulted in values $\alpha \approx 0.5$. Our model with confinement imposed both on the solvent and the polymer yields values of α ranging from 0.48 ± 0.04 ($N = 32$, solid squares in Fig. 5.6) to

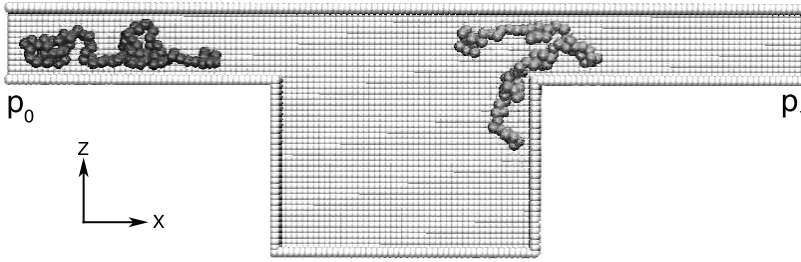


Figure 5.7. A side profile of the system geometry with one of the side walls removed. Polymer motion is biased to the right ($+x$ direction) and the bottom of the pit is located at $z=0$ and the floor of the narrow section is at $z = 32$ nm. The $+y$ axis is into the plane of the page. A pressure differential $\Delta p = p_1 - p_0 > 0$ is present between the inlet and the outlet. The schematic was created using VMD. [127]

0.60 ± 0.05 ($N = 96$, solid circles) to 0.66 ± 0.05 ($1/N \rightarrow 0$ via finite-size scaling) the last of which agrees with the blob theory prediction. When D_{\parallel} is measured with confinement on the polymer only, no dependence on C is observed either for the LB (diamonds) or the LD solvent (hollow circles), which reveals the importance of momentum absorption due to the no-slip boundary condition. This suggests Langevin dynamics is not a viable option for studying polymer dynamics in equilibrium or with small driving biases between solid walls as a function of C as it gives qualitatively incorrect results. The LD results are, however, qualitatively similar to having confinement only on the MD polymer.

5.3 Polymer transport in nanochannels

Biopolymer transport in nanofluidic and microfluidic channels involves competition between external forcing, surface interactions and, possibly, entropic trapping. Careful adjustment of the relative magnitudes between these factors can result in unique transport characteristics such as contour-length based mobility [128, 24] and pit-to-pit hopping [23, 24] in pressure-driven flow and electrophoretic mobility differences for long DNA molecules [129, 130]. Electric field-driven separation techniques have also been optimized for DNA [131]. Mikkelsen *et al.* [24] demonstrated recently pressure-driven DNA to exhibit clear mobility differentiation both as a function of the degree of polymerization, N , and internal structure (linear and ring polymers with the same N). Their experimental arrangement consisted of an array of troughs in which the chain was trapped. In this work, we examine computationally whether a channel

with sidewalls and alternating sections of narrows and pits can be used for pressure-driven polymer filtration. The change in the channel's cross section facilitates swelling of the chain in a time frame defined by the pressure differential, and it leads to a non-trivial effect on chain mobility as a function of the degree of polymerization and chain structure. The problem is challenging as the trapping regime may correspond to a very small bias, or Deborah number $De \ll 1$, defined as the ratio $\tau_p/\tau_{\text{flow}}$ of the polymer relaxation time τ_p to the geometric time scale τ_{flow} the fluid takes to traverse the pit region. Until now, a transversal (electric) field that tends to direct the polymer to the bottom of the pit has not been considered for increased mobility differentiation. We indicate how such an arrangement is able to induce differentiation for chains that exhibit no mobility difference in the absence of the field.

On the theoretical side, we test the validity of the threshold of minimal momentum flux needed for a polymer to enter a narrow pore [132] in our geometry. The threshold was recently found to be accurate in computer simulations under bodyforce-driven flow [133]. However, a body force is not the same as a pressure difference in a channel of varying cross section as the pressure drop per unit length decreases as the cross-sectional area increases.

We define polymer mobility μ as

$$\mu = \langle v_x \rangle / \Delta p, \quad (5.8)$$

where $\langle v_x \rangle$ is the mean velocity of the polymer in the x direction and $\Delta p = p_0 - p_1 > 0$ is the pressure differential between the inlet and the outlet of the system depicted in Fig. 5.7. The pressure difference is set as a skew-periodic BC in the equation of state (see text below Eq. (3.19)) through the average density difference, $\Delta p = \Delta \rho v_s^2 = (\rho_0 - \rho_1) v_s^2$.

The overall mobility of the polymer in our system is a weighted average of the mobility in the narrow region, in the pit region and in the interfaces between the two regions. It is of interest to understand which of these four aspects contributes the most to that in Eq. (5.8). The polymer mobility of Eq. (5.8) depends on the relative magnitude of the pressure differential and thermal fluctuations, which determines how easily the polymer can move perpendicular to flow streamlines. To change the ratio of thermal fluctuations to the driving force, we vary the pressure differential that results in a mean momentum flux \bar{j}_x that we measure over a cross section

A of the channel and average over time:

$$\bar{j}_x A = \left\langle \int_A \rho(\mathbf{r}) u_x(\mathbf{r}) dA \right\rangle_t. \quad (5.9)$$

Polymer entry from the pit to the narrow region has been examined theoretically by Sakaue *et al.* using the blob theory [132]. Their result is that the momentum flux is able to make a flexible polymer enter a narrows smaller than R_g providing it exceeds a threshold velocity flux specific to the process. We cast the threshold here in terms of the momentum density, j_c , as

$$j_c A \simeq k_B T / \nu, \quad (5.10)$$

where ν is the kinematic viscosity of the solvent. We emphasize that Eq. (5.10) is independent of pore details and the degree of polymerization N and no assumptions about them were made in deriving it. Equation (5.10) is obtained by assuming large enough an N and the process to be slow enough to be describable by a free energy that exhibits a barrier of entry as a function of the partial length of the pore occupied by the polymer.

In the absence of bias, the barrier of entry is dictated by the free energy difference, ΔF , between the sections. Experiments can have a large ΔF by imposing Odijk confinement (see Fig. 5.4(b)) in the narrow and de Gennes confinement in the pit. Such a contrast is not feasible for the simple bead-spring model we employ here.

Our system consists of a channel with alternating segments of square and rectangular cross sections. The geometry of the channel is shown schematically in Fig. 5.7. In terms of the space available for the polymer, the narrows has a square cross section of size $L_y \times h = 4.9\sigma \times 4.9\sigma$ unless otherwise noted and the pit region has a rectangular cross section $L_y \times L_{z,\text{pit}} = 4.9\sigma \times 25.6\sigma$. The polymer model is identical to that in Section 5.2. The length of the pit and of the narrows in the x direction are $L_{x,\text{pit}} = 27.6\sigma$ and 69.3σ , respectively. The walls that confine the polymer in the channel are made out of LJ beads with ϵ as above and distance parameters set to $\sigma_{\text{mw}} = 1.87\sigma$. We follow the motion of FENE polymers consisting of $N = 1$ to 96 beads moving through the channel with a periodic boundary condition (PBC) splitting the narrow into halves of equal length. The location of the PBC is placed as far away as possible from the pit region.

An important physical distinction is that the pressure drop in the pit is less than that in the narrow section. Unlike a body force, a pressure boundary condition allows the fluid to slow down when the size of the

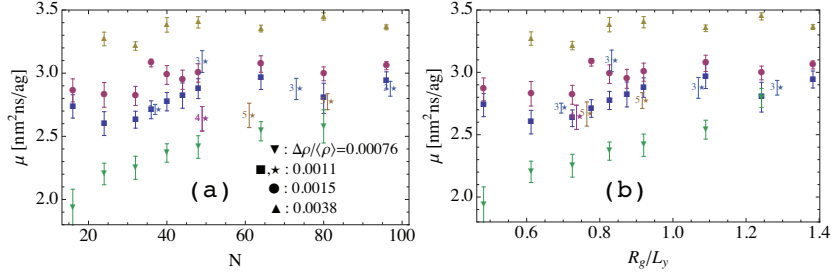


Figure 5.8. Polymer mobility μ in the x direction as a function of (a) the degree of polymerization N and (b) the relative size of the chain. All polymers are linear except the star symbols correspond to f -branch $f \in \{3, 4, 5\}$ star polymers of $N = f N_f + 1$ monomers with $N_f = 12, 16, 24$ and 32 .

channel's cross section increases. It is important to remember that a body force is not the same as a pressure difference as resistance to flow drops in the pit region due to decreasing velocity whilst mass flux stays constant. The kinematic viscosity in our simulations is $\nu = 1403 \text{ nm}^2 \text{ ns}^{-1}$, which is 1.4 times that of water.

To compute the polymer mobility, we have analyzed traces of the x component of the polymer's CM coordinate, x_{cm} , versus time. We adjust the relative strength between entropic trapping and advection by changing the pressure difference. To get an idea of the magnitudes involved, we vary the density difference between the ends of the system relative to the mean density from $\Delta\rho/\langle\rho\rangle = 7.6 \cdot 10^{-4}$ to $3.8 \cdot 10^{-3}$. In the corresponding L_z by h square channel without the pit, this range of density difference would result in a flow profile, whose mean velocity $\langle u \rangle$ relative to thermal velocity varies between $\langle u \rangle / (\sqrt{k_B T / (\langle \rho \rangle \Delta x^3)}) = 7.6 \cdot 10^{-4}$ and $3.8 \cdot 10^{-3}$. The mean bias in the velocity field is chosen sufficiently small relative to velocity fluctuations in the solvent in order to allow for spontaneous particle migration across streamlines. The Reynolds number defined as $Re \equiv L_y \langle v_x \rangle / \nu$ varies between 0.002 and 0.016. We define also the Péclet number $Pe \equiv L_y \langle v_x \rangle / D$, where D is the diffusion coefficient of the chain in corresponding level of slitlike confinement. We find $Pe = 1, \dots, 25$ for the range of pressure differentials considered.

We have determined polymer mobility μ at different degrees of polymerization, N in the case of linear and star polymers. Mobility allows us to characterize polymer movement at different pressures on an equal footing. This measurement is interesting since, if the mobility were to depend on N , our system could be applied to polymer filtration based on their length. Figure 5.8 shows the polymer mobility corresponding to

$\Delta\rho/\langle\rho\rangle = 0.00076$ (down triangles), 0.0011 (squares and stars), 0.0015 (circles) and 0.0038 (up triangles). The star symbols correspond to f -branch star polymers of $N = f N_f + 1$ monomers with $N_f = 12, 16, 24$ and 32. Other polymers are linear. Traces of entropic trapping cannot be seen at the largest pressure difference (up triangles) as the pressure dominates the entropic repulsion at the entrance to the narrow. This leads to a value of μ that is independent of N . However, at the second to lowest pressure difference (squares), the situation becomes more interesting as the mobility has a minimum at $N = 24$ and increases nearly monotonically up to $N = 64$. The result is significant as the error in the statistical averages is smaller than the difference in the mobilities $\mu(N = 24)$ and $\mu(N = 64)$. Most significantly at the lowest feasible pressure differential, the downward-pointing triangles show a clear increase $\mu(N = 80)/\mu(N = 16) \approx 1.45$ in mobility as N increases from $N = 16$ to $N = 80$.

We have found two explanations for the non-monotonicity for intermediate Δp . On the one hand, the CM of a short chain is able to get closer to the bottom wall, for which reason it can move vertically more in the pit. On the other hand, too short a chain will not be able to exert any repulsive entropic force at the entry to the narrow, whereas the free energy barrier can be large for a long chain. These aspects are visible in the probability distribution of the z_{cm} coordinate in the pit region for $N = 16, 24, 32$ and 48 even at $\Delta\rho/\langle\rho\rangle = 0.0011$ in Fig. 5.9. The distributions in Fig. 5.9 are fully consistent with the corresponding squares in Fig. 5.8 as the z component of the chains' CM coordinate z_{cm} ($\langle z_{\text{cm}} \rangle = \int_{z=0}^{z=Lz} z P(z) dz$) is ordered as $\langle z_{\text{cm}}(24) \rangle < \langle z_{\text{cm}}(32) \rangle < \langle z_{\text{cm}}(16) \rangle < \langle z_{\text{cm}}(48) \rangle$ and so are the corresponding mobilities. The inset of Fig. 5.9 shows chain mobility in the pit defined as $\mu_{\text{pit}} = \langle v_{x,\text{pit}} \rangle / \Delta p$ versus N . The dependence of μ_{pit} on N becomes stronger as $\Delta p/p_0$ drops from 1.0 to 0.5. The pit-to-slit translocation time for the chain increases linearly with N , which is consistent with the single file being the most prevalent mode of translocation for long chains: $R_g/L_y \gtrsim 1$.

The significance of Fig. 5.8 can be understood by relating it to experiments in terms of the degree of confinement and the geometry of the system. Stein *et al.* [128] have determined experimentally the mobility of double-stranded DNA molecules in pressure-driven flow in slitlike silica channels of height between $d_{\text{min}} \approx 0.2 \mu\text{m}$ and $d_{\text{max}} \approx 3.8 \mu\text{m}$. They observed the mobility of $4 \mu\text{m}$ to $22 \mu\text{m}$ -long DNA to be the same at d_{min} (due to identical dispersion characteristics and concentration profiles across

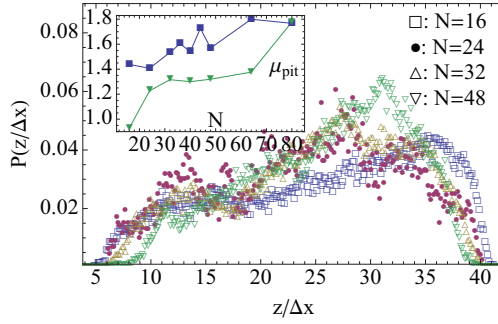


Figure 5.9. Probability distribution of the z component of the CM of the chain in the pit region corresponding to $\Delta\rho/\langle\rho\rangle = 0.0011$ (squares in Fig. 5.8). The averages of the distribution are $\langle z_{\text{cm}}(16) \rangle \approx 25.6$, $\langle z_{\text{cm}}(24) \rangle \approx 24.1$, $\langle z_{\text{cm}}(32) \rangle \approx 25.1$ and $\langle z_{\text{cm}}(48) \rangle \approx 26.5$. Inset: polymer mobility in the pit versus N corresponding to $\Delta\rho/\langle\rho\rangle = 0.0015$ (squares) and $\Delta\rho/\langle\rho\rangle = 0.00076$ (down triangles).

the channel), but the mobility of the shortest chain dropped by 11% compared to the longest at d_{max} . They related the mobility difference at d_{max} to an N -dependent DNA density distribution stemming from contour-length dependent Taylor dispersion only seen in wide channels corresponding to a degree of confinement $C = R_g/d \lesssim 1.5$ [128]. In the present work, we observe a similar difference in the mobility for a smaller ratio between contour lengths and the same regime of confinement in the slit: $\mu(N = 64)/\mu(N = 24) \approx 1.14$ at $\Delta\rho/\langle\rho\rangle = 0.0015$ and $R_g(N = 24)/L_y \approx 0.62, \dots, R_g(N = 64)/L_y \approx 1.1$. Moreover, by reducing the bias to $\Delta\rho/\langle\rho\rangle = 0.00076$, the aforementioned mobility ratio stays approximately the same, but the monotonic increase in mobility extends from $N = 16$ to $N = 80$.

We have been careful not to use our simulation methodology outside of its regime of validity, which we have determined to extend at least to a level of confinement $C \approx 3$ within the de Gennes regime ($L_y/l_p \gg C > 1$, where l_p is the persistence length of the chain) [Publication V]. Our simulations indicate that an array of nanopits (height contrast $L_{z,\text{pit}}/h \approx 5.2$) with sidewalls leads at least to the same level of mobility differentiation within the de Gennes regime as in a slit. However, experiments by Mikkelsen *et al.* [24] exhibit mobility ratios up to 100 between linear DNA chains of lengths 165.6 kbp and 48.5 kbp for a height contrast of $L_{z,\text{pit}}/L_{z,\text{slit}} = 3$ in an array of troughs. Their work was distinctly different from ours in two ways. First, their slit region had a height comparable to the chain's persistence length, which corresponds to Odijk's regime of confinement [124]. Second, their pits were long troughs, which imposed no confinement on the chain in the y direction of Fig. 5.7.

We discuss the second distinction first. Mikkelsen and coworkers ob-

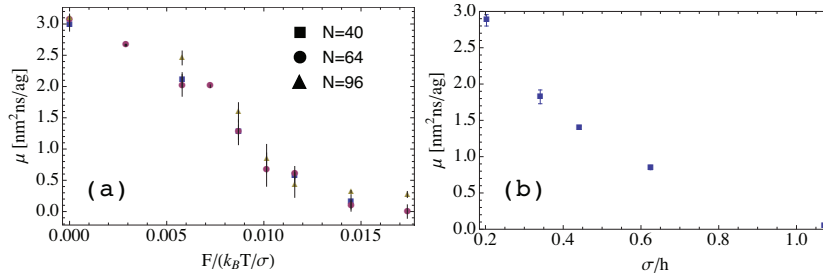


Figure 5.10. (a) Polymer mobility μ in the x direction as a function of the normalized magnitude of the downward force per monomer in the pit region $x \in [48, 95]$ nm. The pressure difference corresponds to $\Delta\rho/\langle\rho\rangle = 0.0015$ here. (b) The mobility μ versus the inverse of the slit height h/σ for $\Delta\rho/\langle\rho\rangle = 0.00076$ and $N = 48$.

served both linear and circular chains to escape from the pit either by its end (circular chain rolls out at both ends) threading the pit-to-slit interface first (“sidewinder” mode) or by the middle section of the chain forming a hairpin and thus initiating the propagation (“tumbleweed” mode) [24]. We have observed both of these propagation modes in simulations without sidewalls at a pressure differential of $\Delta\rho/\langle\rho\rangle = 0.0015$. Therefore, the propagation modes are dominated by the degree of confinement in the y direction. However, the degree of mobility differentiation appears to be dominated by the height of the slit region, which we discuss next.

The fact that the mobility for $N = 48$ through $N = 96$ in our simulations is roughly constant suggests that even $\bar{j}(0.0011) > j_c$ in the system. This observation is based on the assumption that j_c is independent of N . However, the ratio of the narrow’s linear size to the chain’s mean diameter $L_z/(2R_g)$ varies from 0.9 ($N = 16$) to 0.3 ($N = 96$), which makes it debatable whether the narrow in our system is small enough for Eq. (5.10) to hold altogether.

In spite of the numerical prefactor in the criterion of Eq. (5.10) being unknown [132, 133], it is interesting to compare the theoretical value of Eq. (5.10) for the threshold momentum density to the averages at different pressures in our simulations. We have $\bar{j}(\Delta\rho/\langle\rho\rangle = 0.00076)/j_c = 0.5$, $\bar{j}(0.0011)/j_c = 0.8$ and $\bar{j}(0.0015)/j_c = 1.1$. These numbers and the constant value of $\mu(N = 48, \dots, 96)$ for $\Delta\rho/\langle\rho\rangle = 0.0011$ suggest the numerical prefactor in Eq. (5.10) to be smaller than 0.5 for our system. The weakest feasible pressure difference (down triangles in Fig. 5.8) may be close to a threshold for our system as the dependence of μ on N strengthens as compared to stronger driving.

Based on the data provided by Mikkelsen *et al.*, we have determined

their smallest buffer velocity in the slit to exceed that in the threshold of Eq. (5.10) by a factor of 10. This is to say that Eq. (5.10) is largely irrelevant as far as applications are concerned since, in practice, devices need to be driven more strongly as exemplified by Ref. [24].

The mobility at $\Delta\rho/\langle\rho\rangle = 0.0015$ is roughly constant for $N \geq 80$ independent of the structure (number of branches). For smaller N , Fig. 5.8(a) tells that star polymers $(f, N_f) = (3, 16)$ and $(4, 12)$ move at very different velocities. However, as the mobility is plotted as a function of the relative size of the chain in Fig. 5.8(b), most star polymers with $N < 64$ or $R_g/L_y \lesssim 1.0$ have mobilities very close to those of linear chains of the same size. Albeit a weaker contrast than in Ref. [24], this observation supports the argument that artificial nanotopographies can lead to technologically significant mobility differentiation devices based on internal chain structure.

Another adjustable feature in the design of the sorting channel is the depth of the pit. In this work, we use a depth that we optimized to provide a maximal downward solvent flux in the upstream half of the pit. The guiding principle was to have as significant a downward push as possible in order to prolong the trapping time of the polymer. Deeper pits do not result in additional downward flux, but they do provide more space for the polymer to take up. Thus, increasing the pit depth could translate to larger mobility differences as a function of the degree of polymerization or possibilities for intermittent chain extraction from the system, and should be investigated in future work.

The pit region is suitable for imposing a vertical (electric) field on the polymer in order to enhance mobility differentiation. In Fig. 5.10(a), we plot the mobility for $N = 40, 64$ and 96 as a function of the downward force F per monomer in the pit region at $\Delta\rho/\langle\rho\rangle = 0.0015$, which results in no clear differentiation in Fig. 5.8. For the range of N considered and the pressure we use, values of $F/(k_B T/\sigma) = 0.016\text{--}0.032$ differentiate mobilities between the different chain lengths. This effect should be emphasized by reducing the driving even further, but it is not feasible computationally. Also, it is interesting that the mobilities do not remain ordered by N as F is increased. The total force on a chain is equal to NF , which for large enough F should lead to more prominent slowing down of long chains ($\mu(N = 96) < \mu(N = 40)$ at $F/(k_B T/\sigma) = 0.032$) and the flipping in the order appears to take place at $F/(k_B T/\sigma) = 0.03$. Even though the differences in μ seem small in Fig. 5.10(a), they are much larger than be-

tween the corresponding data points in Fig. 5.8 (circles). Thus, having a vertical field acting on the polymers at strong driving can facilitate separation as a function of polymer length.

The free energy difference between the slit and the pit regions can be increased by making the slit shallower. The effect of h on μ is shown in Fig. 5.10 for $N = 48$. We see that μ can be decreased roughly by an order of magnitude. In this case, the slit height decreases close to that in studies of polymer translocation [135, 136].

6. Summary

We have developed a hybrid simulation method that combines a compressible lattice-Boltzmann solvent and a particle phase described by molecular dynamics. The coupling between the two is implemented using a phenomenological velocity-based coupling. In contrast to all previous work, we have calibrated the coupling by requiring the simultaneous reproduction of several established fluid mechanical steady-state solutions. The calibration procedure fixes the only adjustable algorithmic parameter γ in the DBB equation.

Once γ is fixed, we find that the macroscopically observed fluctuation-dissipation theorem of Eq. (3.47) is obeyed quantitatively and the associated numerical contribution to the hydrodynamic radius due to the stencils is well understood. Moreover, the velocity autocorrelation function indicates that the mass of the particle is augmented by an added mass contribution in agreement with Eq. (2.22).

Our stochastic model is based on the theoretical Markovian framework for the coupled system presented in Section 2.3. In this thesis, we have demonstrated conclusively that no additional, external Langevin noise needs to be added to the equations of motion of either the solvent or the solute due to the solvent-solute coupling. By linking hydrodynamically calibrated particles with a FENE potential, we find the macroscopic fluctuation-dissipation theorem of Eq. (5.5) to be quantitatively obeyed and the chain's hydrodynamic radius to be in agreement with the theoretical prediction. All numerical multiscale models contain approximations. The ones we have made do not appear to come at the cost of the essential physics. However, there are systems to which our model is not directly applicable. For instance, placing a rigid DBB sphere at a gas-liquid interface [134] might require a varying γ in the two phases and at the interface, but it is a fascinating topic due to the recent availability of cou-

pling through conservative forces [113] and a fluctuating LB model with non-ideal equations of state [137].

We have derived closed-form expressions for the hydrodynamic force exerted on DBB particles. Our derivation generalizes earlier work based on homogenization theory and the results can easily be extended to incorporate separate coupling coefficients for normal and tangential slip by having different coupling coefficients γ_{\perp} and γ_{\parallel} in Eqs. (4.5) and (4.7).

DBB colloids reveal that they can be sorted in a T-shaped bifurcation by focusing them on a streamline that splits the particle beam into the outlets based on porosity. The particles should be placed sparsely enough in the beam in order to eliminate correlations between them. On the other hand, the two-particle correlations suggest the exotic possibility of encoding binary information to pairs of particles.

An investigation of polymer dynamics in a thin film has revealed the necessity of hydrodynamic interactions in confinement as Langevin dynamics given qualitatively incorrect results for the CM diffusion coefficient of the polymer. Our measurements suggest that the dynamic scaling changes continuously from that in two to that in three dimensions. The investigation could be extended to large polymer concentration to explore the limits of the methodology and the Zimm-to-Rouse dynamics transition.

Computational studies of mobility differentiation based on chain length and topology are challenging questions as entropic trapping requires large enough a difference in the chain free energy in different parts of the system and the small bias makes the simulations time consuming. Our early results show that mobility differentiation in simulations is observable and it can be enhanced both by external fields and by narrowing the slit region of the channel.

There are two general directions of research we would like to pursue in the future. The first are the topics of heat conduction in nanofluids and thermophoresis, which require an energy-conserving formulation of our fluctuating LBM following, *e.g.*, Ref. [138]. The second is the introduction of effective internal degrees of freedom to the LB fluid such that hydrophobicity/hydrophilicity could be accounted for in future studies of nanofluidics.

Bibliography

- [1] John D. Anderson, Jr., *Fundamentals of Aerodynamics* (McGraw Hill, 2010).
- [2] J. Seddon, *Basic Helicopter Aerodynamics* (BSP Professional Books, 1990).
- [3] Odd M. Faltinsen, *Hydrodynamics of High-Speed Marine Vehicles* (Cambridge University Press, 2005).
- [4] P. Moron, R. Powell, D. Freed, F. Perot *et al.*, *SAE Technical Paper* 2009-01-2203 (2009).

B. Crouse, D. Freed, S. Senthoooran, F. Ullrich *et al.*, *SAE Technical Paper* 2007-01-2400 (2007).
- [5] B. Duncan, S. Senthoooran, D. Hendriana, P. Sivakumar *et al.*, *SAE Technical Paper* 2007-01-0100 (2007).
- [6] S. P. Sutera and R. Skalak, *Annu. Rev. Fluid Mech.* **25** pp. 1-19 (1993).
- [7] Epson's Micro Piezo Technology, http://global.epson.com/innovation/printing_technology/micro_piezo_technology/characteristics/, <http://www.epson.com/cgi-bin/Store/Landing/InkTechPrinter.jsp>, accessed 5.3.2013.
- [8] G. M. Whitesides, *Nature* **442** pp. 368-373 (2006).
- [9] T. Thorsten, S. J. Maerkl, and S. R. Quake, *Science* **298** pp. 580-584 (2002).
- [10] T. Kalisky and S. R. Quake, *Nature Methods* **8** pp. 311-314 (2011).
- [11] D. Pushkarev, N. F. Neff, and S. R. Quake, *Nature Biotechnology* **27** pp. 847-850 (2009).

- [12] J. P. Glotzbach *et al.*, *PLoS ONE* **6** (6) e21211 (2011).
- [13] A. R. Wu *et al.*, *Lab Chip* **12** pp. 2190-2198 (2012).
- [14] G. Segré and A. Silberberg, *Nature* **189** pp. 209-210 (1961).
- [15] G. Segré and A. Silberberg, *J. Fluid. Mech.* **14** pp. 114-135 (1962).
- [16] G. Segré and A. Silberberg, *J. Fluid. Mech.* **14** pp. 136-157 (1962).
- [17] B. P. Ho and L. G. Leal, *J. Fluid Mech.* **65** pp. 365-400 (1974).
- [18] M. Masaeli *et al.*, *Phys. Rev. X* **2** 031017 (2012).
- [19] A. J. Mach *et al.*, *Lab Chip* **11** 2827 (2011).
- [20] E. M. Purcell, *Am. J. Phys.* **45** 3 (1977).
- [21] E. Lauga and T. R. Powers, *Rep. Prog. Phys.* **72** 096601 (2009).
- [22] H. Peng and X. S. Ling, *Nanotechnology* **20** 185101 (2009).
- [23] J. T. Del Bonis-O'Donnell, W. Reisner, and D. Stein, *New Journal of Physics* **11** 075032 (2009).
- [24] M. B. Mikkelsen, W. Reisner, H. Flyvbjerg, and A. Kristensen, *Nano Lett.* **11** pp. 1598-1602 (2011).
- [25] J. P. Boon and S. Yip, *Molecular Hydrodynamics* (Dover, New York, 1991).
- [26] R. Huang *et al.*, *Nature Physics* **7** pp. 576-580 (2011).
- [27] H. J. C. Berendsen, *Simulating the Physical World* (Cambridge University Press, 2007).
- [28] J. L. F. Abascal and C. Vega, *J. Chem. Phys.* **123** 234505 (2005); G. S. Fanourgakis, J. S. Medina, and R. Prosmiti, *J. Phys. Chem. A* **116** pp. 2564-2570 (2012).
- [29] Felix Franks, *Water: a matrix of life* 2nd Ed. (The Royal Society of Chemistry, 2000).
- [30] L. E. Reichl, *A Modern Course in Statistical Physics 2nd ed.* (John Wiley, 1998).
- [31] L. D. Landau and E. M. Lifschitz, *Fluid Mechanics* 2nd Ed. (Pergamon, 1987).

- [32] T. M. Squires and S. R. Quake, *Rev. Mod. Phys.* **77** pp. 977-1026 (2005).
- [33] G. G. Stokes, *Mathematical and Physical Papers by*, Vol. 3 pp. 55-59 (Cambridge University Press, 1901). Available online at <http://archive.org/details/cu31924004181339>.
- [34] H. Lamb, *Hydrodynamics* 6th Ed., (MacMillan, New York, 1932).
- [35] J. Rotne and S. Prager, *J. Chem. Phys.* **50** pp. 4831-4837 (1969).
- [36] J. Happel and H. Brenner, *Low Reynolds Number Hydrodynamics*, (Kluwer, Boston, 1983).
- [37] J. F. Brady and G. Bossis, *Ann. Rev. Fluid Mech.* **20** pp. 111-157 (1988).
- [38] C. W. Oseen, *Hydrodynamik*, (Akademische Verlag, Leipzig, 1927).
- [39] E. Wajnryb, P. Szymczak, B. Cichocki, *Physica A* **335** 339 (2004).
- [40] R. M. Jendrejack, M. D. Graham, J. J. dePablo, *J. Chem. Phys.* **119** 1165 (2003).
- [41] R. Brown, *The miscellaneous botanical works of Robert Brown*, Volume 1, Ed. John J. Bennett, R. Hardwicke (London, 1866).
- [42] E. Frey and K. Kroy, *Ann. Phys. (Leipzig)* **14** No. 1 - 3, 20- 50 (2005).
- [43] E. L. Cussler, *Diffusion, Mass Transfer in Fluid Systems*, 3rd Ed. (Cambridge University Press, 2007).
- [44] A. Einstein, *Ann. d. Phys.*, **17** pp. 549-560 (Leipzig, 1905).
- [45] M. Smoluchowski, *Ann. D. Phys.* **21** 756 (1906); M. Smoluchowski, *Bull. Internat. Acad. Krakovie* 202 (1906); R. M. Mazo, *Brownian Motion: Fluctuations, Dynamics and Applications* (Oxford University Press, New York, 2002).
- [46] R. Kubo, *J. Phys. Soc. Japan* **12** 570 (1957).
- [47] R. Kubo, *Science* **233** 330 (1986).
- [48] P. Langevin, *C. R. Acad. Sci. (Paris)* **146** pp. 530-533 (1908).
- [49] E. H. Hauge and A. Martin-Löf, *J. Stat. Phys.* **7** pp. 259-281 (1973).

- [50] J. Boussinesq, *C. R. Acad. Sci. Paris* **100** pp. 935-937 (1885).
<http://gallica.bnf.fr/ark:/12148/bpt6k3056t/f935.image.r=boussinesq>.
- [51] W. P. Graebel, *Advanced Fluid Mechanics* p. 213 (Academic Press, 2007).
- [52] V. Vladimirovsky and Y. A. Terletsky, *Hydrodynamical theory of translational Brownian motion.*, *Zh. Eksp. Teor. Fiz.* **15** pp. 258-263 (1945).
- [53] B. J. Alder and T. E. Wainwright, *Phys. Rev. Lett.*, **18** pp. 988-990 (1967).
- [54] B. J. Alder and T. E. Wainwright, *Phys. Rev. A*, **1** pp. 18-21 (1967).
- [55] A. Rahman, *Phys. Rev.*, **136** pp. A405-A411 (1964).
- [56] R. Zwanzig and M. Bixon, *Phys. Rev. A*, **2** pp. 2005-2012 (1970).
- [57] A. Widom, *Phys. Rev. A*, **3** pp. 1394-1396 (1971).
- [58] G. L. Paul and P. N. Pusey, *J. Phys. A: Math. Gen.* **14** pp. 3301-3327 (1981).
- [59] R. Kubo, *Rept. Progr. Phys.* **29** 235 (1966).
- [60] R. Zwanzig and M. Bixon, *J. Fluid Mech.* **69** pp. 21-25 (1975).
- [61] M. Lax, *Rev. Mod. Phys.* **32** pp. 25-64 (1960); M. Lax, *Rev. Mod. Phys.* **38** pp. 359-379 (1966); M. Lax, *Rev. Mod. Phys.* **38** pp. 541-566 (1966).
- [62] M. G. Velarde and E. H. Hauge, *J. Stat. Phys.* **10** pp. 103-105 (1974).
- [63] C. Denniston and M. O. Robbins, *J. Chem. Phys.* **125** 214102 (2006).
- [64] E. Lauga, M. P. Brenner, and H. A. Stone, *Handbook of Experimental Fluid Dynamics* Ch. 15 (Springer, New York, 2005).
- [65] P. Debye and A. M. Bueche, *J. Chem. Phys.* **16** 573 (1948).
- [66] H. C. Brinkman, *Appl. Sci. Res.* **A1** pp. 27-34 (1947).
- [67] H. C. Brinkman, *Appl. Sci. Res.* **A1** pp. 81-86 (1947).
- [68] J. M. Deutch and B. U. Felderhof, *J. Chem. Phys.* **62**, 2398 (1975).
- [69] B. U. Felderhof, *Physica A* **80**, pp. 63-75 (1975).

- [70] N. Liron N and S. Mochon, *J. Eng. Math.* **10** 287 (1976).
- [71] P. E. Rouse, *J. Chem. Phys.* **21** 1272 (1953).
- [72] B. H. Zimm, *J. Chem. Phys.* **24** 269 (1956).
- [73] M. Doi and S. F. Edwards, *The Theory of Polymer Dynamics*, (Oxford University Press, London, 1986).
- [74] P.-G. de Gennes *Scaling Concepts in Polymer Physics*, (Cornell University Press, London, 1979).
- [75] O. Punkkinen, E. Falck, I. Vattulainen, and T. Ala-Nissila, *J. Chem. Phys.* **122** 094904 (2005).
- [76] E. Falck, O. Punkkinen, I. Vattulainen, and T. Ala-Nissila, *Phys. Rev. E* **68** 050102R (2003).
- [77] A. Kopf, B. Dünweg, and W. Paul, *J. Chem. Phys.* **107** 6945 (1997).
- [78] P. J. Flory, *Statistical Mechanics of Chain Molecules*, John Wiley and Sons, New York, 1969.
- [79] F. Muller *et al.*, *Biomacromolecules* **12** pp. 3330-3336 (2011).
- [80] B. Li, N. Madras, and A. D. Sokal, *J. Stat. Phys.* **80** 661 (1995).
- [81] B. Dünweg, D. Reith, M. Steinhauser, and K. Kremer, *J. Chem. Phys.* **117** 914 (2002).
- [82] R. G. Winkler, L. Harnau, and P. Reineker, *Macromol. Theory Simul.* **6** pp. 1007-1035 (1997).
- [83] K. Mussawisade, M. Ripoll, R. G. Winkler, and G. Gompper, *J. Chem. Phys.* **123** 144905 (2005).
- [84] C. L. Dias, T. Ala-Nissila, M. Grant, and M. Karttunen, *J. Chem. Phys.* **131** 054505 (2009).
- [85] T. Hynninen, V. Heinonen, C. L. Dias, M. Karttunen, A. S. Foster, T. Ala-Nissila, *Phys. Rev. Lett.* **105** 086102 (2010).
- [86] A. P. Markesteijn, R. Hartkamp, S. Luding, and J. Westerweel, *J. Chem. Phys.* **136** 134104 (2012).
- [87] I. Pagonabarraga, M. J. H. Hagen, D. Frenkel, *Europhys. Lett.* **42** 377 (1998).

- [88] J. Smiatek, M. P. Allen, and F. Schmid, *European Phys. J. E* **26** 115 (2008).
- [89] G. Gompper, T. Ihle, K. Kroll, and R. G. Winkler, *Advances in Polymer Science* **221** 1 (2009).
- [90] A. Donev, B. J. Alder, and A. L. Garcia, *Phys. Rev. Lett.* **101** 075902 (2008); A. Donev, B. J. Alder, and A. L. Garcia, *J. Stat. Mech.* P11008 (2009).
- [91] F. Balboa Usabiaga, I. Pagonabarraga, and R. Delgado-Buscalioni
- [92] A. Donev and J. B. Bell and A. L. Garcia and B. J. Alder, *Multiscale Model. Simul.*, **8** pp. 871-911 (2010).
- [93] A. J. Chung, D. R. Gossett, and D. Di Carlo, *Small* doi: 10.1002/sml.201202413 (2012).
- [94] D. R. Gossett *et al.*, *Small* **8** No. 17 pp. 2757-2764 (2012).
- [95] S. Chen and G. D. Doolen, *Annu. Rev. Fluid Mech.* **30** pp. 329-364 (1998).
- [96] S. Succi, *The Lattice Boltzmann Equation for Fluid Dynamics and Beyond*, (Oxford University Press, USA, 2001).
- [97] S. Succi, A. A. Mohammad, and J. Horbach, *International Journal of Modern Physics C* **18** pp. 667-675 (2007).
- [98] H. K. Shin, C. Kim, P. Talkner, and E. K. Lee, *Chemical Physics* **375** pp. 316-326 (2010).
- [99] K. P. Travis, B. D. Todd, and D. J. Evans, *Phys. Rev. E* **55** pp. 4288-4295 (1997).
- [100] R. Balescu, *Statistical Dynamics: Matter out of Equilibrium* (Imperial College Press, London, 1997).
- [101] J.-P. Hansen and I. R. McDonald, *Theory of simple liquids* 3rd Ed. (Academic Press, 2005).
- [102] K. Huang, *Statistical Mechanics* 2nd Ed. (John Wiley & Sons, New York, 1987).
- [103] M. Bixon and R. Zwanzig, *Phys. Rev.* **187** pp. 267-272 (1969).

- [104] J. Hardy, O. Pazzis, and Y. Pomeau, *Phys. Rev. A* **13** pp. 1949-1961 (1973).
- [105] U. Frisch, B. Hasslacher, and Y. Pomeau, *Phys. Rev. Lett.* **56** pp. 1505-1508 (1986).
- [106] U. Frisch *et al.*, *Complex Systems* **1** pp. 649-707 (1987).
- [107] D. J. Holdych, D. Rovas, J. G. Georrgiadis, and R. O. Buckius, *Int. J. of Mod. Phys. C* **9** 1393 (1998).
- [108] P. J. Dellar, *Phys. Rev. E* **65** 036309 (2002).
- [109] P. J. Dellar, *J. Comput. Phys.* **190** pp.351-370 (2003).
- [110] C. S. Peskin, *Acta Numer.* **11** p. 479 (2002).
- [111] R. Adhikari, K. Stratford, M. E. Cates, and A. J. Wagner, *Europhys. Lett.* **71** pp. 473-479 (2005).
- [112] H. Hasimoto, *J. Fluid Mech.* **5** pp. 317-328 (1959).
- [113] F. E. Mackay and C. Denniston, *Journal of Computational Physics* **237** 289 (2013).
- [114] F. E. Mackay, S. T. T. Ollila and C. Denniston, to appear (2013).
- [115] J. R. Looker, J. R. and S. L. Carnie, *Phys. Fluids* **16** pp. 62-72 (2004).
- [116] K. Svanes and B. W. Zweifach, *Microvasc. Res.* **1** pp. 210-220 (1968).
- [117] Y. C. Fung, *Microvasc. Res.* **5** pp. 34-48 (1973).
- [118] V. Doyeux, T. Podgorski, S. Peponas, M. Ismail, and G. Couplier *J. Fluid Mech.* **674** pp. 359-388 (2011).
- [119] G. S. Grest and K. Kremer, *Phys. Rev. A* **33** 3628 (1986).
- [120] B. Liu and B. Dünweg, *J. Chem. Phys.* **118** 8061 (2003).
- [121] C. Micheletti and E. Orlandini, *Macromolecules* **45** pp. 2113-2121 (2012).
- [122] W. Reisner, J. N. Pedersen, and R. H. Austin, *Rep. Prog. Phys.* **75** 106601 (2012).
- [123] Y. Wang, D. R. Tree and K. D. Dorfman, *Macromolecules*, **44**, 6594-6604 (2011).

- [124] T. Odijk, *Macromolecules*, **16** 1340 (1983).
- [125] E. A. Strychalski, S. L. Levy, and H. G. Craighead, *Macromolecules*, **41**, pp. 7716-7721 (2008).
- [126] J. Tang, S. L. Levy, D. W. Trahan, J. J. Jones, H. G. Craighead, and P. S. Doyle, *Macromolecules*, **43**, pp. 7368-7377 (2010).
- [127] W. Humphrey, A. Dalke and K. Schulten, *J. Molec. Graphics* **14** 1 pp. 33-38 (1996).
- [128] D. Stein, F. H. J. van der Heyden, W. J. A. Koopmans, and C. Dekker, *P Natl Acad Sci USA* **103** pp. 15853-15858 (2006).
- [129] J. Han, S. W. Turner, and H. G. Craighead, *Phys. Rev. Lett.* **83** pp. 1688-1691 (1999).
- [130] J. Han and H. G. Craighead, *Science* **288** pp. 1026-1029 (2000).
- [131] J. Han and H. G. Craighead, *Anal. Chem.* **74** pp. 394-401 (2002).
- [132] T. Sakaue, E. Raphael, P.-G. de Gennes, and F. Brochard-Wyart *Europhys. Lett.*, **72**, pp. 83-88 (2005).
- [133] A. P. Markesteijn, O. Berk Usta, Issam Ali, Anna C. Balazs, and J. M. Yeomans, *Soft Matter* **5** pp. 4341-4584 (2009).
- [134] J. W. J. de Folter, V. W. A. de Villeneuve, D. G. A. L. Aarts, and H. N. W. Lekkerkerker, *New J. Phys.* **12** 023013 (2010).
- [135] M. Miholovic, N. Hagerty, and D. Stein, *Phys. Rev. Lett.* **110** 028102 (2013).
- [136] C. Dekker, *Nature Nanotechnology* **2** pp. 209-215 (2007).
- [137] M. Gross, R. Adhikari, M. E. Cates, and F. Varnik, *Phys. Rev. E* **82** 056714 (2010).
- [138] N. I. Prasianakis and I. V. Karlin, *Phys. Rev. E* **76** 016702 (2007).



ISBN 978-952-60-5198-7
ISBN 978-952-60-5199-4 (pdf)
ISSN-L 1799-4934
ISSN 1799-4934
ISSN 1799-4942 (pdf)

Aalto University
Aalto School of Science
Department of Applied Physics
www.aalto.fi

**BUSINESS +
ECONOMY**

**ART +
DESIGN +
ARCHITECTURE**

**SCIENCE +
TECHNOLOGY**

CROSSOVER

**DOCTORAL
DISSERTATIONS**